ELECTROSTATIC (LANGMUIR) PROBE MEASUREMENTS IN RF DRIVEN He, N_2, BCl_3, AND BCl_3/N_2 PLASMAS

BY

Bogdan Amaru Pathak
(cc)(i)($) 2008

Submitted to the graduate degree program in Electrical Engineering
and the Graduate Faculty of the University of Kansas
in partial fulfillment of the requirements for the degree of
Master of Science in Electrical Engineering.

____
Dr. Karen J. Nordheden,
Co–chairperson

____
Dr. Rongqing Hui,
Co–chairperson

____
Dr. Christopher Allen

____
Dr. Glenn Prescott

Date Defended: _________________________

The Thesis Committee for Bogdan Amaru Pathak certifies
that this is the approved version of the following thesis:

ELECTROSTATIC (LANGMUIR) PROBE MEASUREMENTS IN
RF DRIVEN He, N_2, BCl_3, AND BCl_3/N_2 PLASMAS

Committee:

____
Dr. Karen J. Nordheden
Co–chairperson

____
Dr. Rongqing Hui
Co–chairperson

____
Dr. Christopher Allen

____
Dr. Glenn Prescott

Date Approved: ________________________

Dedication and Acknowledgements

I would like first like to thank everyone who stuck it out with me these many years—ordinary people would have quit long ago.

To my family who encouraged, cajoled, threatened, supported, and on more than one occasion helped me keep things in perspective. Thank you.

To my colleagues, mentors, and committee members for (often against your better judgment) letting me take the path less traveled and get sidetracked without allowing me to lose focus. You helped me learn more than those letters after my name will ever be able to convey. I am particularly indebted to you, Dr. N and John.

To all the previous researchers in plasma physics, electrical engineering, and any of the other scientific fields—well known or anonymous—you are all giants in your own right. From Dr. Irving Langmuir to all the graduate students whose work I have read, thank you for letting me stand on your shoulders and put one more block into the forever changing wall of scientific understanding. It is a rare thrill, even if that block is tiny.

To my friends who made these years worthwhile not only educationally and scientifically but by helping me grow on a personal level. Keep up the good work wherever you end up. You can and do change people for the better. Especially you, Brianne.

To Max (my cat): There's nothing quite like a good lap warmer to help you type. I'm sorry about the new kittens…this does mean you get better food, though.

To everyone I've met along the way who expanded my horizons, whether it was in Kansas, Poland, Michigan, New Mexico, India, or on the dance floor.

Thank You ♦ Dzękuje ♦ Merci ♦ धन्यवाद ♦ Gracias

Abstract

A Langmuir (electrostatic) probe was designed and constructed to measure the average electron energy ($<\varepsilon>$), electron temperature (kT_e) and electron density (N_e) in He, N_2, BCl_3, and BCl_3/N_2 capacitively coupled plasmas (CCPs). Helium, N_2, and BCl_3 plasmas were used to calibrate and validate the new probe system; BCl_3/N_2 plasmas were investigated.

Previously described small increases in N_e when N_2 is added to BCl_3 plasmas cannot fully explain the substantial increase in gallium arsenide (GaAs, 13.3× @ 60% N_2) and copper (Cu, 7.5× @ 30% N_2) etch rate. Though it was hypothesized that $<\varepsilon>$ increased with N_2 addition leading to increased etch rates, probe measurements show that $<\varepsilon>$ decreases when N_2 is added to BCl_3 plasmas (4.52 eV @ 0% N_2, 3.69 eV @ 60% N_2, 4.14 eV @ 30% N_2). Increases in negative ion densities were observed with N_2 addition (15.6× @ 60% N_2, 10.3× @ 30% N_2, maximum: 20.8× @ 40% N_2) that correlate with both GaAs and Cu etch rates. These findings are consistent with two reaction pathways. The most likely pathway suggests N_2 metastables create Cl neutrals that ionize and become active etch species that etch the substrate or that recombine and dissociate into Cl^- ions.

Table of Contents

Dedication and Acknowledgements ii

Abstract iv

Table of Contents v

List of Symbols and Abbreviations...ix

List of Figures xi

List of Tables xiv

Chapter 1. Motivation 1

1.1. Background 1

1.2. Etching as a Function of both Plasma and Substrate.....................2

1.3. Plasma Chemistry—Reactive, Inert, and Inhibiting Species 5

Chapter 2. Literature Review and Basis...8

2.1. Indicators—Common Ground 8

2.2. Mixed Chemistry Plasmas 9

2.3. Diagnostic Methods 13

2.4. Langmuir Probes 15

Chapter 3. Review of Relevant Plasma Physics 17

3.1. Plasma Physics Review 17

Chapter 4. Langmuir (Electrostatic) Probe Description..........................22

4.1. Background 22

4.2. Preliminary Electrostatic Probe Theory 22

Ideal Langmuir Probe Behavior in a DC Plasma of a Single Species 24

4.3. Practical Considerations in an RF driven processing plasma 27
Time Varying, RF Plasma Source 28
Plasma-Probe Tip Interactions and Probe Tip Contamination 30

4.4. Interpreting the Probe Sweep 32
Finding V_p 34
Laframboise Correction 34
The Electron Energy Distribution Function (EEDF) 37
The Log-Slope method 39
The SmartProbe Method 41

4.5. The Effect of Negative Ions and (Charged) Metastables on the Second Derivative of the I-V Characteristic 43

Chapter 5. Experimental Setup & Protocol 46

5.1. PlasmaTherm 790 48

5.2. Langmuir Probe 51
Probe Tip 51
Compensation Electrode and Shield 54
Probe Body and Housing 54
Internal Probe Electronics 55
In Situ Monitoring via Oscilloscope 58

5.3. Data Acquisition System 58
Sourcemeter 59
Control Program and Hardware 60

5.4. Data Analysis 67

5.5. Experimental Protocol 69
Determination of plasma region of interest and correct probe height 69
Cleaning 72
Probe Sweep and Plasma Settling Timing Parameters 74

Chapter 6. Experimental Chemistries 75

6.1. Helium Calibration 75

6.2. Variation of kT_e and N_e, and the Evolution of the EEDF in He 75
Pressure Variation 75

Power Variation 83

6.3. N_2 Calibration 86

6.4. Variation and Relevance of kT_e and N_e, and the Evolution of the EEDF in N_2 88
Pressure Variation 88
Power Variation 93

6.5. BCl_3 Calibration & Investigation 96

6.6. Variation in N_e and kT_e, as well as Evolution of the EEDF in BCl_3 97
Pressure Variation 97
Power Variation 100
Power Variation 101

6.7. BCl_3/N_2 Composition Experiments 103

6.8. Effect of Composition on Negative Ion Density, the EEDF, kT_e, and N_e 103
EEDF and Second Derivative Structure—Evidence of Negative Ions 103
Aggregate Metrics—Equivalent kT_e and N_e 106
Aggregate Metrics—Equivalent kT_e and N_e 107

6.9. Comparing Negative Ion Density with Etch Rate in BCl_3/N_2 Plasmas 109

Chapter 7. Conclusions 113

References 116

Appendix A. Chamber Description 121

A.1. Reactive Ion Etching System 121

Appendix B. Sample MathCAD Worksheets 124

Appendix C. Langmuir Probe and Sweep Identification 150

C.1. Sweep Identification 150

C.2. Langmuir Probe Identification..154

List of Symbols and Abbreviations

Symbol or Abbreviation	Definition	Common Unit
kT_e	Electron Temperature (as Defined in a Maxwellian Distribution)	eV
kT_+	Positive Ion Temperature (as Defined in a Maxwellian Distribution)	eV
N_e	Electron Density	cm^{-3}
N_-	Negative Ion Density	cm^{-3}
N_+	Positive Ion Density	cm^{-3}
EDF	Energy Distribution Function	
EEDF	Electron Energy Distribution Function	
EVDF	Electron Velocity Distribution Function	
EEPF	Electron Energy Probability Function (N.B: Not an actual probability distribution, i.e., $\int_0^\infty \text{EEPF}\, dE \neq 1$)	
ε	Electron Energy	eV
$<\varepsilon>$	Mean Electron Energy	eV
DC	Direct Current	
CCP	Capacitively Coupled Plasma	
RIE	Reactive Ion Etching	
ICP	Inductively Coupled Plasma	
X*	Excited or Metastable Species of Atom, Ion, or Molecule X (e.g., N_2* would be an Excited or Metastable Nitrogen molecule.)	
OES	Optical Emission Spectroscopy	

QMS	Quadrupole Mass Spectrometry	
LIF	Laser Induced Fluorescence	
V_f	Floating Potential	V
V_p	Plasma Potential, Space Potential	V
V_b	Langmuir (Electrostatic) Probe Bias	V
I_e	Electron Current	μA
I_+	Positive Ion Current	μA
I_-	Negative Ion Current	μA
λ_D	Debye Length, Debye Wavelength, Debye Radius	m
q_e	Electronic Charge (Negative)	C
A_p, A_{probe}	Surface Area of the Langmuir (Electrostatic) Probe Tip	m^2
m_e	Mass of an Electron	kg
m_+	Mass of the Appropriate Positive Ion	kg
MFC	Mass Flow Controller	
ID	Inner Diameter	cm
OD	Outer Diameter	cm
RF	Radio Frequency	>1 MHz
SRF	Self Resonant Frequency	MHz
LOESS	Locally Weighted Scatterplot Smoothing [46-47]	

List of Figures

Figure 2.1: The etch rate of copper as a function of % BCl_3 in BCl_3/N_2 (○) and BCl_3/Ar (△), (50 mTorr, -300 V bias, 250°C) [3, 12]....................... 11

Figure 2.2: The etch rate of GaAs as a function of % BCl_3 in BCl_3/N_2 (●) and the DC Bias as a function % BCl_3 in BCl_3/N_2 (■) (15 mTorr, 50 W RF power) [4, 6]... 12

Figure 4.3: Ideal probe trace with V_f and V_p labeled................................. 26

Figure 4.4: Illustration of various levels of RF distortion of the electron current [19]. 29

Figure 4.5: Graphical example of Laframboise correction to V_p. 36

Figure 4.6: Schematic drawings of the positive ion current (i_+) and the second derivative of the electron, negative ion, and positive ion currents (i_e'', i_-'', i_+'') [16]. Dotted curve: ideal case; solid line: actual observation. 45

Figure 5.7: Schematic of experimental apparatus used in Langmuir probe studies. 47

Figure 5.8: Schematic of the PlasmaTherm 790 Series capacitively coupled plasma chamber used in Langmuir probe and etching experiments [6]. 49

Figure 5.9: Schematic describing the Langmuir probe positioning radially in the chamber. 50

Figure 5.10: Illustration/Schematic of typical Langmuir probe construction. Based on previous designs by Chen *et al.* and Hopkins *et al.* [15, 19, 34]... 52

Figure 5.11: Overview screenshot of data acquisition application. 61

Figure 5.12: Screenshot of the data file organization form in the data acquisition application.. 62

Figure 5.13: Screenshot of the probe cleaning form 63

Figure 5.14: Screenshot of the sweep control form. 66

Figure 5.15: Labeled photograph of a probe in situ demonstrating the visual guides used to determine accurate vertical positioning. 70

Figure 5.16: Photographs of a probe positioned to measure the presheath (Top, 100% N_2, 15 mTorr, 50 W) and the bottom of the bulk of the plasma (Bottom, He plasma, 50 mTorr, 100 W). 71

Figure 6.17: kT_e and N_e measurements 100% He, 175 W RF Power plasma with pressure ranging from 20 to 150 mTorr (Run 121). 77

Figure 6.18: Comparison of an EEDF of a 100% He, 40 mTorr, 175 W plasma with a Maxwellian and Druyvesteyn distribution of equal average electron energy. 78

Figure 6.19: Comparison of an EEDF of a 100% He, 125 mTorr, 175 W plasma with a Maxwellian and Druyvesteyn distribution of equal average electron energy, as well as a Druyvesteyn distribution with ¾ the average electron energy found from the observed EEDF. 79

Figure 6.20: Evolution of the EEDF in 175 W He calibration plasmas. 80

Figure 6.21: Comparison of kTe and Ne calculations based on Log-Slope, SmartProbe, and EEDF measurements in 175 W He calibration plasmas. 82

Figure 6.22: Comparison of the kT_e and N_e values obtained using various techniques in 125 mTorr He calibration plasmas. 84

Figure 6.23: Comparison of the equivalent kT_e and N_e values obtained using various techniques (including LaFramboise correction) in 50 W N_2 calibration plasmas. 89

Figure 6.24: Comparison of the EEDFs of 40-75 mTorr N_2 calibration plasmas. 90

Figure 6.25: Comparison of the EEDFs of 10-40 mTorr N_2 calibration plasmas. 91

Figure 6.26: Comparison of EEDFs for 25-300 W N_2 calibration plasmas. 94

Figure 6.27: Comparison of the equivalent kT_e and N_e values obtained using various techniques in 15 mTorr N_2 calibration plasmas. 95

Figure 6.28: Comparison of the equivalent kT_e and N_e values obtained using various ranges for the EEDF in 50 W BCl_3 calibration plasmas. 98

Figure 6.29: Comparison of EEDFs for 25-100 W BCl_3 calibration plasmas. 100

Figure 6.30: Comparison of the equivalent kT_e and N_e values obtained using various ranges for the EEDF in 15 mTorr BCl_3 plasmas. 102

Figure 6.31: Comparison of EDFs of mixtures of 40-100% BCl_3 (balance N_2) plasmas at 15 mTorr and 50 W. 105

Figure 6.32: Comparison of EDFs of mixtures of 0-40% BCl_3 (balance N_2) plasmas with the EDF of a 100% BCl_3 plasma at 15 mTorr and 50 W. 106

Figure 6.33: Comparison of the equivalent kT_e and N_e values in 15 mTorr, 50 W BCl_3/N_2 plasmas of varying compositions. 108

Figure 6.34: Comparison of normalized area under the negative ion region of the EEPF (or second derivative). 110

Figure A.35: Schematic of the PlasmaTherm 790 series capacitively coupled plasma chamber used in the Langmuir probe and etching experiments........... 123

Figure C.36: Folder tree showing the hierarchy of folder names exemplifying the folder naming conventions........... 151

Figure C.37: Several run files exemplifying the run naming conventions. 153

List of Tables

Table 5.1: Probe tip characteristics used for experimental chemistries presented. 53

Table 5.2: Inductor characteristics used in the passive RF filters. 57

"Every winner has scars."

—Herbert Casson

"Vincit qui patitur: he conquers, who endures."

—Percy Cerutty

Chapter 1. Motivation

1.1. Background

The current proliferation of integrated devices in electronics results directly from the invention of the transistor. The transistor alone, however, cannot be wholly credited with the increase in device density that Gordon Moore predicted in 1965 [1]. The increase in device density and miniaturization of integrated chip (IC) devices is a testament to the unique properties of plasma processing, and in particular, plasma etching to create anisotropic features.

Today, plasma technology is critical to many different parts of the integrated chip manufacturing process. Engineers in industry and research employ plasma processing both to accomplish the mundane (e.g., removal of excess photoresist) and to push the limits of research (e.g., creation of microscopic features in micro-electro-mechanical systems—MEMS).

Despite the overwhelming use of plasma etching in industry, research in plasma technology continues unabated for at least two reasons. First, silicon (Si), the most common substrate used in the microchip industry, is not suitable for all applications, particularly in electro-optics and more environmentally demanding situations because of its narrow bandgap,

and the resultant low resistance to external radiation. This makes controlling and characterizing the plasma etching process in III-V materials such as Gallium Arsenide (GaAs) and Gallium Nitride (GaN) as well as other unique substrates such as Silicon Carbide (SiC) and Zinc Oxide (ZnO) extremely appealing. Second, while plasmas are commonly used, the process of selecting the correct plasma parameters for a particular job remains highly experiential. There is a need, therefore, for a theoretical framework to explain why etch rates reach maxima and how etch rates vary with plasma parameters such as included power, pressure, and chemical composition. Because of the lack of a complete framework, a body of experimental evidence characterizing several often used plasmas is desirable and testable hypotheses based on this body allow research to take the next steps forward.

1.2. Etching as a Function of both Plasma and Substrate

Plasma etching involves interplay of both physical and chemical processes. While the results of an etch process are a function of the physical characteristics of the semiconductor being etched (crystal structure, orientation, bond energy, etc.) and the physical characteristics of the plasma in which it is etched (electron energy—kT_e, electron density—N_e, chemical composition, pressure, etc.), the chemical reactions of the active plasma species and the substrate must produce products that

are sufficiently volatile to evaporate and expose a new layer to be etched. These product volatilities are often used to predict whether an active etchant (such as F or Cl) will etch a given substrate (such as SiC or GaAs) and are valuable tools in selecting plasmas that will selectively etch through one layer of a substrate and not another. Still, understanding the plasma parameters allows one to predict (and then experimentally test) the ability of a certain plasma to effectively etch a particular substrate. Thus, an understanding of these characteristic quantities, as well as studies on multiple substrates is an important and worthy scientific and engineering endeavor.

As testing numerous materials and plasma parameters could result in years of study, this work is limited to evaluating the changes in the plasma characteristics but will include etch results from previous studies [2-6]. Further, this thesis will limit its discussion to those plasmas used for etching III-V or wide bandgap semiconductors. For our studies, the plasmas will be low density, Capacitively Coupled Plasma (CCP) discharges. They give rise to Reactive Ion Etching (RIE) where reactive ions are created by electron collisions and other mechanisms and are then accelerated across a strong electrostatic sheath into the target substrate.

While RIE plasma parameters are controlled externally by varying pressure, chemical composition, and electrode power (which induces a self bias on the powered electrode), the physical plasma parameters that are affected within the bulk plasma are electron and ion density as well as electron and ion energy (sometimes referred to as electron and ion temperature). As the electrons in plasmas are much more mobile than the ions because of their much lower mass, they are responsible for the majority of interactions (collisions, attachment, etc.) that result in dissociation and excitation reactions. Thus, by examining the electron temperature, electron density, and electrode DC bias one can attribute the effect that changes in external parameters have on etch rate to these more intrinsic plasma parameters.

More modern techniques such as Inductively Coupled Plasmas (ICPs) are now used rather than CCPs for some of the higher bond strength (wider bandgap) materials, since they allow independent control of ion production and ion impact energy. The same physical processes, however, occur in ICPs and CCPs to produce ions and we believe that our experimental results can be extrapolated to ICPs. Specifically, if we are able to show how the various external conditions affect trends in kT_e and N_e in CCP discharges, the effects should be extendable to ICP discharges with similar kT_e and N_e values or using similar etching chemistries.

1.3. Plasma Chemistry—Reactive, Inert, and Inhibiting Species

Previous work in the University of Kansas Plasma Research Laboratory (KU PRL or KU Plasma Research Lab) has focused on reactive ion etch rates in wide bandgap semiconductors such as GaAs, InGaAsP, SiC, and GaN [2, 4-6]. Reactive species such as chlorine are commonly used to etch gallium based substrates because chlorine reacts with the substrate resulting in gallium chloride ($GaCl_x$) which is volatile and quickly sublimates into the plasma atmosphere. In these situations, boron trichloride (BCl_3) is often used as the donor molecule. While inert species such as argon (Ar) or helium (He) do not react with the substrate and only etch by physically colliding with the substrate and knocking the substrate atoms out of their crystal matrix, both research and industry experience shows that a small percentage of an inert gas can stabilize the discharges. Finally, fluorine acts as an inhibiting species for gallium and aluminum based substrates because gallium fluoride (GaF_x) and aluminum fluoride (AlF_x) are not sufficiently volatile to sublimate and expose new layers of the substrate to the etching plasma making pure sulfur hexafluoride (SF_6) unsuitable for etching GaAs or GaN. Furthermore, when even a small amount of SF_6 is added to a BCl_3 plasma it can completely prevent the plasma from etching AlGaAs or AlAs. Because of this unique property, SF_6 is added to plasmas to halt the etching process at a buried AlAs or AlGaAs

layer. Counterintuitively, that same addition of SF_6 to BCl_3 drastically increases the etch rate in GaAs [5]. This initial inconsistency raises interesting questions and has inspired research into mixed gas plasmas at the KU PRL and elsewhere.

Investigation into mixed gas plasma chemistries has raised questions about the effect of adding what were initially considered either diluent or inhibitory gases (Ar, He, N_2, SF_6 etc.) to active etching gases. Since plasmas consisting of only diluent or inhibitory gases are not effective reactive ion etchants and can only etch through brute force sputtering if at all, intuition holds that adding them to an active gas should decrease the overall etch rate. Many investigators have found this not to be the case, and in fact the opposite is often true [2-5, 7, 8].

Individual KU PRL investigations [4, 5] revealed that BCl_3/N_2 and BCl_3/SF_6 plasmas etch GaAs and GaN faster than pure BCl_3 plasmas. Similarly, SF_6/He plasmas etch SiC faster than pure SF_6 plasmas. These discoveries prompted electron density measurements using microwave interferometry with the hope of explaining the increased etch rate. These inquiries had mixed results. Electron density in SF_6/He plasmas increased with increasing He and displayed a direct correlation with the increase in etch rate; electron density increased with increasing N_2 in BCl_3/N_2

plasmas but not sufficiently to fully explain the increase in etch rate, and electron density actually decreased with increasing SF_6 in BCl_3/SF_6 plasmas though the etch rate increased. This recent research into these critical plasma parameters suggests that quantifying just electron density while controlling for DC bias is not sufficient to predict etch rate.

Because it is clear that N_2 and He effect a palpable change in etch rates, electron density, and perhaps electron energy/temperature when added to BCl_3 and SF_6, this thesis will refer to BCl_3/SF_6, BCl_3/N_2, and SF_6/He as mixtures. This is in contrast to previous papers that sometimes refer to admixtures or diluted plasmas. The exception to this will be when the thesis discusses N_2, He, or Ar as inactive in their own right, rather than in combination with SF_6 or BCl_3.

Chapter 2. Literature Review and Basis

2.1. Indicators—Common Ground

When striking a plasma discharge, the most notable parameters are external or extrinsic—chemistry, incident RF power, chamber pressure, chamber geometry, etc. Thus, these, along with the target substrate, are naturally what most engineers use to describe a process plasma. However, when one varies chamber geometry, substrate, or the technology used to strike the plasma, things get muddled quickly. How can one compare CCP to ICP to other novel plasma generation techniques? The answer lies in intrinsic or internal parameters such as electron density, ion density, electron temperature, ion temperature, etc. While these parameters still depend on the external parameters used to create them, they also provide a window into suggesting common ground among similar, but not directly comparable, plasmas.

For all its quantitative precision, absolute etch rate is not necessarily a good indicator as it is highly dependent on the factors mentioned above and it is not an intrinsic plasma parameter. Relative etch rate, however, is a good starting point in this research. Let us be clear—a controllable, very selective etch rate that produces clean features is the ultimate goal. In the process of finding that target etch rate, however, we hope to learn

something important about how the more basic internal parameters influence etch rate. Our interest is further piqued by etch rate trends that are counterintuitive when only external parameters are considered. Specifically, why would diluting a known etchant with a noble (and theoretically inert) or other inert, non-etching gas result in an increase in etch rate?

2.2. Mixed Chemistry Plasmas

Mixed chemistry plasmas have long garnered interest because they can show enhanced etch rates, selectivity, and surface profiles over single constituent plasmas. The mundane nature of the first patent using a mixture of CF_4 and O_2 to etch silicon (filed in 1969), however, shows that the potential advantages of mixed chemistry plasmas are rarely seen in their first applications. Over the years, the idea of adding a second or third parent molecule to plasmas gained traction, and both plasma enhanced deposition and plasma etching benefited from this advance. For industry, this increased the complexity of plasma processes, and made the process parameters a way to compete with one another. For researchers, it opened new avenues to gain further understanding about plasma physics, chemistry, and its applications.

Because industrial process plasma parameters are almost always held as industrial trade secrets interested in etch and deposition rates as well as surface morphology, the literature contains few meaningful examples of plasma process recipes. Nonetheless, some chemistries (such as $SiCl_4 + H_2 + Ar$) are well explored and characterized both from an effect-based as well as a mechanistic standpoint. Mechanistically, these explorations document dissociation into active components through radical-molecule (e.g., $SiCl_4 + H_2$), ion-molecule (e.g., $SiCl_4 + Ar$), and electron-molecule interactions [9]. Unfortunately, most explorations are incomplete and indicate that the target effect (be it deposition or etching) scales non-linearly with concentrations and other parameters [2-6, 9-11]. This means that most explorations first characterize the mixture from the point of view of the target effect, and only later characterize its mechanism. Simply put, the technology of mixed chemistry plasma etching advances faster than 1) is reported in the literature and 2) the science that explains how or why it works.

In his thesis in 1993 and later as a paper in 1994, B. Howard described a chemistry (i.e., BCl_3/N_2) that etched copper faster as a mixture than a plasma of only its active parent ingredient, BCl_3 [3, 12]. The study described several "response models for copper etch rate behavior" and showed that the etch rate of copper peaked at 75% BCl_3/25% N_2 in a 50

mTorr, -300 V DC Bias, 250°C plasma (See Figure 2.1). The models correlated various external parameters such as temperature, pressure, and DC bias with copper etch rate. Ion density measurements were also taken, but the results did not fully explain the increase in etch rate with N_2 addition and so Howard did not attempt to posit a causative mechanism.

This study, as well as previous work by K. Nordheden [5, 10] inspired studies into BCl_3/N_2 discharges for etching III-V semiconductors at the KU PRL. J. Sia and K. Nordheden not only focused on etch rate

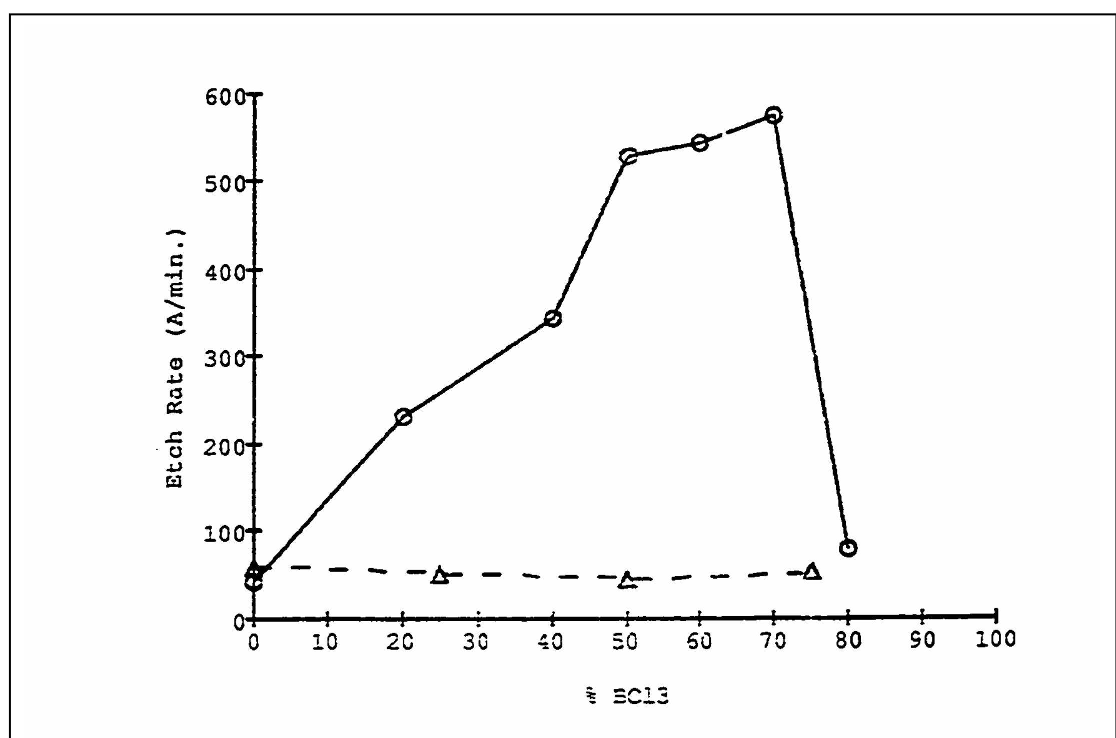

Figure 2.1: The etch rate of copper as a function of % BCl_3 in BCl_3/N_2 (○) and BCl_3/Ar (△), (50 mTorr, -300 V bias, 250°C) [3, 12].

comparisons, but attempted to explain the increase in etch rate using Cl concentrations and electron density increases. The etch rate findings mirrored those of Howard, though the maximum appeared at 40% N_2, and a sharper peak was noted. (See Figure 2.2.) The mechanistic findings were not as promising: though Cl concentrations and energy density were clearly contributory, these factors did not fully explain the increase in etch rate.

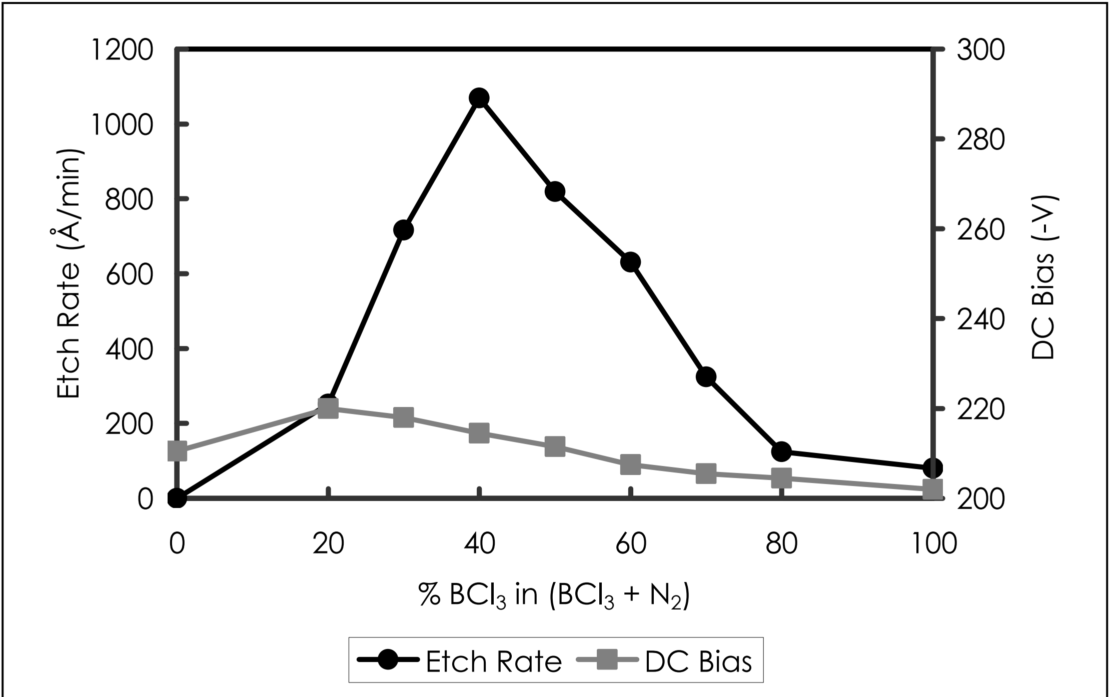

Figure 2.2: The etch rate of GaAs as a function of % BCl_3 in BCl_3/N_2 (●) and the DC Bias as a function % BCl_3 in BCl_3/N_2 (■) (15 mTorr, 50 W RF power) [4, 6].

2.3. Diagnostic Methods

Plasma diagnostics seek to measure plasma parameters or to obtain other information about the state of the plasma. The most common diagnostic methods are mass spectrometry, electrostatic probes, optical emission spectroscopy, and microwave phase measurements. Each has its advantages and disadvantages depending on the target parameter, and for this reason, different diagnostic methods are used in different situations. On one end of the diagnostic spectrum, mass spectrometry can identify the mass to charge ratio and relative number of molecules, ions, or other species present in the molecular spectrometer, but cannot guarantee that those are the actual species present in the plasma because of the recombination reactions that the species potentially undergo in transit to the detector. The upside of the *ex situ* nature of this method is that it does not perturb the plasma. On the opposite end of the spectrum, electrostatic (or Langmuir) probes do not directly shed any light on the chemical nature of plasmas but can find various relevant physical parameters (e.g., electron temperature and electron density) which are measured within the plasma itself. The downside to this *in situ*, intrusive technique is that it must perturb the plasma to measure the parameters, and therefore the plasma must be large enough to screen out the local perturbation so as not to affect the bulk of the plasma. [9]

Both J. Sia and R. Alapati employed almost the entire gamut of diagnostic techniques in various attempts to ferret out the parameters that were responsible for the increased etch rate in the mixtures of BCl_3/N_2 and SF_6/He, respectively [2, 4, 6]. These included microwave phase change measurements, optical emission spectroscopy (OES), and quadrupole mass spectrometry (QMS). These methods elucidated that increases in the DC bias and electron density (N_e) could completely explain the increases seen SF_6/He plasmas. However, the results could not fully explain the significant rise in etch rate in BCl_3/N_2 plasmas, either chemically, because of increased DC bias, or because of electron density increases. In her work [4, 6], Sia did see an increase in Cl species, but neither N_e nor DC bias could explain it, therefore she posited that either kT_e or energy transfer from N_2 metastables were the most likely mechanisms behind Cl species production. Electrostatic probes, therefore, became the next logical step to understanding these plasmas since they could measure additional information about electron energy distributions that microwave phase measurements could not. This thesis seeks to develop a viable electrostatic (Langmuir) probe system at the KU PRL, develop a framework to analyze BCl_3/N_2 plasmas using He, N_2, and BCl_3 as bases, and to provide results from various BCl_3/N_2 plasmas that can be further interpreted to explain the etch rate increases.

2.4. Langmuir Probes

Langmuir (electrostatic) probes have a long history of use in analyzing simple plasma discharges. Unfortunately, both their apparent simplicity and cost effectiveness are mitigated by disparity in measured parameters under “similar” conditions. To further complicate issues, Langmuir probes have rarely been used to measure anything but single constituent plasmas under actual processing conditions, though a quick search of the literature will find many different studies that employ electrostatic probes. The fastidious cleaning required prior to each probe sweep also limits their use in common processing gases. Nonetheless, they are able to measure, albeit with increasing difficulty, V_f, V_p, kT_e and N_e if the distribution of electrons is Maxwellian, a good estimate of the EEPF and EEDF, a good estimate of $<\varepsilon>$ (or of an effective kT_e), N_e, I_+, I_e, I_-, the exact EEPF and EEDF, and $<\varepsilon>$.

Several previous papers have examined the EEDF of N_2 plasmas using Langmuir probes, particularly because of an interesting feature that is missed unless the EEDF is examined [13-15]. Other papers have looked at the effects of RF generated plasmas on basic Langmuir probe theory, and still others have critiqued some of the underlying assumptions that have been made in the case of electronegative plasmas such as those containing BCl_3 or SF_6 [16-26]. This shows that the literature is still evolving and

that problems are still often encountered, particularly when diagnosing real-world processing plasmas.

The closest any studies have come to using a Langmuir probe under similar conditions are when Howard used a Langmuir Probe in his research to find the positive ion density and what was reported as kT_e for a select number of BCl_3/N_2 concentrations and when G. Hebner and C. Fleddermann [27] attempted to use a Langmuir probe to measure the electron characteristics of N_2 addition to BCl_3 plasmas in an ICP. Howard did not, however, examine the EEDF nor did he use the kT_e values that he derived to attempt to explain the increase in etch rate while Hebner and Fledderman mentioned their attempt but did not publish any results because of concerns about reproducibility and believability.

Chapter 3. Review of Relevant Plasma Physics

3.1. Plasma Physics Review

A plasma is an ionized gas. It can be either fully ionized or partially ionized, but it must have a sufficient number of ionized particles (electrons, positive ions, or negative ions) to affect its macroscopic physical, electrical, and perhaps chemical properties. It then becomes conductive, begins to exhibit other electrical and physical properties, and its constituent particles interact collectively to create unique phenomena because of the interaction of the separated charged particles.

If one looks at a plasma in isolation, such as a plasma in outer space, or a volume of bulk plasma that is sufficiently far away from any other state of matter, several properties become clear. First, the sum of the charges of the negative and positive charge carriers is equal to zero when summed over a large volume (i.e., a large number of particles is observed). Second, while the net charge of the volume is zero, the particles inside it are actively attempting to recombine into stable molecular or atomic species via the electro-magnetic forces that are created because of the charge separation. These forces cause the charge carriers to cease their purely random motion and to accelerate toward (or be repelled by) the electric fields created by the other charge carriers. Third, because of the

lack of boundaries of an isolated plasma, charge carriers that enter the plasma replace those that escape it.

Any time a non-plasma object comes in contact with a plasma, the lighter, more quickly moving electrons collide with its surface more frequently than the heavier, positively or negatively charged ions. Because these interactions result in charge transfer, the object quickly acquires a negative charge relative to the plasma. If the object is electrically insulated (or non-grounded) this accumulated charge then repels increasingly energetic electrons until only the few electrons with a kinetic energy above a certain threshold can overcome the object's electric potential barrier. The more massive positive (or negative) ions do not move as quickly even when they are attracted to (or repelled by) the negatively charged object, and so are only termed to "drift" towards (or away from) it. Provided there are enough electrons in the plasma, the negative charge on the surface continues to accumulate, repelling negatively charged particles (ions and electrons) and attracting positively charged ones (ions) until the sum of the electron and negative ion flux is equal to that of the positive ions. The volume of influence of this electric field is termed the Debye sheath or the plasma sheath. (N.B: This is different from the Debye radius, which is the characteristic radius of influence of a charged particle within a plasma.)

V_p (the plasma potential) is physically the average electric potential that exists on a scale smaller than that of the Debye radius (wavelength or length—λ_D) between the individual charged particles within a plasma. In this context, however, it also corresponds to the voltage at which the probe is at the same potential as the plasma. At this probe bias voltage, all the charge carriers (mostly electrons) that cross the probe tip's boundary—high and low energy alike—are captured by the probe. Because the probe must have a path to ground to achieve this voltage, the accumulated negative charge these carriers transfer to the probe drains off the probe to ground through the voltage source. This is equivalent to having a positive current being emitted by the probe.

Despite the quasi-neutrality of bulk plasmas, the small reduction of negatively charged particles (mostly electrons) around the edges of the plasma generates a positive V_p throughout the plasma. The typical capacitively coupled plasma (CCP) RIE chamber geometry and the circuit used to generate the plasma allows these electrons to escape in larger numbers than in other plasma systems. The typical CCP chamber, like the PlasmaTherm 790 used in the KU PRL, is composed of an electrically grounded chamber housing and a powered electrode that is DC isolated from the chamber RF power source by a capacitor and is physically isolated from the chamber housing. A high power RF signal is sent

through the electrode and induces an oscillating electric field between the electrode and the chamber housing. The few free electrons that are normally present in any gas respond to this oscillation by accelerating toward and away from the electrode. When these electrons inevitably collide with parent molecules in the source gas they sometimes knock other electrons out of the outermost molecular or atomic orbits ionizing the gas. The original and new free electrons continue to be affected by the electric field and an avalanche of ionization begins. A portion of this cloud of free electrons then collides with both the chamber housing and the electrode. The electrons that collide with the housing drain off because the chamber is grounded, while the electrons that collide with the electrode are trapped by the DC blocking capacitor and build up a negative charge. Since the only sources of electrons in the system are the outermost orbits of the parent molecules, the plasma becomes positively charged and thus V_p is noticeably positive. This phenomenon also explains why the electrode becomes negatively charged leading to a negative DC bias voltage with respect to ground. This DC bias attracts positive ions across the sheath and these ions bombard the substrate, reacting and consequently etching it.

One can quickly infer that if the difference between V_p and the electrodes changes, the sheath will have to change to compensate. This

change can take on many forms but if the potential difference is large enough it generally changes the dimension of the sheath. (Although the term sheath height, radius, or length is often used informally depending on the inducing electrode's geometry.) If the difference in potential is small, the compensation does not affect the sheath dimension, and instead the sheath itself adjusts internally. This adjustment forms the basis for Langmuir probe theory. However, because each plasma is a unique mixture of negative ions, positive ions, and electrons it will react similarly but not identically to minute perturbations, leading to the wide ranging experiments using Langmuir probe studies.

Chapter 4. Langmuir (Electrostatic) Probe Description

4.1. Background

At its simplest, a Langmuir probe is any small piece of metal that is inserted into a plasma to measure its characteristics. To make use of its probing capabilities, however, requires that a voltage source bias that piece of metal from below a potential where the electron flux does not significantly mask the positive ion saturation current to a few volts above the electron saturation potential where the positive ion flux is negligible. In addition, if the plasma source varies with time, a filtering scheme (either passive or active) is required to suppress the primary RF driving frequency and mitigate the inevitable high frequency oscillations that an RF plasma power source creates.

4.2. Preliminary Electrostatic Probe Theory

A Langmuir probe sweep characteristic is essentially a measurement of a DC voltage-current pair taken at many different voltage points. Each voltage point corresponds to a different current that reflects the energies and density of positive ions, negative ions, and electrons that are attracted to or repelled by the probe tip. The sweep can be fundamentally divided into three regions based on the voltage applied to the probe (the probe bias—V_b). The first is the positive ion collection region. This region

corresponds to a strongly negative probe bias in relation to the plasma potential (V_p). In this region the probe is biased so negatively that all the electrons and negative ions are repelled from its surface and only positive ions are collected. Because of this, and the relatively standard definition that positive charge flow away from the probe tip is positive, the probe current is negative and only positive ions affect the probe response if there is a decrease in the bias. The second region is the electron saturation region. This corresponds to the region where the probe bias is a few volts higher than V_p. In this region the probe surface collects all the electrons and negative ions that come in contact with the sheath surface. In this range, the potential barrier effectively repels all of the positive ions from the collecting surface and therefore the current overwhelmingly consists of electrons and negative ions. In a similar (but opposite) fashion to the positive ion collection region, the probe response here depends only on electrons and negative charge carriers if the probe bias is increased. The third region is the transition region. This is where both high energy electrons that are able to overcome the potential created by the probe tip and the positive ions contribute to the probe current. Within this region, a special point exists called the floating potential (V_f). This is the potential (or voltage) where the sum of the charges of the positive ions, negative

ions, and electrons that are collected by the probe result in a net zero current.

Ideal Langmuir Probe Behavior in a DC Plasma of a Single Species

While Langmuir's original work and several other more recent monographs and articles [28-33] admirably explain the basic principles of electrostatic probes, a brief visualization of an ideal probe characteristic may help guide the reader throughout the rest of this thesis.

The probe current comprises two competing currents—the positive charge carrier current (positive ion current, I_+) and the negative charge carrier current. In plasmas that ionize predominantly into positive ions and electrons, called electropositive plasmas, the negative charge carrier current is the electron current (I_e). In plasmas that have a sufficient number of negative ions so as to influence the plasma, termed electronegative plasmas, the negative charge carrier current is the sum of I_e and the negative ion current (I_-). In this example, I_- is taken to be zero. If one does not attempt to take sheath expansion into account, and if the thermal energy of the electrons is much greater than the thermal energy of the positive ions ($kT_e \gg kT_+$), which is typically true,

$$I_+\left(V_b\right)=\begin{cases} I_{+sat}\exp\left(\dfrac{q_e\left(V_p-V_b\right)}{kT_+}\right) & \text{when } V_b \geq V_p \\ I_{+sat} & \text{when } V_b < V_p \end{cases} \tag{4.1}$$

where $I_{+sat}=0.6\cdot q_e\cdot N_+\cdot A_{probe}\cdot\sqrt{\dfrac{kT_e}{m_+}}$, the Bohm Current, and

$$I_e\left(V_b\right)=\begin{cases} I_{esat}\exp\left(\dfrac{q_e\left(V_b-V_p\right)}{kT_e}\right) & \text{when } V_b \leq V_p \\ I_{esat} & \text{when } V_b > V_p \end{cases} \tag{4.2}$$

where $I_{esat}=\dfrac{1}{4}q_e\cdot N_e\cdot A_{probe}\cdot\sqrt{\dfrac{8kT_e}{\pi\cdot m_e}}$, the random electron current. This results in the type of curve seen in Figure 4.3. This oversimplifies the probe characteristic because the electric potential sheaths do not expand as they must in order to retard the positive ions and electrons in the regions slightly above and below Vp, nor do they continue expanding as the bias spreads away from V_p. Still, the transition region from V_f to V_p is similar to what one would expect in a well-behaved DC plasma with no collisions in the sheath (such as the plasmas found in fusion Q-machines) and the knee that one sees at V_p is one of the first indicators of a "good" I-V characteristic.

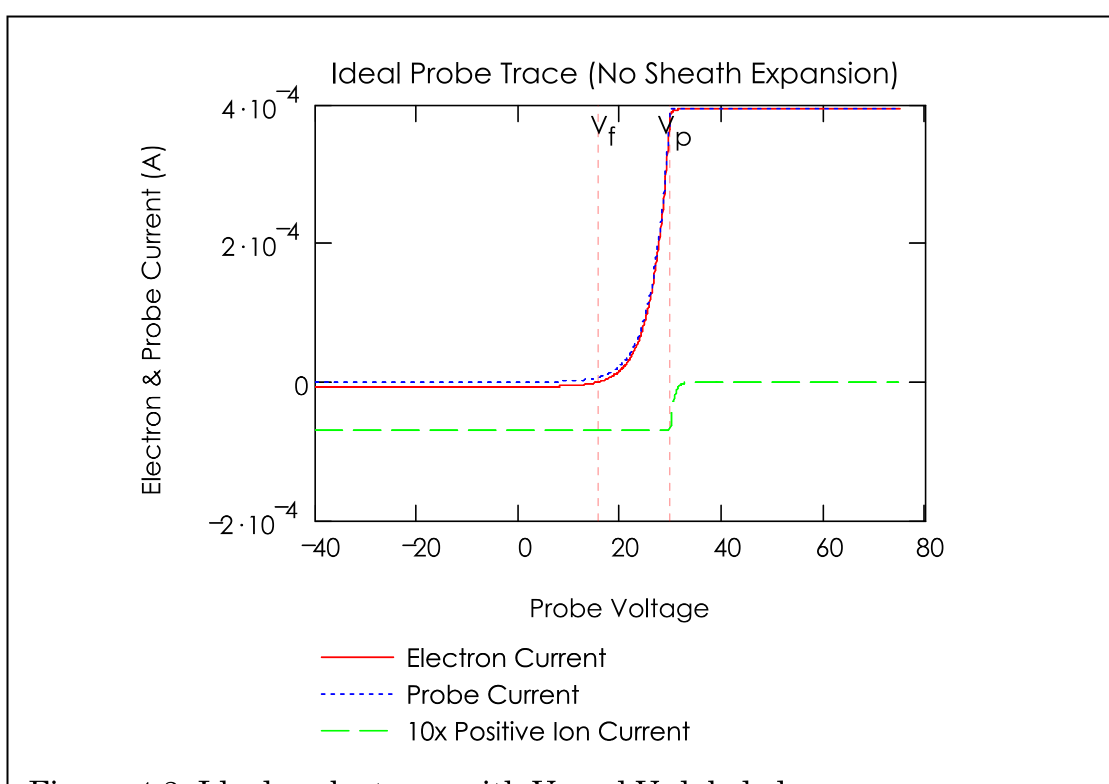

Figure 4.3: Ideal probe trace with V_f and V_p labeled.
The positive ion mass is taken to be that of helium.

Such clean curves were indeed found by Langmuir, Druyvesteyn, Chen and others working in the realm of fully ionized plasmas, validating the original Langmuir probe theory. Unfortunately, to quote Francis Chen (a well respected electrostatic probe researcher) after he presented several examples of Q-machine I-V characteristics: "Such nice exponentials were never seen again!" This is emblematic of the realities of today's plasmas, which are inevitably time varying and usually collisional.

4.3. Practical Considerations in an RF driven processing plasma

Langmuir originally developed electrostatic probes in inert DC discharges or glows (i.e., with a steady electric field inducing the plasma, and in Ar, H_2, or He) [29]. Because of the static nature of those plasma sources, the electric potential of the plasma, the driving electrode, and the direction of electron flow did not vary with time. This allowed the difference between the plasma potential and the probe bias voltage to remain constant for each point on the characteristic curve. Further, because the gases were inert and non-reactive, there was relatively little chemical interaction between the plasma and the probe tip. (Although the reader should note that this does not mean that the two did not interact at all.) In modern processing plasmas, however, the plasma source is rarely static and the gases are always reactive—less so with the probe tip than

with the substrate, but they still react. Specifically, the KU PRL PlasmaTherm 790 receives power from a 13.56 MHz RF generator that connects to the biased electrode via two coaxial cables and the plasma parent gases in this study are He, N_2, and BCl_3. These realities ensure that the plasma oscillates at 13.56 MHz, introduce the possibility of a non-sinusoidal driving function, and guarantee that the plasma species will quickly affect the electrical characteristics of the probe tip.

Time Varying, RF Plasma Source

If one simply ignored the existence of the RF oscillations and used a non-compensated probe to measure the I-V characteristic in an RF plasma, the RF interference would effectively obscure the target measurements. To quote Paranjpe et al. [25], "Numerous papers have demonstrated the perturbing effects of [RF] interference on the single probe characteristic." This comment rings true because even the simplest Helium and Argon plasmas do not behave nearly as well when they are created with an RF source because of the dynamic electric fields to which the plasma species are subjected. Unlike the Q-machine or other DC plasmas where the electric field used to ionize the parent gases is constant, the RF sources in a CCP accelerate electrons back and forth between the electrodes (or more accurately their accelerating sheaths) until the electrons collide with some particle—more than likely a parent

molecule—dissociating, ionizing, exciting, or attaching to it. Meanwhile, the ions formed react to the changing field much more slowly, and are largely unaffected by the rapid changes in the electric field. Unfortunately, this still means that the electric potential between the DC probe bias and the plasma is rapidly changing in the all-important transition region. Even if one relies on the "average" DC value that the ammeter provides, because of the non-linearity of the I-V curve, the knee will effectively be obscured and the transition region deformed as seen in Figure 4.4.

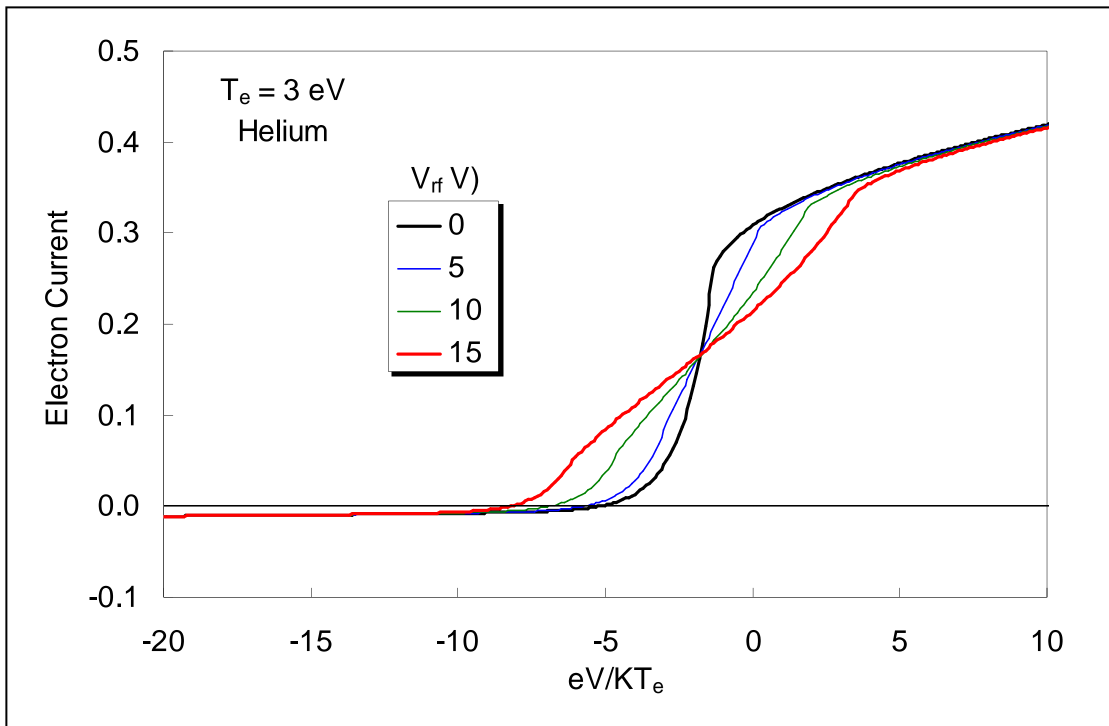

Figure 4.4: Illustration of various levels of RF distortion of the electron current [19].

Unless one uses an extremely fast volt/current meter to attempt to capture the time resolved data, the probe must either suppress or mimic and ride the RF signal used to create the plasma. While each of these options have their own disadvantages ranging from an unknown response of sheath potential drop to a strongly nonlinear current response, various researchers have tried them all, and Annaratone et al, even compared the passive and active probe methods [18]. This remains an active area of research with recently issued patents [22]. Because of the nascent nature of Langmuir probe research in the KU PRL, we opted for the simplest method of the three—suppression and filtering. With this scheme it does not matter if the driving signal is non-sinusoidal or out of phase with the source. We focused on designs used by both Chen and Hopkins to passively filter the RF from the plasma signal [15, 19, 34]. The section on experimental setup will provide further details of the filtering scheme.

Plasma-Probe Tip Interactions and Probe Tip Contamination

By design, the probe tip interacts with the plasma. Without charge transfer, no current would pass through the probe and this would render the probe useless. However, because ions and electrons collide with the probe, one is guaranteed that they will interact both physically and perhaps chemically (especially in reactive plasmas). Further, the ions that

collide with the probe are often the same species of ions that will eventually react with and etch the substrate, and some of the electrons have the same energies as the ones needed to dissociate parent molecules in the plasmas into their constituent ions. This is a perfect recipe for probe tip contamination and while it is beyond the scope of this thesis to discuss its exact modalities, suffice it to say that a dirty, contaminated probe is the bane of an accurate I-V curve and consequently every value derived from it is suspect.

Because of the need to ensure probe cleanliness, every researcher must develop a cleaning protocol for the Langmuir probe tip *in situ*. Authors explain that these range from simple electron bombardment at high bias voltages to more elaborate cleaning techniques that involve both ion and electron bombardment [3, 15, 30, 35-37]. Oftentimes, as the plasma becomes more reactive and complex, the cleaning technique becomes more stringent and complex as well. At the KU PRL, BCl_3 necessitated a more involved cleaning than did He and N_2, and plasma mixtures such as BCl_3/N_2 contaminated the probe very quickly after cleaning, necessitating changes in experimental protocol to avoid corrupting the I-V characteristic.

4.4. Interpreting the Probe Sweep

As mentioned previously, a Langmuir probe is only useful when it is swept through a range of voltages. These voltages are related to the electric field strength generated in the plasma and corresponding energy of the collected charged particles.

In the case of the positive ion collection or positive ion saturation region (i.e., when $V_b << V_p$ and $V_b << V_f$), the strong negative voltage applied to the probe creates an electric field that collects positive ions with increasing energy until 1) the electric field is sufficient to prevent all the electrons and negative ions from hitting the probe and 2) all the positive ions are collected from the sheath. In this region, any decrease in potential results not in an increase of collected ions per unit of sheath area; rather, it increases the volume of the sheath and consequently its surface area. The effect of that surface area increase on probe current has been modeled by Z. Sternovsky as a polynomial with linear dependence on the applied voltage and square root dependence on the absolute value of the applied voltage relative to V_p [38].

In the case of the electron saturation region (i.e., when $V_f > V_p$), the strong positive bias applied to the probe creates an electric field that collects all the electrons and negative ions from the probe sheath and

repels all positive ions. Though for a small voltage bias above V_p, the positive ion current decays exponentially, past this often insignificant region, any increase in the potential results in an increase in the volume of the sheath and its surface area. The effect of that surface area increase on probe current has again been modeled by Sternovsky and varies linearly with increased applied voltage [38].

The region of most interest is the region from slightly below V_f to V_p. In this region, the current gives a good representation of the total number of electrons collected by the probe, and consequently the total number of electrons below a given energy threshold. There is an offset because of the positive ion current, but because more and more positive ions are being repelled as the bias voltage is raised, the effect of the positive ion current becomes more and more negligible. Further, since the positive ion current is composed of heavier particles that do not have the same charge to mass ratio, they will not respond as dramatically as electrons to the change in probe potential. This asymmetrical effect results in a lower positive ion current in comparison to the current that the highly mobile electrons create.

Finding V_p

Knowing the plasma potential is important because it determines the origin for the EEDF and is used in all other methods of determining both $<\varepsilon>$ and kT_e. At V_p, there is no sheath around the probe tip and only the random flux of electrons, positive ions, and if present, negative ions determines the probe current. Traditionally, any analysis begins by estimating V_p as the voltage where the current slope is maximized. This leads to either calculating the first derivative of the slope and finding its maximum, or calculating the second derivative and finding where it crosses zero. Realistically, because of the increase in noise inherent in the process of taking derivatives, the (first) maximum of the first derivative is always used.

Laframboise Correction

In 1966 Laframboise investigated the non-ideal nature of single probe I-V sweeps [39]. He concluded that the zero-second derivative method underestimated the true value of V_p. Further, this underestimation was based on the non-ideal saturation of the positive ion and electron currents. Laframboise put forth the idea that the ratio of the Debye radius to the probe radius could be used as an indicator of sheath expansion which influenced the shape of the ion and electron saturation curves and consequently the correction required to find V_p. His very complete

experimental work gave rise to a new generation of papers that parameterized his ion current curves while at the same time expanding his theory to almost-Maxwellian and slightly collisional plasmas [23, 40, 41]. As Laframboise was mainly interested in the proper placement of Vp and finding kT_e, his papers hinted at what Karamcheti and Steinbrüchel explicitly stated: “A linear extrapolation of $[I_+(V_p)]$ is often adequate for determining the electron temperature,… [23].”

To this end, the Laframboise correction typically linearly extrapolates the electron saturation current and the exponential in the transition region to find a more accurate V_p at the intersections of these two lines. This new value of V_p can then be used to calculate kT_e and N_e. For example, Figure 4.5 illustrates how the second derivative method would estimate V_p=18.8 V, while the Laframboise correction would increase it to V_{pLF}=20.8 V. This correction can be incorporated into the SmartProbe Method [42], and is used to augment it if there is concern that the sheath expands rapidly enough to discernibly impact Vp. While this correction does not incorporate the entirety of Laframboise theory, it is the first step in correcting for sheath expansion in plasmas.

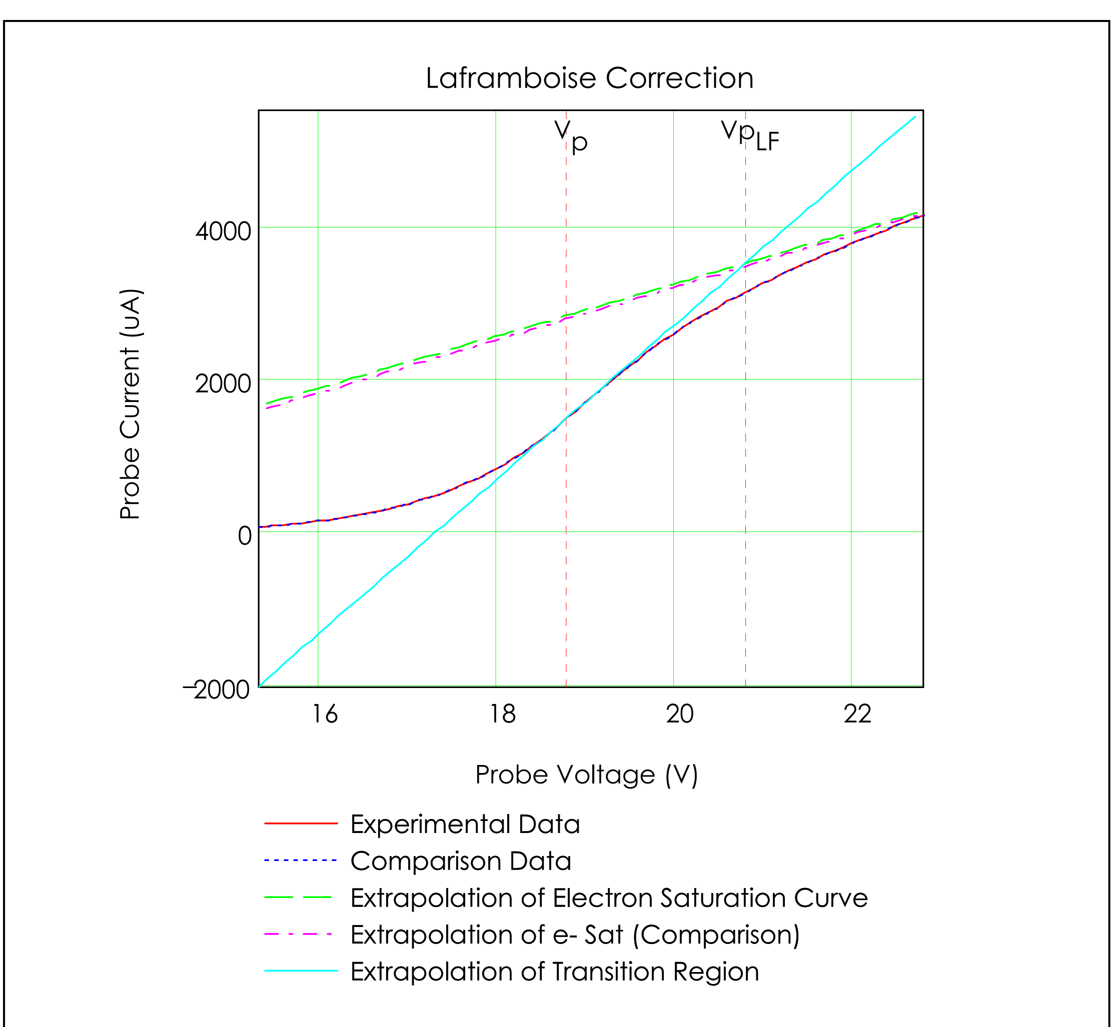

Figure 4.5: Graphical example of Laframboise correction to V_p.

A more accurate estimate of V_P is located at the intersection of the extrapolated lines.

The Electron Energy Distribution Function (EEDF)

Like any statistically characterized system, the free electrons in a CCP plasma are not all at the same energy. While the main force that initiates the electrons' motion is the RF oscillation, a myriad of forces including collisions with other species in the plasma influences each electron and therefore the electrons take on a variety of speeds and corresponding energy levels. The resulting distributions give insight into the kinetics of the plasma, the reactions that occur, and how the driving electrical forces are converted to particle motion. Because this thesis focuses on the average electron energy, it will focus on the electron energy distribution function (EEDF) and not work with the electron velocity distribution function (EVDF) which can be derived from the EEDF.

An accurate EEDF is the definitive way to measure both the average electron energy and electron density of a plasma as described in Equations (4.3) and (4.4).

$$N_e = \int_0^\infty EEDF(\varepsilon)\,d\varepsilon \tag{4.3}$$

$$\langle \varepsilon \rangle = \bar{\varepsilon} = \frac{\int_0^\infty \varepsilon \cdot EEDF(\varepsilon)\,d\varepsilon}{\int_0^\infty EEDF(\varepsilon)\,d\varepsilon} \tag{4.4}$$

where $\varepsilon = V_p - V_b$. Experimentally observed distributions vary tremendously and can be of any shape. For example, a nitrogen plasma EEDF has been observed to have a "hole" between 2 and 4 eV for certain pressures and powers in the GEC Reference Cell because the N≡N bond resonates at that energy [13, 15]. While initially suggested by Langmuir, Druyvesteyn [28] demonstrated that the second derivative of the electron current in the transition region of a Langmuir probe sweep was proportional to what is termed the electron energy probability function (EEPF) through the Druyvesteyn formula

$$EEPF(\varepsilon) = \frac{2\sqrt{2 \cdot m_e}}{q_e^{\ 3} \cdot A_p} \cdot \frac{d^2 I_e(\varepsilon)}{d\varepsilon^2} \tag{4.5}$$

where m_e is the mass of an electron, q_e is the elementary charge, A_p is the area of the probe tip, and $\frac{d^2 I_e(\varepsilon)}{d\varepsilon^2}$ is the second derivative of the probe electron current in units of A/V^2. Further, he showed that the EEPF was related to the EEDF by the relation in Equation (4.6):

$$EEDF(\varepsilon) = \sqrt{\varepsilon} \cdot EEPF(\varepsilon). \tag{4.6}$$

Druyvesteyn's work provided the bridge between the probe characteristic and the EEDF for any non-concave (typically planar, cylindrical, or spherical) probe tip geometry. As a side note, the term

EEPF can be a bit confusing and the reader should be aware that the EEPF is not a true probability distribution because its integral is not equal to one.

While the EEDF is a highly effective method for finding the average electron energy and electron density, it suffers from a number of drawbacks. First, because ε relies on knowing V_p, it can easily be skewed. Second, the EEPF relies on the second derivative of the electron current and taking the second derivative magnifies the noise in the transition region which already has a low signal to noise ratio because of the inherent thermal and RF noise and a signal that peaks at values on the order of 0.5–1.5 mA. Third, because $I_e(\varepsilon)$ is the electron current and not the raw probe characteristic, a correction for the positive ion current must be made to obtain accurate values of the EEDF at higher energy values. Nonetheless, even an approximate EEDF provides insights that cannot be gleaned from the other methods that will be described that avoid some of the EEDFs pitfalls.

The Log-Slope method

The simplest, time-honored, and original method for analyzing the probe characteristic is the Log-Slope method. Langmuir [29] first proposed this method as an effective analysis for the original DC glow discharges

that he later called plasmas. It assumes that the EEDF of the bulk plasma electrons is Maxwellian. Because a Maxwellian distribution of electrons is described by

$$EEDF_{Max}(\varepsilon) = N_e \cdot \frac{2}{\sqrt{\pi \cdot kT_e^3}} \cdot \sqrt{\varepsilon} \cdot \exp\left(-\frac{\varepsilon}{kT_e}\right), \tag{4.7}$$

the EEPF, the first derivative, and the electron current all can be described as exponentials. Specifically, the electron current in the transition region (i.e., $V_b < V_p$) is described by

$$I_e(V_b) = I_{sat} \cdot \exp\left[(V_b - V_p) / kT_e \right]. \tag{4.8}$$

As described previously, when the probe potential approaches V_p, the probe current approaches the electron current and the positive ion current becomes negligible (more or less so depending on the mass of the positive ions). So near the plasma potential, the slope of the logarithm of the probe current becomes proportional to the inverse of the electron temperature.

$$\ln\left(I(V_b)\right) = 1/kT_e \cdot V_b + \ln\left(I_{sat}\right) - \frac{V_p}{kT_e}. \tag{4.9}$$

This allows for a simple analysis of the probe curve. First one takes the natural logarithm of the probe current and fits a line to the section of the curve closest to V_p. Then the inverse of the slope of the line is equal to the

electron temperature. Fortunately, when the EEDF is Maxwellian, the average electron energy is then equal to three halves ($\frac{3}{2}$) of the electron temperature.

One of the advantages of the Log-Slope method is its simplicity once V_p is found. Another of its advantages is that if V_p is not clear, the fit to an exponential can be moved a bit lower and further away from a possibly incorrectly estimated V_p. This will still give the same value for kT_e provided that the ion current is not sufficiently large to distort the exponential. Its major downfalls are that is often does not take into account a large section of the I-V curve, it requires that the EEDF be Maxwellian, and that there ideally should be no significant ion (positive or negative) component in the region used to fit the exponential.

The SmartProbe Method

The SmartProbe method [43] is similar to the Log-Slope method in that it assumes that the EEDF follows a Maxwellian distribution. The difference, however, is that it decreases the dependence of the kT_e calculation on the numerical differentiation method and resulting individual slope calculations at each point in the logarithm of the I-V curve.

Recall that for a Maxwellian EEDF the electron current takes on the form of Equation (4.8) and that

$$\int_{-\infty}^{V_p} I_{sat} \cdot \exp\left[\left(V_b - V_p\right) \big/ kT_e \right] = kT_e \cdot I_{sat} \cdot \exp\left[\left(V_b - V_p\right) \big/ kT_e \right]. \qquad (4.10)$$

From this, one can find an excellent estimate of kT_e from

$$kT_e = \frac{\int_{-\infty}^{V_p} I_e(V)dV}{I_e\left(V_p\right)} \approx \frac{\int_{V_f}^{V_p} I(V)dV}{I\left(V_p\right)} \qquad (4.11)$$

provided that the ion current is sufficiently low in the transition region and $V_f < V_p - 3 \cdot kT_e$ for a 5% error. Because both the ion current and the discarding of the low V portion of the sweep depress the value of $\frac{\int_{V_f}^{V_p} I(V)dV}{I\left(V_p\right)}$, one expects the values of kT_e found by the SmartProbe method to be slightly lower than the actual value of kT_e.

Despite the errors that are inherent in its formulation, the SmartProbe method is very useful in many less than optimal circumstances. For example, when the EEDF is more or less Maxwellian but has some discontinuities such as in the case of N_2, it allows for an accurate measurement of kT_e without the noise inducing double differentiation that would be required to find the location of the possible “hole” in the

Maxwellian. It is also useful as an automated method of calculation, particularly in the cases when probe sweeps are noisy and smoothing would excessively smear out the I-V characteristic.

4.5. The Effect of Negative Ions and (Charged) Metastables on the Second Derivative of the I-V Characteristic

Most plasmas are electropositive. This means that the ionized components of the plasma consist of electrons and positive ions. Historically, Langmuir probe theory assumed this, and only upon further investigation were negative ions included in the analysis. Further, if a plasma contains enough negative ions that they need to be taken into account because they affect the plasma's behavior, the plasma is termed electronegative. Unfortunately, the first attempts to fit a theory that would characterize these plasmas contained a mathematical inconsistency that propagated throughout the field through textbooks despite being corrected in an earlier journal article [20, 44].

Fortunately, H. Amemiya experimentally observed the Langmuir probe response to an electronegative plasma and identified both the current and features of the second derivative the negative ions and metastable negative species induce [16, 17]. Since our experiments use BCl_3 as a primary parent gas, and it results in an electronegative plasma, these particular features become extremely relevant when observing our

Langmuir probe results. Figure 4.6 shows both the ideal and actual cases for negative ion current and its second derivative (i_-'' in the figure, I_-'' in this thesis). The local minimum seen in the actual second derivative results from a reconfiguration of the sheath around the Langmuir probe. It is the point at which the slow negative ions reach a critical ratio with the remaining fast electrons in the sheath and change the response of the sheath from one dominated by electrons to one dominated by negative ions. This reconfiguration of the sheath momentarily slows down the increase in negative charge carrier current and creates the local minimum in the second derivative preceding the negative ion peak.

Amemiya also discusses the matter of negatively charged metastable species. Citing Wiesemann [45], he warns that these species result in a secondary electron emission spike similar to $-i_+''$ in Figure 4.6 just above V_p. When these metastables collide with the probe, they relax back to a lower energy state releasing energy in the form of electrons. These electrons are then rapidly recaptured by the probe, resulting in a spike in the second derivative. Amemiya also notes that this spike should be discriminated from the spike caused by negative ions that should appear just below V_p.

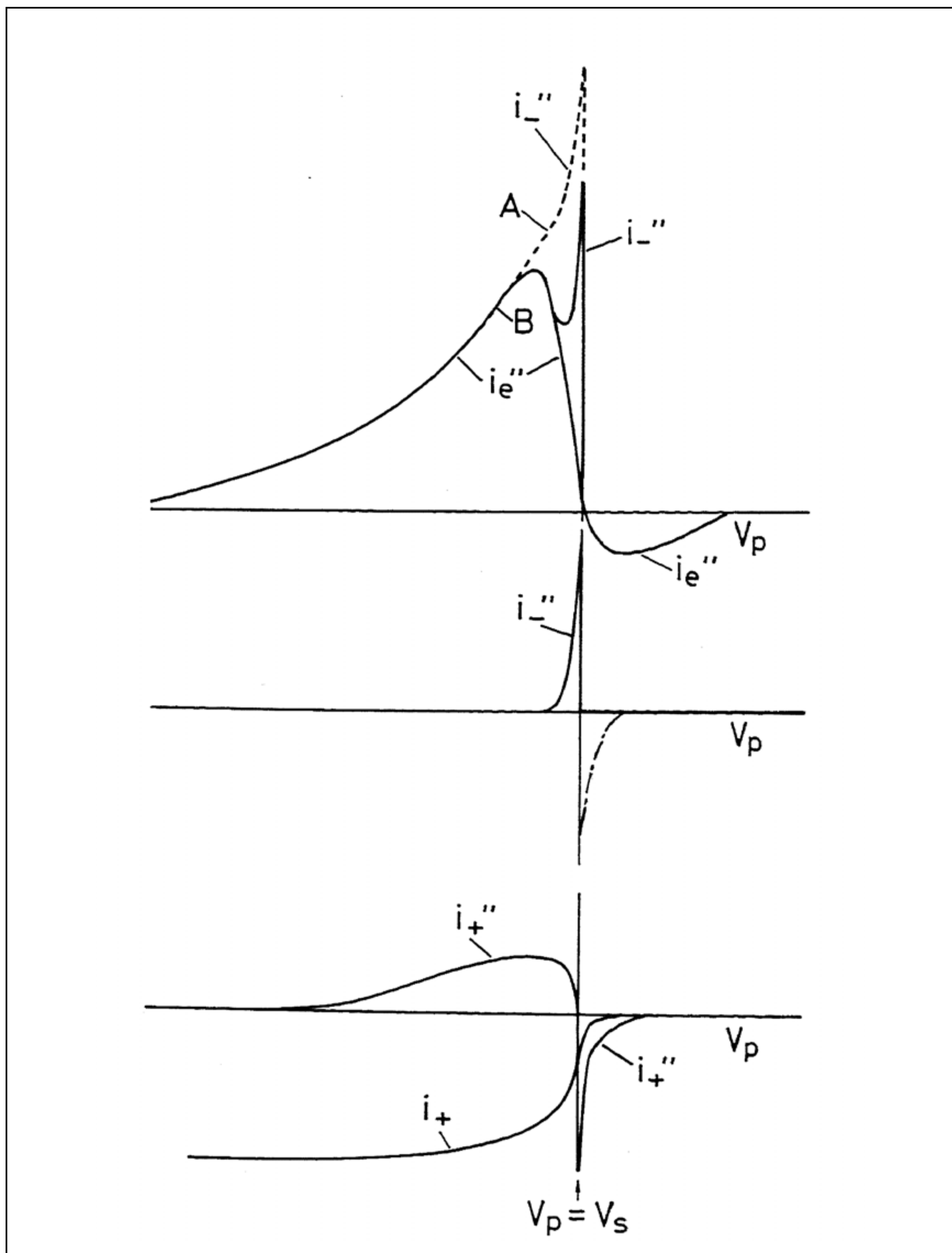

Figure 4.6: Schematic drawings of the positive ion current (i_+) and the second derivative of the electron, negative ion, and positive ion currents (i_e'', i_-'', i_+'') [16]. Dotted curve: ideal case; solid line: actual observation.

Chapter 5. Experimental Setup & Protocol

The experiments consist of collecting information that can be analyzed to infer the characteristics of different plasmas created in a PlasmaTherm 790 Series chamber with a Langmuir probe using the associated data acquisition system. To this end, several sections will provide a brief description of the equipment involved in each sub-system of the apparatus and a detailed description of its role in the experiments. Figure 5.7 shows a schematic of the entire system and may be useful as an overview before delving into specifics. This chapter presents an outline of the experimental and analysis protocol along with parameters common to the experimental runs. Any significant variations will be summarized and the specific variation used to characterize a particular set of parameters (chemistry, power, pressure) will be mentioned in the corresponding results sections. It is worth noting that many experimental variations yielded a few choice examples that nicely illustrate the controlling phenomena, and that the underlying experimental philosophy remained the same throughout the data collection and analysis process.

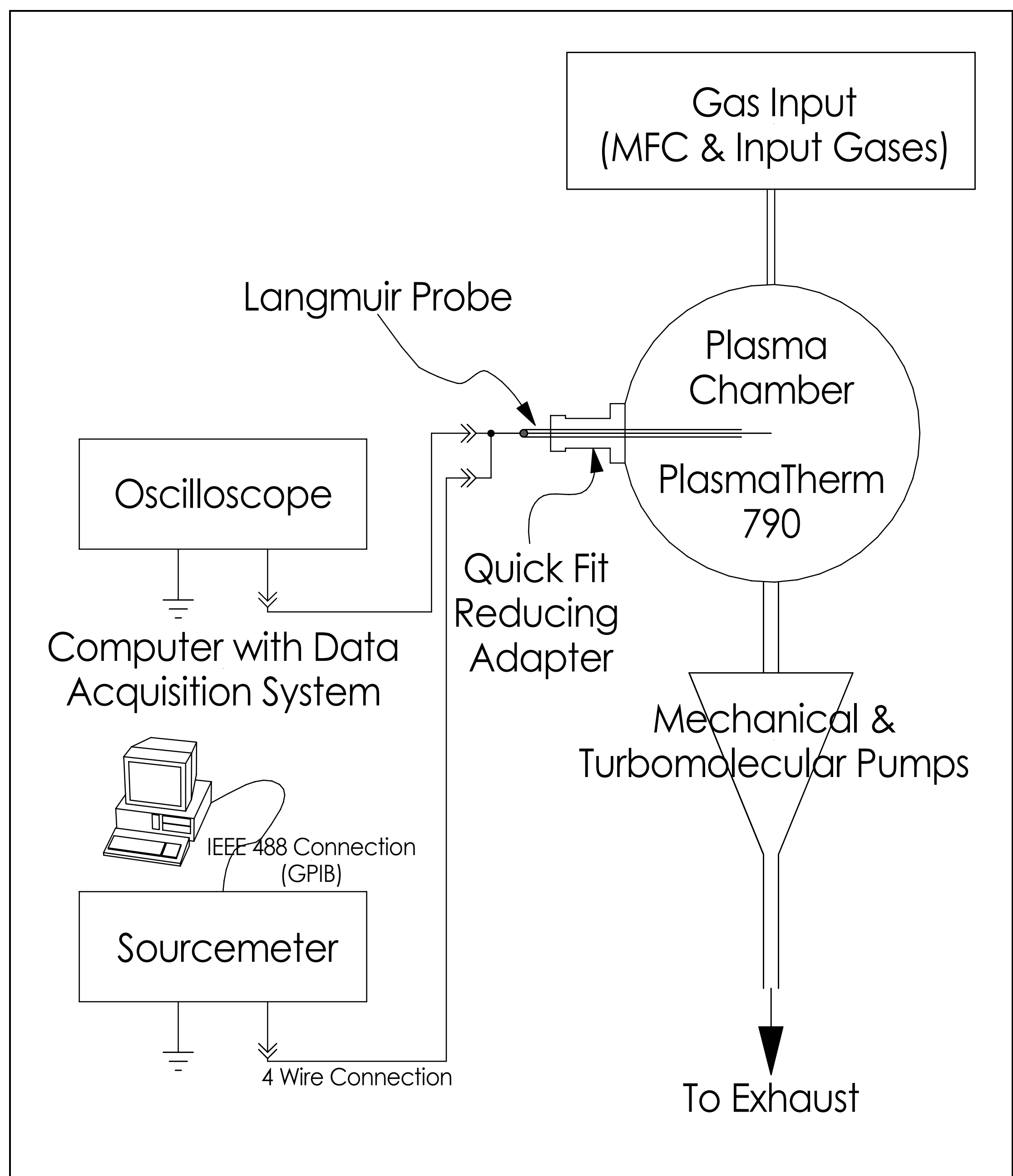

Figure 5.7: Schematic of experimental apparatus used in Langmuir probe studies.

5.1. PlasmaTherm 790

The experiments were performed in a PlasmaTherm 790 Series capacitively coupled parallel plate system. Figure 5.8 is a schematic prepared by J. Sia that shows the basic plasma reactor configuration.

Further details of the system, also prepared by J. Sia, can be found in Appendix A. In our experiments, the Langmuir probe was inserted into one of the three viewing ports using a quick fit reducing adapter. (See Figure 5.7.) Figure 5.9 shows that the distance from the inner wall of the chamber to the end of the probe, counting tip length, is standardized to 7". This corresponds to the probe tip being within 0.5" of the radial center of the chamber and lower electrode during all experiments. A base pressure of 5×10^{-6} Torr was considered acceptable without the quick fit reducing adapter (probe coupler) attached to the system, and because of the probe and coupler seals, a base pressure of 8.0–9.5×10^{-6} Torr was considered acceptable with a probe inserted into the chamber through the coupler.

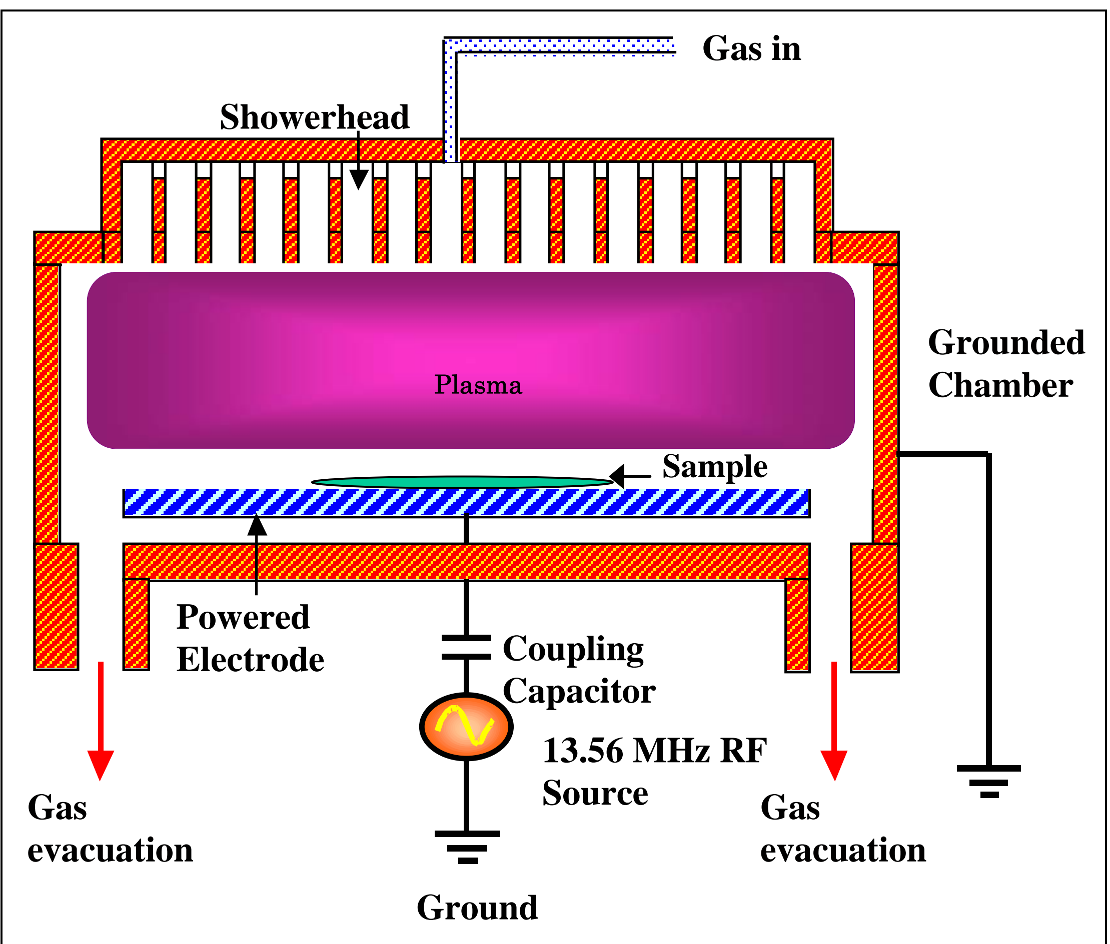

Figure 5.8: Schematic of the PlasmaTherm 790 Series capacitively coupled plasma chamber used in Langmuir probe and etching experiments [6].

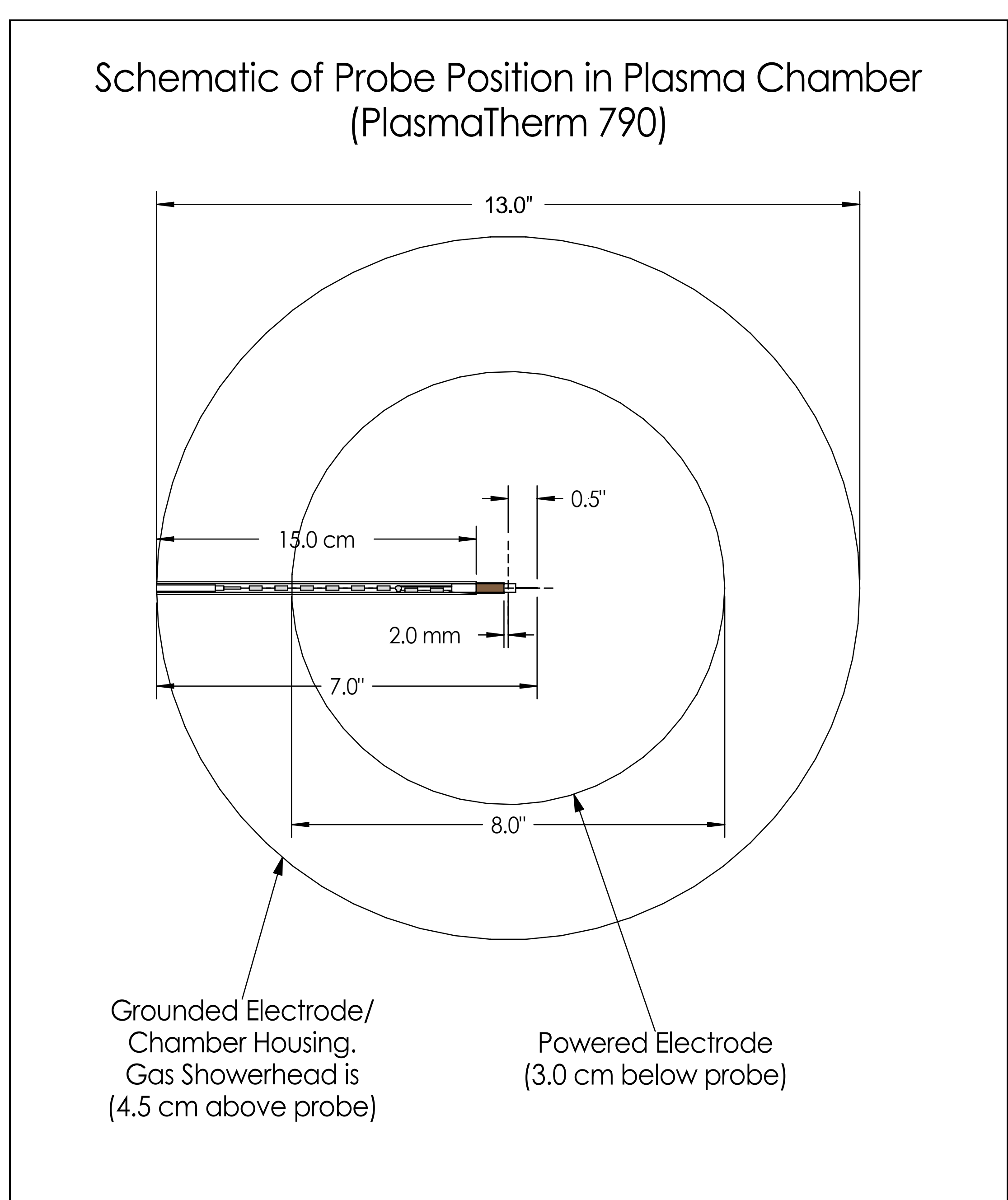

Figure 5.9: Schematic describing the Langmuir probe positioning radially in the chamber.

5.2. Langmuir Probe

In our design of a Langmuir probe, we use a wire for our probe tip giving us a cylindrical Langmuir probe. The wire protrudes from a quartz tube fitted with a ceramic plug on one end and an epoxy plug on the other to keep the probe vacuum tight. A passive RF filtering network connects the probe tip to a lead wire that is swept across a range of voltages by a sourcemeter that also measures the actual voltage applied to and current flowing through the probe (and consequently the plasma). Figure 5.10 exemplifies the KU PRL probe structure and will be useful as a reference as each part is discussed further.

Probe Tip

As mentioned earlier, the probe tip consists of a wire. While different plasma chemistries and pressures require different probe tip sizes and materials, the starting point for most investigations is a platinum tip with 0.25 mm radius and 1.05 cm length.

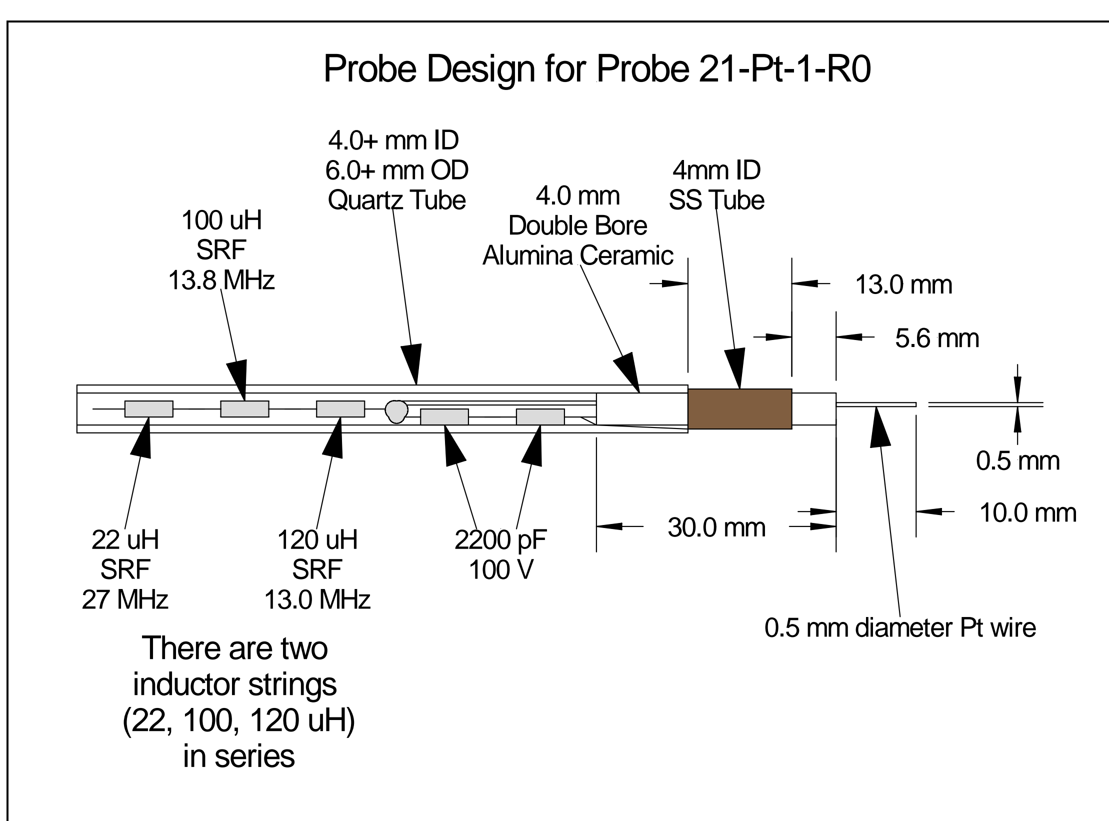

Figure 5.10: Illustration/Schematic of typical Langmuir probe construction. Based on previous designs by Chen *et al.* and Hopkins *et al.* [15, 19, 34].

Table 5.1 below lists the various tip dimensions and materials used. It is indexed by chemistry and pressure range which affects the magnitude of the plasma electron density and Debye radius.

Table 5.1: Probe tip characteristics used for experimental chemistries presented.

Plasma Chemistry & Characteristics	Probe Radius (mm)	Probe Length (cm)	Probe Material
He, 20–140 mTorr, 50–225 W	0.25	1.05	80:20 Ni:Cr
N_2, 10–75 mTorr, 25–300 W	0.25	0.85	99.95% Pt
BCl_3 10–100 mTorr 50–200 W	0.25	0.60	99.95% Pt
BCl_3/N_2 15 mTorr 50 W	0.25	0.80	99.95% Pt

Compensation Electrode and Shield

The compensation electrode for the majority of preliminary Langmuir probes consists of nickel tubing obtained from UTI Corporation (now Accellent Corporation). The tubing's inner diameter (ID) is 4 mm and its outside diameter (OD) is 4.5 mm. In preliminary models of the probe, the compensation electrode is 1 cm long, and has a hole drilled into it to facilitate attaching a nickel lead from the internal passive filter. In the later models of the probe, the compensation electrode consists of a 316 stainless steel tube obtained from Small Parts Corporation. Like the nickel tubing, the ID is 4 mm, and the OD is 4.5 mm. However, because of an improved understanding of the target plasmas, and to counteract possible errors due to Debye length concerns, newer probes used a longer (1.3 cm) compensation electrode.

Probe Body and Housing

The probe housing consists of a 6 mm OD, slightly greater than 4 mm ID quartz tube obtained from the University of Kansas glass blower. As can be seen in the diagram, a 4 mm OD, 0.8 mm ID double bore alumina ceramic tube plugs one end of the tube (Alfa Aesar Stock #32550). The ceramic also acts as a support for the compensation electrode, isolates the electronics housed in the probe from the plasma, and isolates the

cylindrical probe tip from everything but the plasma and the signal port of the RF filtering network.

Internal Probe Electronics

Electrostatic probe analysis in RF generated capacitively coupled plasmas (CCPs) requires that a passive or active filter suppress the RF signal used to generate the plasma. Only then can the probe measure the stationary DC current-voltage (I-V) pairs that make up a sweep. While the active method has the theoretical advantage of using the same RF driving signal as the plasma source to suppress it exactly, we have found that not only does the plasma act as a mixer, but other signals between 13.56 MHz and 27.12 MHz are present. Because of this, we chose to implement a passive filtering scheme.

The minimum passive filtering network consists of a blocking inductor (or RF choke) with a self-resonant frequency (SRF) that corresponds to the plasma frequency in series with the probe tip and a capacitor that smoothes the incoming RF signal that rides the bias potential between the probe tip and the compensation electrode. In practice, because the filtering network should be placed as close to the probe tip as possible, all of the filtering capacitors and inductors must fit inside the quartz tube making up the probe body. No single inductor that can fit into the probe

body can sufficiently attenuate the driving signal at the plasma frequency and its harmonics so a series of inductors commonly called a choke chain must be employed. Further, because the electron bombardment portion of the cleaning cycle subjects the probe tip to voltages that can reach up to 175 V above the plasma floating potential, a series of capacitors must replace the single capacitor. (Again, since no single capacitor that can withstand this voltage can fit into the probe body.)

Manufacturers rarely market inductors with a specific SRF and even inductors with the same ratings will have 1) different SRFs and 2) different impedances at that frequency because of manufacturing differences. Each inductor, therefore, must be tested before it is used in a passive filter. As alluded to previously, the spectral profile of the plasma does not have just one peak at 13.56 MHz. Preliminary tests using a probe with capacitors but no inductor choke chain indicated additional harmonics at both 27.12 MHz and 40.68 MHz. Because of this, additional RF chokes were used in two basic configurations. The first aims to broadly attenuate frequencies above 13.56 MHz while the second focuses on the fundamental and second harmonics.

Table 5.2 below details the inductors used in both configurations. Because the manufacturers list a minimum SRF, the inductors are each

tested with a function generator and an oscilloscope to determine the actual SRF. These particular inductors have been found to have an SRF either at the target frequency (either the fundamental plasma frequency or the secondary harmonic) or slightly below or above it. Ideally one chooses an SRF that is slightly above the target frequency to avoid ringing and other distortions in the filter network. The first (or broadband) configuration uses one or two 33 µH inductors and a mix of 100, 120, 150, and 180 µH inductors. The second (or tuned) configuration uses two or three Vishay Dale 180 µH inductors in series with two of the 33 µH inductors. Both methods yielded good suppression, but neither seems to work for all plasmas.

Table 5.2: Inductor characteristics used in the passive RF filters.

Manufacturer	Part Number	Value	Minimum SRF
JW Miller (Bourns)	8230-68-RC	100 µH	13 MHz
JW Miller (Bourns)	8230-70-RC	120 µH	12 MHz
JW Miller (Bourns)	8230-72-RC	150 µH	11 MHz
JW Miller (Bourns)	8230-56-RC	33 µH	24 MHz
Vishay Dale	IM02BH181K	180 µH	10 MHz

The capacitors used have fewer restrictions. While a larger capacitor smoothes out the RF signal more effectively, it also decreases the step response of any change in the electrode bias. Therefore, a judicious choice of capacitance is around 1000 pF. We used two Kemet 2200 pF, 100 V (Part #C420C222J1G5TA7200) capacitors in series to form the capacitive leg of the filtering network.

In Situ Monitoring via Oscilloscope

As mentioned in the previous section, a filter must suppress the RF signal (and its harmonics) used to generate the CCP plasma before the probe can record a meaningful sweep. While function generators can provide a useful indicator of the probe's frequency response, there is no substitute for observing the RF that the probe picks up from the plasma. The Agilent 6000 series oscilloscope can provide a graphical representation of the RF signal and allows the user to gain some insight into the maximum uncertainty that it could cause in the probe sweep. It also provides insight into probe and component aging as multiple sweeps are taken with a single probe.

5.3. Data Acquisition System

The data acquisition system consists of a Keithley 2400 sourcemeter, a custom control program written in Microsoft Visual Basic 6.0, an x86

computer running Microsoft Windows 2000 with an Agilent 82350B IEEE-488 (GPIB, HPIB, etc.) control board installed, and an Agilent 6000 series oscilloscope. The sourcemeter provides the driving signal to the probe tip during experiments, takes both voltage and current measurements, and facilitates plasma cleaning of the probe tip between experiments. The control program and associated hardware provide a method to automate data acquisition via the sourcemeter, record and organize data runs, and automate the process of cleaning the probe tip. The oscilloscope is used to monitor data runs in situ to ensure that the filters in the probe sufficiently attenuate the RF portion of the probe tip signal and other noise seen by the sourcemeter so as to assure consistent measurements and minimize error.

Sourcemeter

The Keithley 2400 sourcemeter is a DC voltage and current source, DC voltage and current measuring device, and can also measure resistance. The experiments make use of all of its capabilities except resistance measurements. The sourcemeter scans through a list of voltages provided by the control system, takes measurements at each voltage after a specified delay, and reports the collected current measurements back to the computer via the control system for storage and processing.

Control Program and Hardware

The control program (or application), written in Microsoft Visual Basic 6.0, combines three major functions: data storage and organization, probe cleaning, and sweep control (or data acquisition). Figure 5.11 shows an overview of the data acquisition application. Each of the forms comprising the application concentrates on one task. The hardware interface is based on the GPIB (IEEE-488) protocol and uses the Agilent 82350B card, the HP SICL32 dynamic link library, and the Visual Basic sicl32.bas module to translate the control commands provided by the program to the Keithley 2400 sourcemeter.

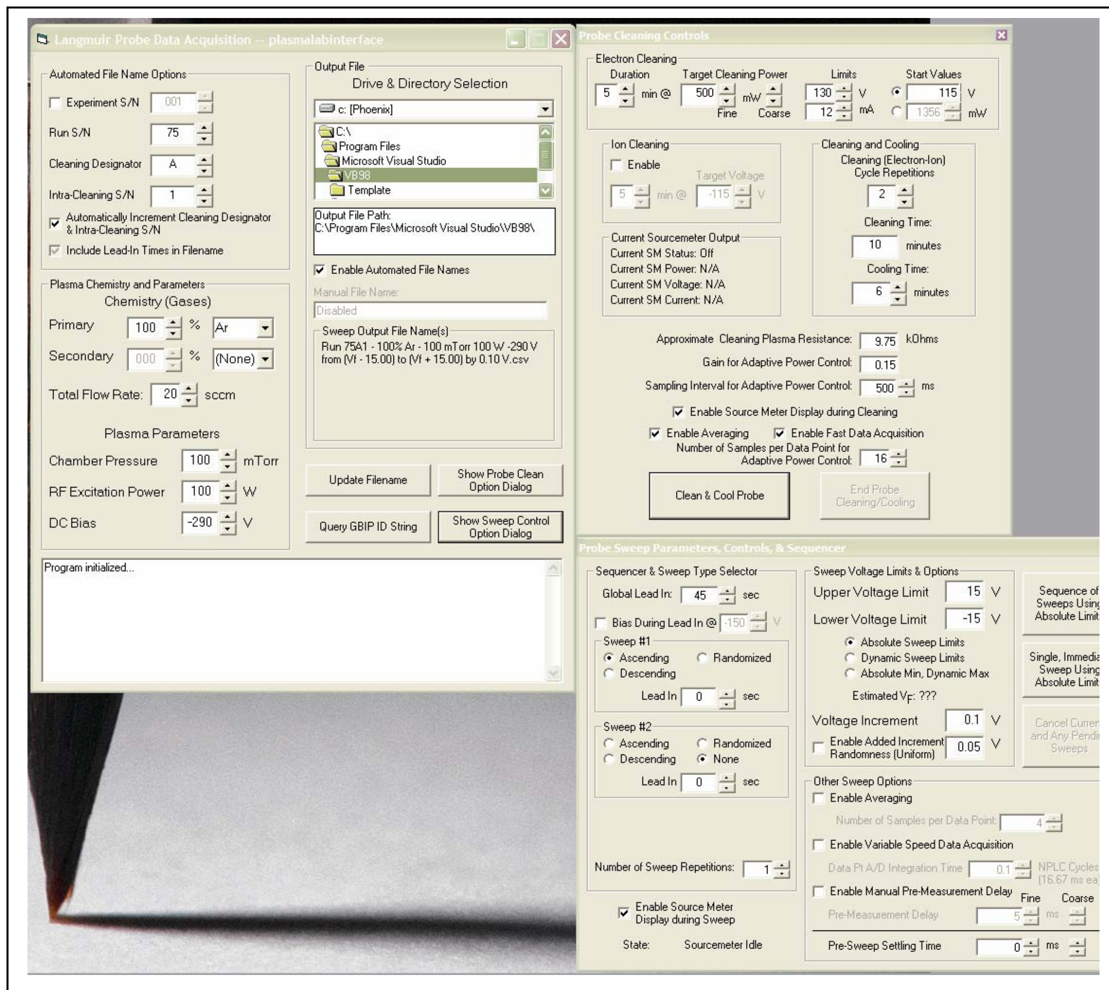

Figure 5.11: Overview screenshot of data acquisition application.

Figure 5.12: Screenshot of the data file organization form in the data acquisition application.

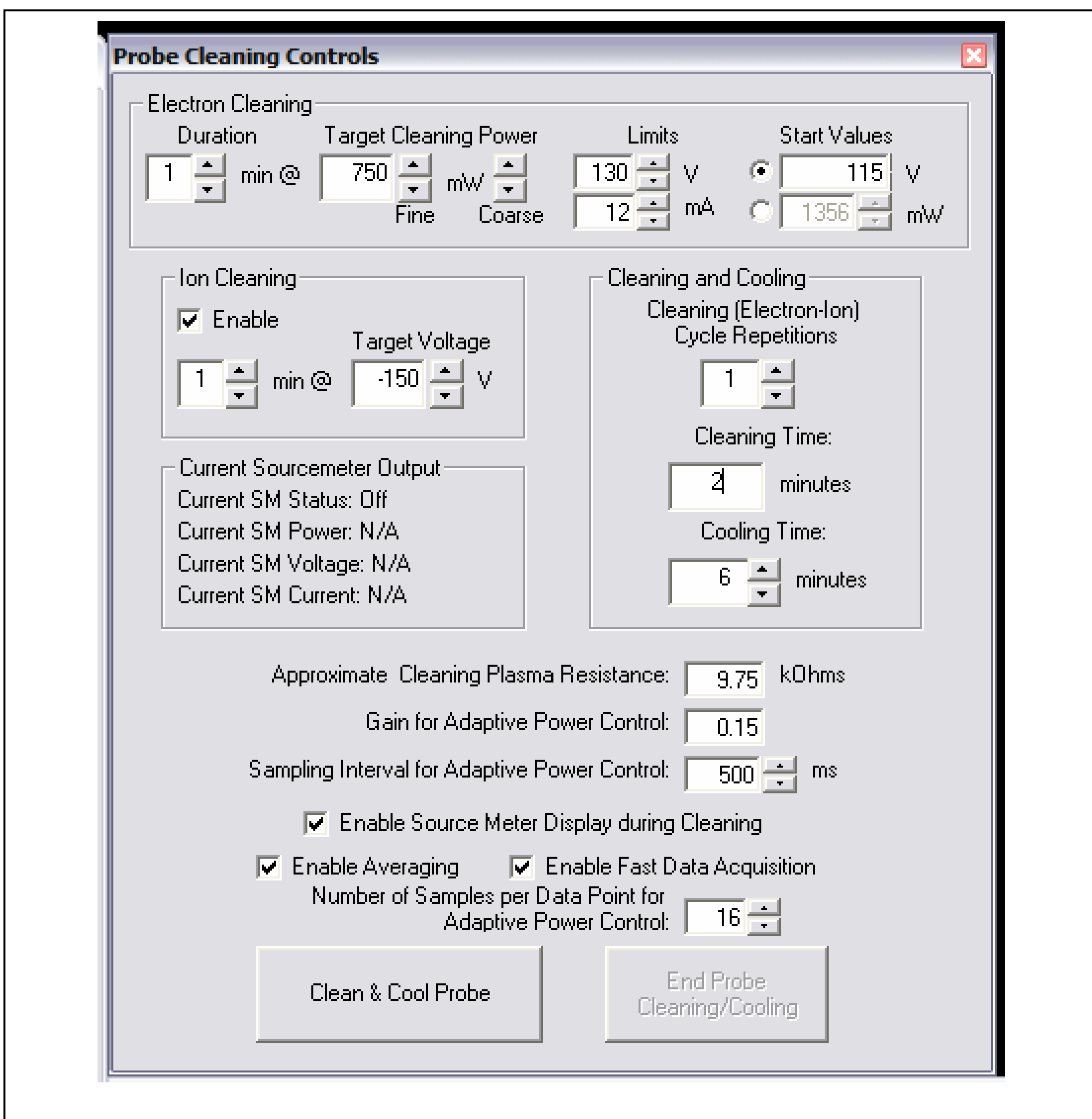

Figure 5.13: Screenshot of the probe cleaning form.

Because the number of I-V curves required for a single experiment (not to mention the countless preliminary tests and variations) inevitably requires some sort of indexing method, the first form (See Figure 5.12) allows the user to select the output file path, generates filenames based on a serial number system and experimental conditions. Further, it logs the experimental conditions to a log file and passes the filenames to the data collection form that records the collected I-V pairs. Further details of the indexing method, including details of what serial number codes mean can be found in Appendix C. For the purposes of elucidating the order of experimental curves, however, it is useful to point out that the first number in the filename is the run serial number that is usually associated with a single set of experimental conditions that vary one parameter such as pressure, power, or composition of the plasma.

The second form (See Figure 5.13) controls the probe cleaning cycle. Although Section 5.5 describes individual cleaning cycles in detail and explains the reasoning behind individual parts of those cycles in greater detail, the purpose of this form is to give the user flexibility in cleaning probes. To this end, there are two frames that correspond to electron and ion cleaning. A third frame "Cleaning and Cooling" allows the user to cycle repeat the electron-ion bombardment cycles as well as to pick a minimum cooling time that will allow the probe to re-equilibrate to approximately

room temperature after being subjected to electron and/or ion bombardment. The user can also select parameters for adaptive power control during the electron and ion bombardment. These parameters place limits on the maximum current and voltage and determine the gain so that charge carriers can bombard the tip with sufficient energy to knock off any impurities, while preventing a current or voltage overload that could (and has in the past) melted the probe tip during cleaning. Finally a frame is provided to allow the user to examine the current state of the sourcemeter in the event that cleaning does not appear to be working or if there are other anomalous conditions.

The third form (See Figure 5.14.) orchestrates the number and type of voltage sweeps that determine the characteristic I-V curve, records the values measured by the probe, and allows the user to pick individual the parameters of the voltage sweeps. Specifically, because the time in the plasma, the response time of individual probes, the direction of the sweep, and knowledge of the floating potential all influence the quality and usability of the probe sweep, the form needed to have a user-friendly method to control each of them. Further, repeatability is a constant concern in any scientific endeavor and even more so with plasma research, so options that take data multiple times in different ways allowed us to

further examine the effects of probe tip cleanliness and what effect it had on critical parameters and the shape of the I-V curve.

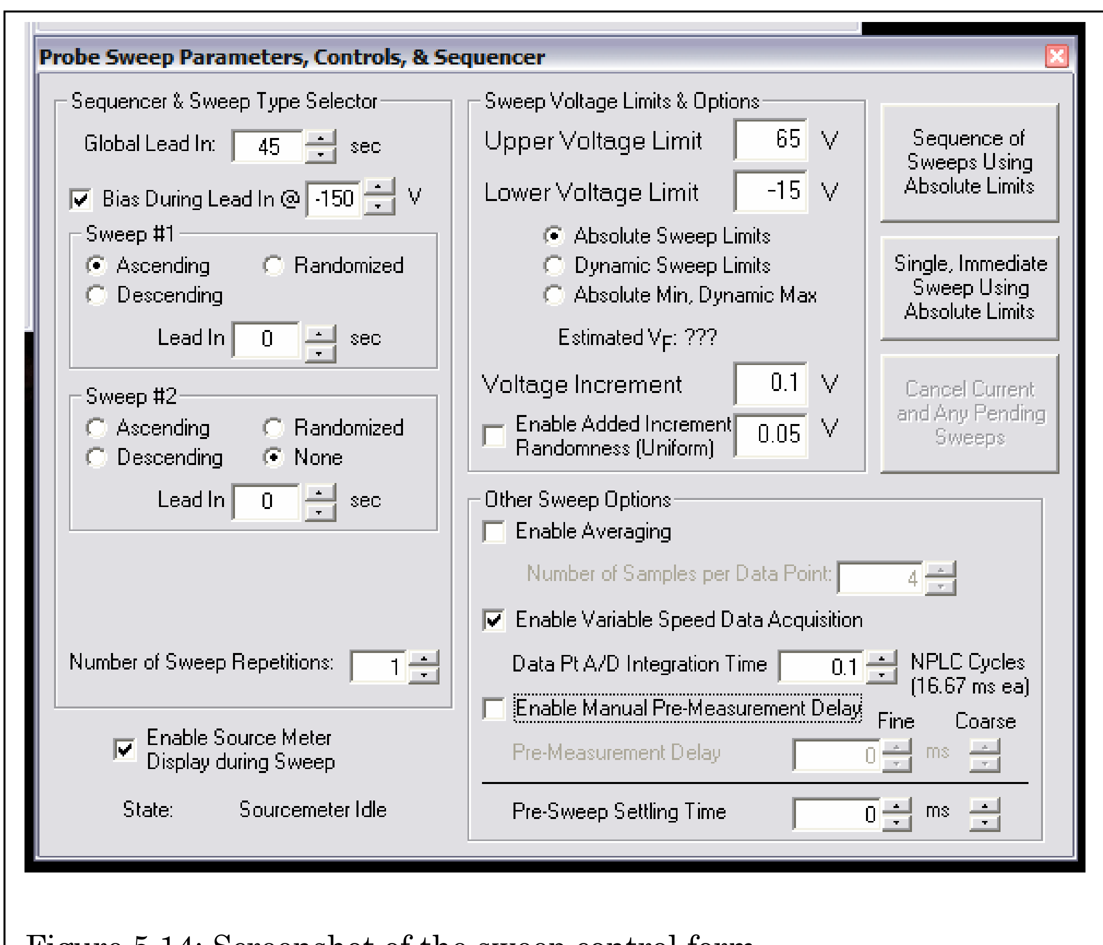

Figure 5.14: Screenshot of the sweep control form.

5.4. Data Analysis

Acquiring a usable I-V curve from the plasma is only the first step to understanding the plasma parameters, their trends, and the underlying physical phenomena. Initially, the collected data was processed using Microsoft Excel templates, but as the analysis of the data became more complicated and required a more automated, transparent, and customizable analysis, a series of MathCAD worksheets were developed. An example of each of the worksheets can be found in Appendix B. The worksheets accomplish five tasks: 1) post-process the data throughout the analysis to eliminate noise; 2) find an accurate V_p and V_f; 3) find kT_e and N_e by either calculating them directly from an approximate EEDF or by using the Log-Slope, SmartProbe, and SmartProbe with Laframboise correction methods; 4) display the various stages of analysis graphically so that they can be examined for unusual behavior (e.g., negative ions, multiple boundary layers in the plasma, excessive probe contamination, etc.); and 5) provide a method to easily export the values of kT_e, N_e, and any of the stages of analysis back into Excel so summary charts can be created.

The worksheets are separated into two categories: analyses that assume Maxwellian EEDFs, and those that do not. This progression

reflects the realities of the plasmas studied and the more important and less important factors affecting the resulting kT_e and N_e values.

Both worksheet templates use either smoothing or filtering to reduce the noise of the I-V characteristic. The first attempt at smoothing used localized smoothing with a Gaussian kernel. This smoothing technique was adequate for He and N_2, but did not work well for the BCl_3 and BCl_3/N_2 plasmas. The reason for this was that the BCl_3 and BCl_3/N_2 plasmas have 1) finer detail that a Gaussian smooth would smear out and 2) have surprisingly high noise so several iterations were required. Since the I-V characteristic was non-linear and not easily described in the case of an electronegative plasma, the LOESS filtering/curve fitting method as implemented by MathCAD was used [46, 47]. LOESS takes small sections of the curve and fits a low degree polynomial to those sections. In the MathCAD implementation, the polynomial is second order. This allows one to examine the effects of varying the length of the section to see coarser and finer features, corresponding to the electron distribution and the distribution of possible negative ions or charged metastable species while eliminating the relevant bandwidth of noise.

5.5. Experimental Protocol

While the experimental setup and protocol for each chemistry investigated was slightly different, a set of guiding principles directs all the experimental protocols. First, one must select the proper probe design. Second, based on each discharge's unique characteristics, one must determine the vertical placement of the probe within the chamber that will capture the region of interest. Third, the probe must be cleaned. And finally, several timing parameters must be selected to ensure that the sweep is a valid representation of what actually occurs in the plasma.

Determination of plasma region of interest and correct probe height

Because (at least) two sheaths form in an RF plasma, one at the powered electrode and one at the grounded electrode, and since a Langmuir probe obtains information about a plasma locally, interference from these sheaths and their presheath regions must be avoided. To further complicate things, the sheaths' heights change based on the difference in mass between the positive and negative charge carriers and the other layers in the plasma often vary based on the electron density. Consequently, each chemistry and pressure potentially requires adjustment of the probe height within the chamber.

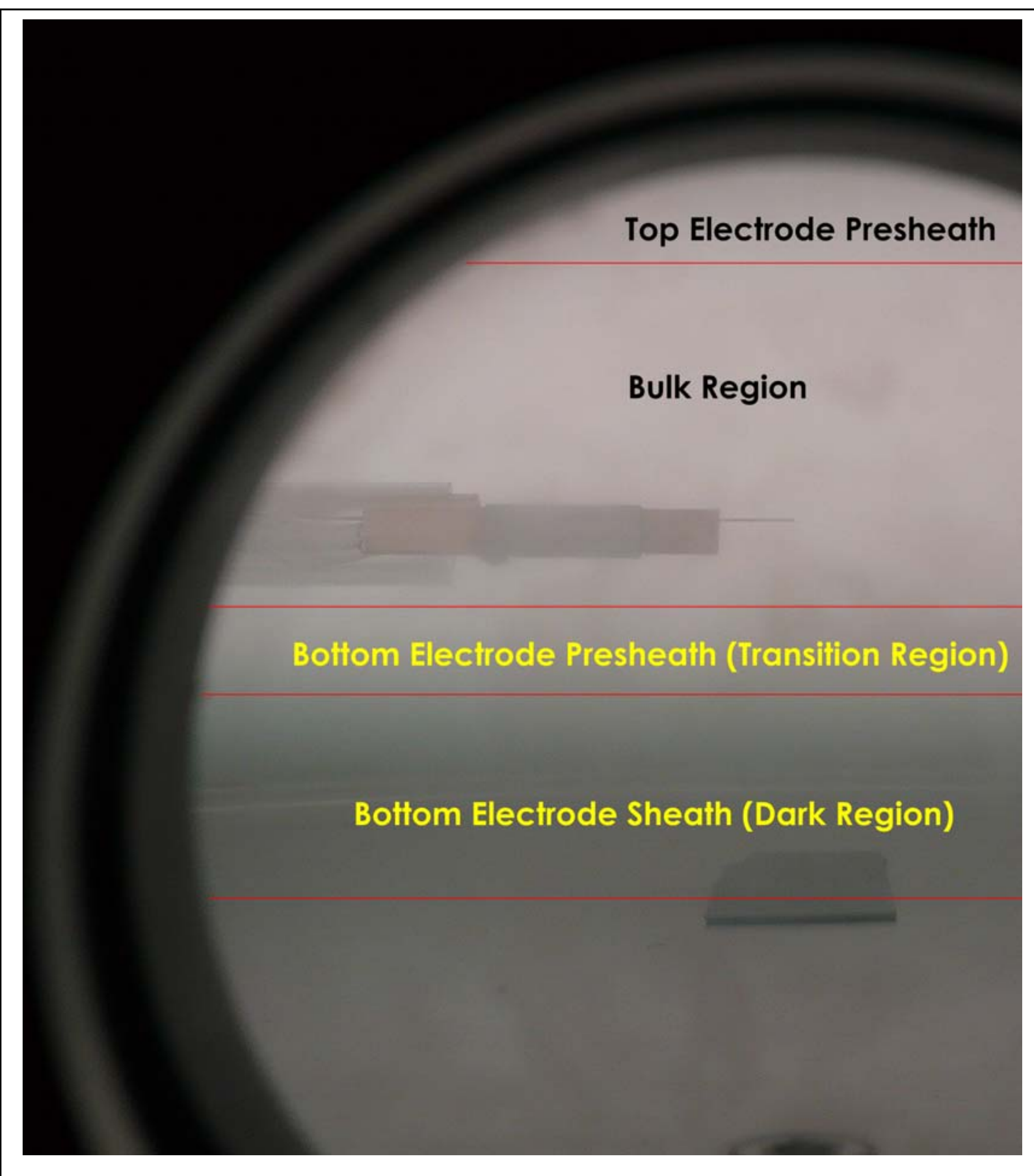

Figure 5.15: Labeled photograph of a probe *in situ* demonstrating the visual guides used to determine accurate vertical positioning.

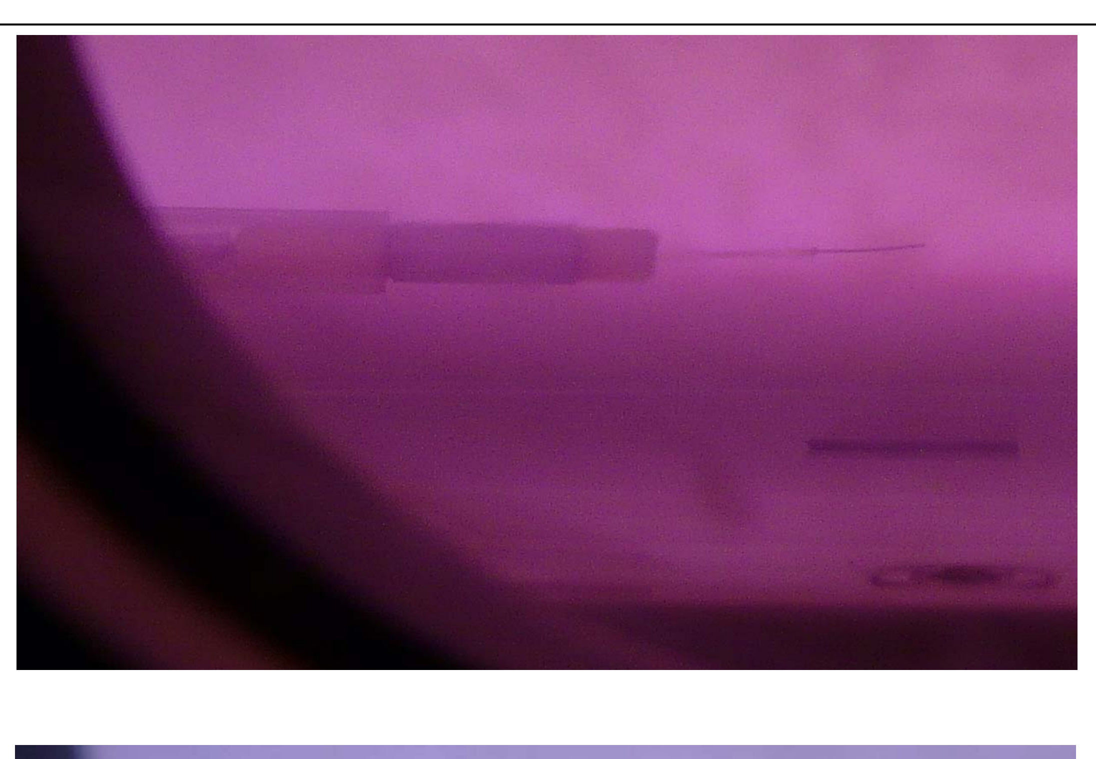

Figure 5.16: Photographs of a probe positioned to measure the presheath (Top, 100% N_2, 15 mTorr, 50 W) and the bottom of the bulk of the plasma (Bottom, He plasma, 50 mTorr, 100 W).

For calibration, the main region of interest is the bulk of the plasma since it is well mixed and large enough to provide uniform plasma characteristics several (5–20 depending on the plasma) Debye lengths above and below the probe. However, for plasmas that include N_2 and BCl_3 it is also worthwhile to examine the presheath region since this is the region that produces most of the ions that directly influence etching and if there are vertically varying effects one would expect significant variations in the EEDF and consequently kT_e and N_e in these regions (See Figure 5.16).

Even for cleaning the probe, the proper height is important. Since the sheath height is larger in a He plasma than in a BCl_3 or N_2 plasma, one can adjust the probe to be in the bulk region for the target plasma and find that the probe is in the sheath for a He cleaning plasma, rendering the cleaning cycle useless.

Cleaning

In-situ cleaning of the probe consists of electron bombardment and optionally ion bombardment. If ion bombardment is used, then the cycle can be repeated as many times as needed. The cleaning is then followed by a cooling down time. During electron bombardment, the probe is biased to a highly positive voltage with respect to the plasma. The result is that

the electrons in plasma are strongly drawn to the probe and the resulting collisions not only transfer charge but also momentum and create heat. Any impurities that have formed a surface layer on the probe are either knocked off or evaporate off of the tip. The probe glows a bright orange color during this phase of the cleaning cycle. Electrons have a very small mass, however, and so the primary mode of cleaning is thermal. Ion cleaning complements this action. By biasing the probe strongly negative, the opposite effect occurs. The positive ions are strongly attracted to the probe, and though the probe does not glow orange-hot during this phase, the momentum transfer of the ions sputters away any remaining contaminants.

The probe tip was typically cleaned in a 50 mTorr, 100 W He plasma. If a He plasma was to be investigated, then an electron bombardment at 750 mW (around 100–130 V) would suffice to clean the probe. With N_2 and BCl_3, however, electron bombardment (as before) and ion bombardment (at –150 V) cycles were used because of the contaminant films that readily formed on the probe surface. Typically each electron and ion bombardment phase lasted two minutes as did the cool down after the clean was finished.

Probe Sweep and Plasma Settling Timing Parameters

The probe sweep duration and data point settling time were chosen as trade-off parameters. The A/D integration time on the sourcemeter was chosen as 0.1 PTAD (a unit determined by the frequency of the AC power source, in the US 1/60 Hz) or 1.667 ms. The settling time was chosen as 1 ms, and because the sourcemeter has as built in trigger and settling time of 1.5 ms, the data points were collected approximately every 4.167 ms or at 240 Hz. With ~1150 samples per data run each sweep lasted ~4.8 seconds, thus avoiding contamination and ensured that there were enough cycles of the plasma frequency to allow the plasma to settle between data points.

However, there was also a need to allow the plasma to settle after striking before sweeps were taken to allow the matching network and the bulk of the plasma to come to equilibrium. This took approximately 25 seconds and was controlled using the global lead in option of the data acquisition application.

Chapter 6. Experimental Chemistries

6.1. Helium Calibration

As previously discussed, Langmuir probes were first used in DC discharges and then in highly ionized plasmas. Because the targets of this study are weakly ionized, RF plasmas, the first step to ensuring that our probe works and that we have a valid data acquisition and analysis system is to characterize a well known or at least well behaved chemistry. Pure helium fits this profile well. Helium is inert and monatomic, produces light ions, and ionizes at a high energy of 24.587 eV. This suggests that the only charged species that would be present in the bulk plasma would be singly ionized He ions and electrons and consequently the other interactions (such as collisions) would result in a well defined Maxwellian electron energy distribution. Because R. Alapati used 125 mTorr and 175 W as plasma parameters in his study of SF_6/He [2], these initial calibration experiments are centered on this pressure and power.

6.2. Variation of kT_e and N_e, and the Evolution of the EEDF in He

Pressure Variation

Gas kinetics predicts that as pressure increases, the average energy per particle decreases if the same amount of power applied to a system

because the number of particles per unit volume increases proportionally to the pressure. With a gas at room pressure and temperature, there is often an abundant supply of external thermal energy to keep the entire system at a single temperature and consequently varying the pressure on a small scale does not greatly alter the average energy of species. For a simple plasma, this relationship between increased pressure and individual electron energy decreasing is magnified because the power that is injected into the system maintains the plasma state by moving electrons and that source of energy is finite and controllable. If the pressure increases, the power then must be distributed over a larger number of electrons and unlike a room temperature gas, there is not enough thermal energy in a plasma to compensate for this effect.

The initial pressure calibrations maintained a fixed power of 175 W and varied the pressure from 20 mTorr to 150 mTorr. As expected, the average electron energy ($<\varepsilon>$), and consequently the equivalent electron temperature (kT_e) decreased with increasing pressure in an inverse exponential curve while N_e increased somewhat linearly (See Figure 6.17).

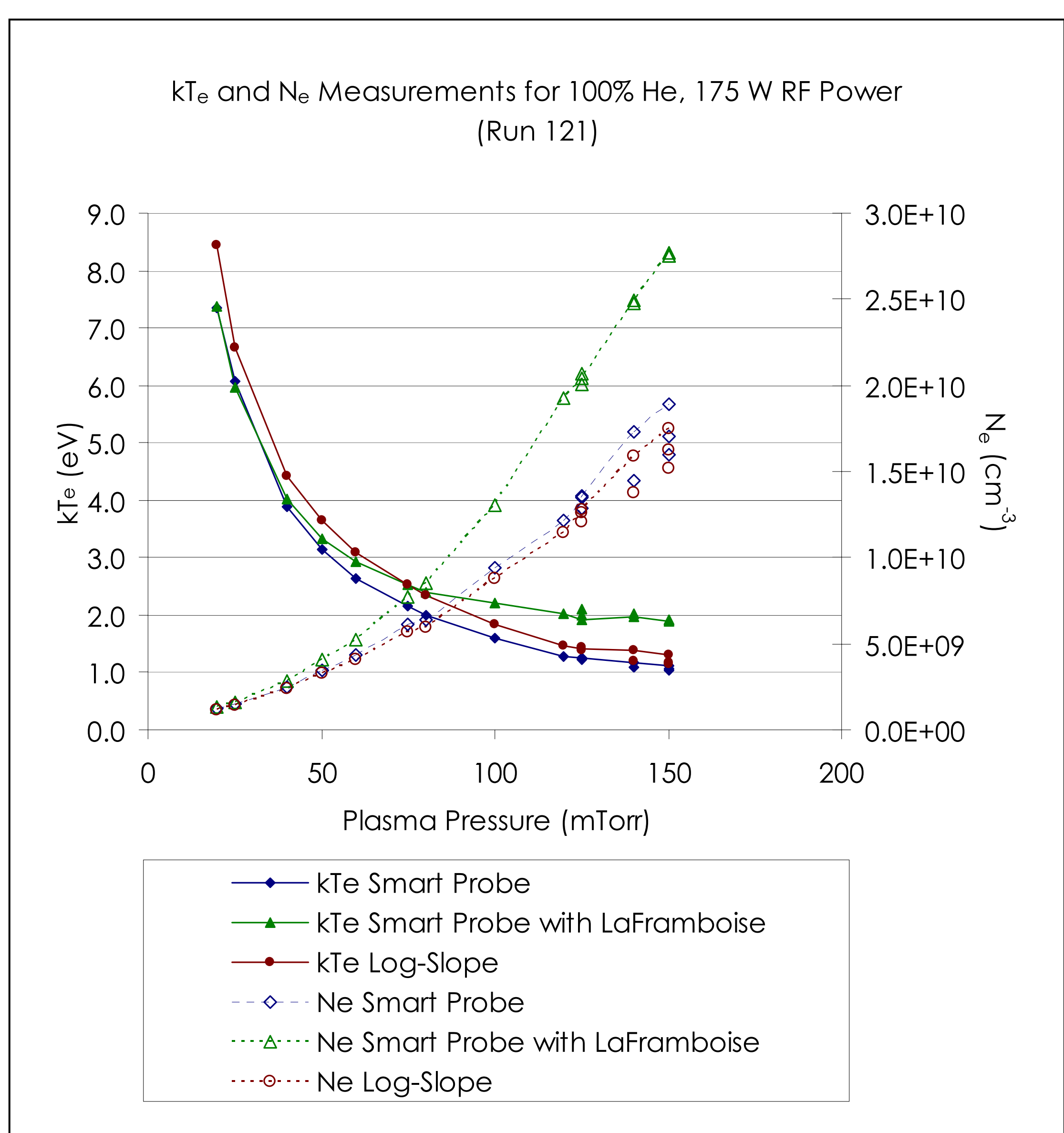

Figure 6.17: kT_e and N_e measurements 100% He, 175 W RF Power plasma with pressure ranging from 20 to 150 mTorr (Run 121).

Because the Log-Slope, SmartProbe, and the LaFramboise methods are used to calculate kT_e and N_e in Figure 6.17, a Maxwellian EEDF is inherently assumed. While this is not often the case for most plasmas, the assumption does hold for the lower pressures (such as 40 mTorr) in this set of experiments as can be seen by the EEDF itself (Figure 6.18).

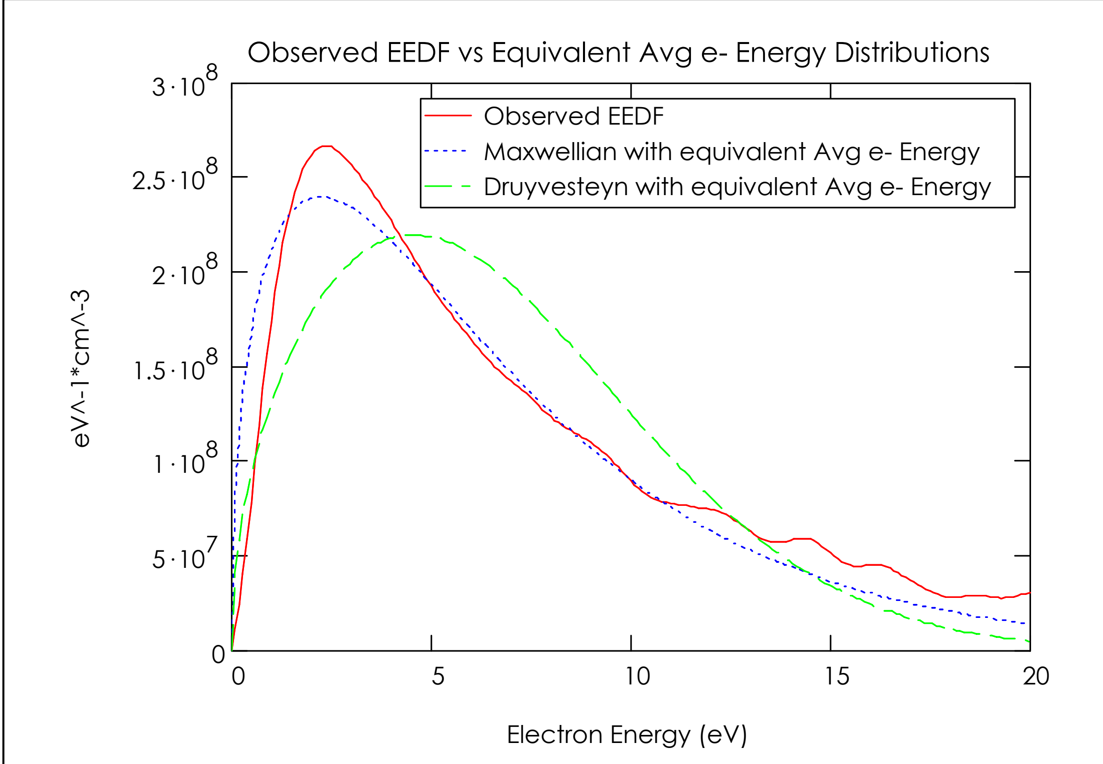

Figure 6.18: Comparison of an EEDF of a 100% He, 40 mTorr, 175 W plasma with a Maxwellian and Druyvesteyn distribution of equal average electron energy.

As the pressure increases to 125 mTorr, the distribution becomes more Druyvesteyn as can be seen by comparing Figure 6.18 to Figure 6.19 and observing the evolution of the EEDFs in Figure 6.20. At this point, the kT_e and N_e values found assuming a Maxwellian distribution are only useful as qualitative indicators; they no longer hold any true meaning quantitatively.

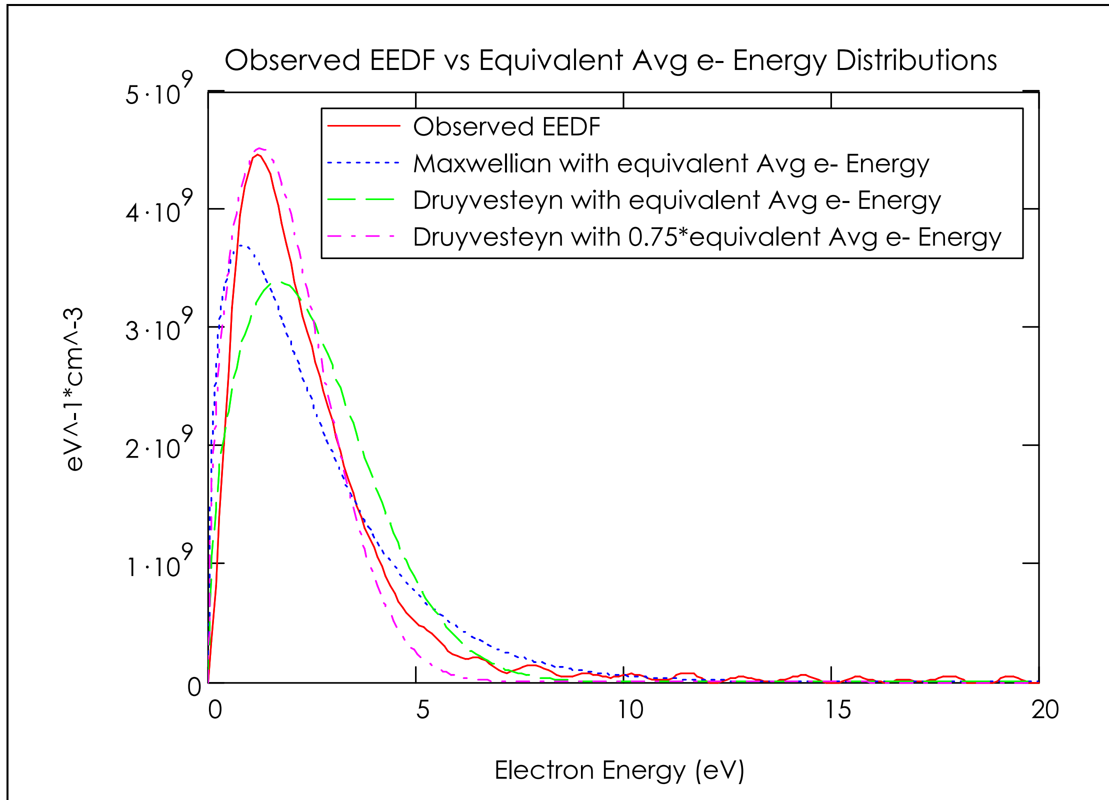

Figure 6.19: Comparison of an EEDF of a 100% He, 125 mTorr, 175 W plasma with a Maxwellian and Druyvesteyn distribution of equal average electron energy, as well as a Druyvesteyn distribution with ¾ the average electron energy found from the observed EEDF.

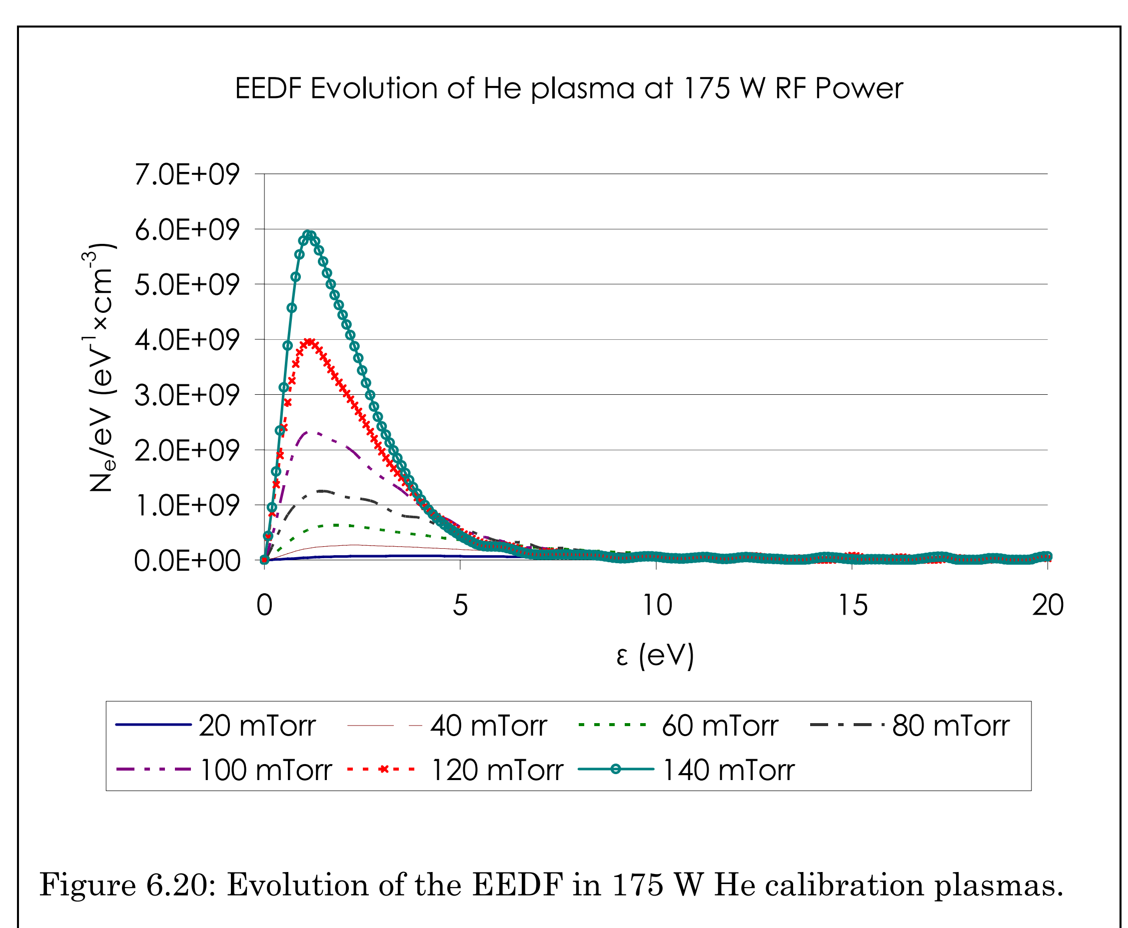

Figure 6.20: Evolution of the EEDF in 175 W He calibration plasmas.

Given this change in distribution shape, actually calculating $<\varepsilon>$ from the EEDF gives a more telling measure of the change in average electron energy and density. Further, it became clear that most of the experimental EEDFs would be neither purely Maxwellian nor Druyvesteyn, and in order to fit the curves to one or the other would require additional fitting parameters such as modifying $<\varepsilon>$. (See Figure 6.19.) This suggested that even an estimated EEDF would provide more insight into the qualities of free electrons (and a window into negative ion densities that might be encountered in electronegative processing plasmas) than methods that assumed a particular distribution. With this in mind, a MathCAD sheet was developed to visualize and analyze an estimate of the EEDF of various plasmas. Using that technique, a more accurate plot emerged. (See Figure 6.21.)

Surprisingly, the kT_e and N_e values and trends cluster together fairly well independent of the method used to calculate them. This outcome both reinforced our belief that the probe behaved as expected and shows that these methods are fairly robust in well behaved gases—despite the evolution of the EEDF from a Maxwellian distribution toward a Druyvesteyn distribution, the trends do not deviate from one another significantly using the three different methods.

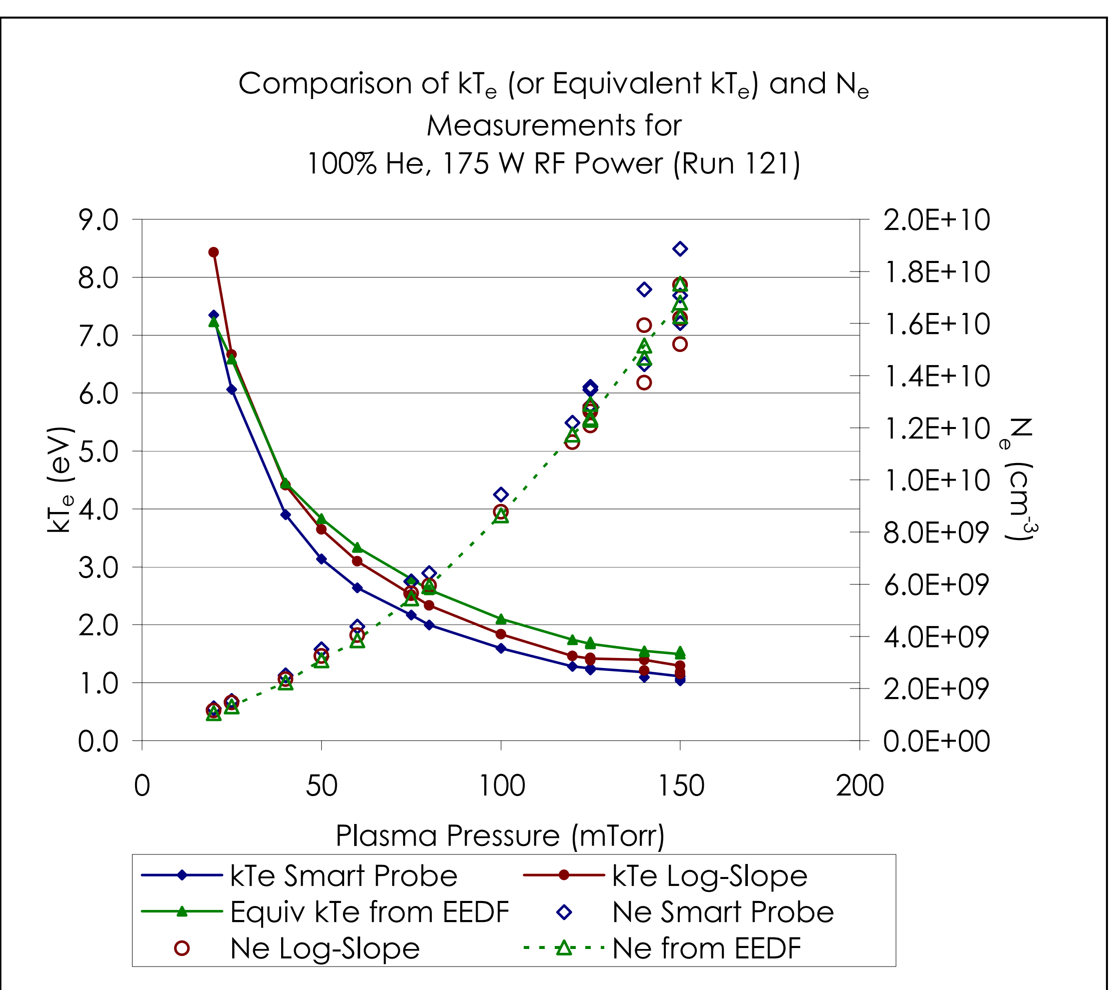

Figure 6.21: Comparison of kT_e and N_e calculations based on Log-Slope, SmartProbe, and EEDF measurements in 175 W He calibration plasmas.

Power Variation

Along with pressure, power is a clear external input to plasmas. By maintaining a constant pressure and varying power, the researcher forces the plasma to distribute varying amounts of energy on a constant number of particles. This effect is well known, and if the type of energy distribution remains constant, the variations will follow a well-defined pattern. The higher values of kT_e and N_e found via the EEDF method in the pressure variation experiment and the fact that the distribution is more Druyvesteyn at higher pressures warranted that we include it to determine more accurate values for kT_e and N_e, and to compare and contrast it with methods that would assume a Maxwellian distribution. Again, since Alapati used 125 mTorr and 175 W in his studies of SF_6/He mixtures, this experiment used 125 mTorr. The results of this experiment are summarized in Figure 6.22.

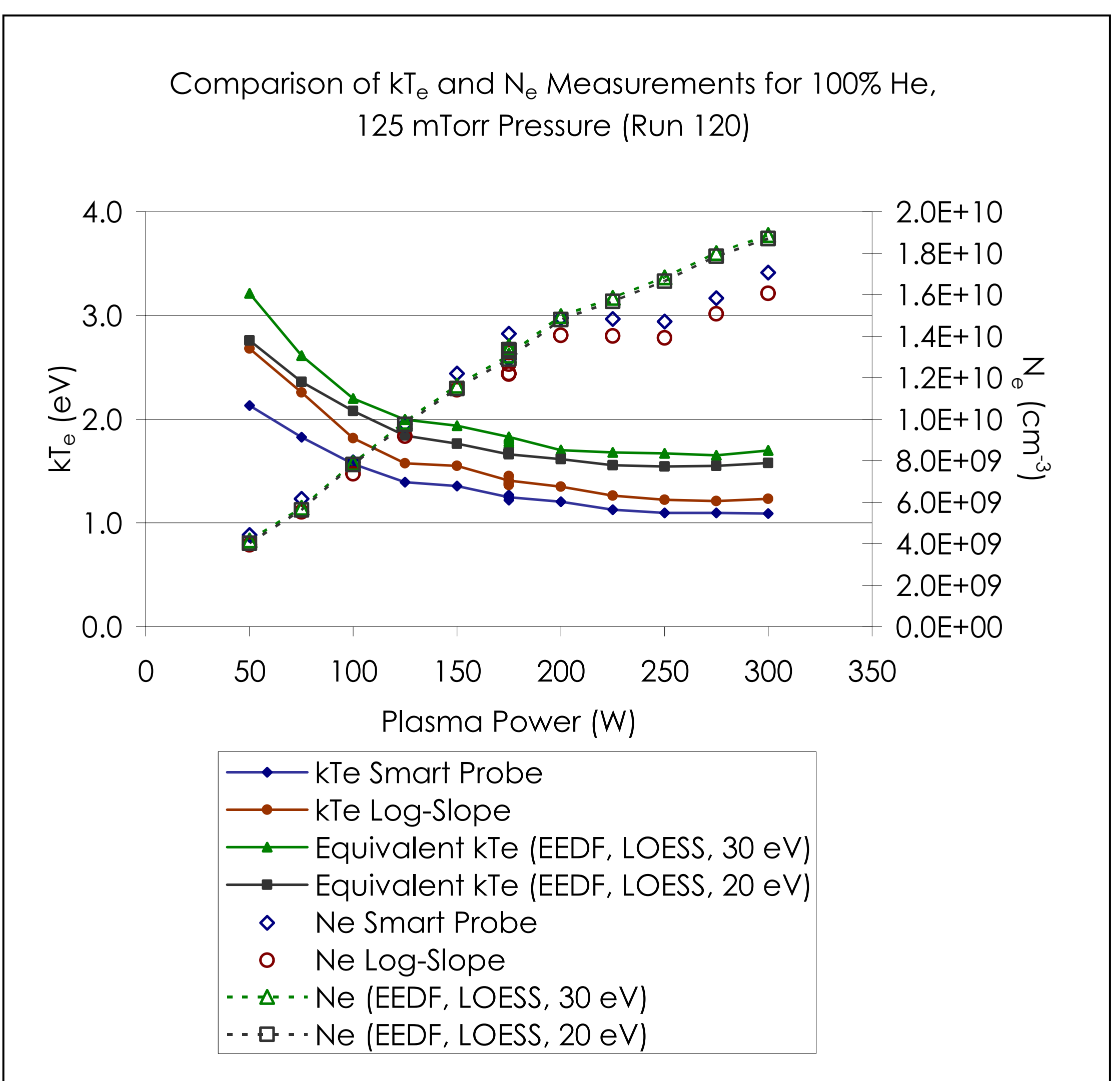

Figure 6.22: Comparison of the kT$_e$ and N$_e$ values obtained using various techniques in 125 mTorr He calibration plasmas.

As in the case of the pressure variation, kT_e decreased along a power curve with increasing power because an increase in dissociation resulted in far more electrons over which the increase in power had to be distributed. Unlike the case of pressure variation, however, N_e exhibited two separate linear regions (50–200 W, and 200–300 W) if calculated via the EEDF method, and an anomalous region between 200–250 W if calculated using the Log-Slope or SmartProbe methods. Surprisingly, this did not seem to correlate with any sharp change in the overall shape of the EEDF when compared to a Druyvesteyn with equivalent $<\varepsilon>$.

In Figure 6.22 there are two sets of equivalent kT_e and N_e values derived from the EEDF. They differ in how far out in energy we chose to calculate the EEDF. Remember that the farther out the EEDF is calculated the larger the $\sqrt{\varepsilon}$ factor that is multiplied by the second derivative of the I-V characteristic, and the greater the negative offset created by the positive ion saturation current. As $\sqrt{\varepsilon}$ increases, the noise that is inherent in the second derivative of the probe sweep is magnified, artificially inflating N_e. If the positive ion saturation current is linear or constant, the double differentiation removes its influence. If it is not, however, the differentiation could have unexpected side effects. By examining different ranges for the EEDF, we can hope to capture the

necessary detail to give accurate results without introducing too much noise at higher electron energies. In the case of helium, it is clear that even if the EEDF is extended out an additional 10 eV, neither kT_e trends nor N_e trends and values change significantly. Both are included to give the reader an idea of the possible error that could be introduced by extending the range of the EEDF out past where it is warranted in a well behaved gas. A similar example will be used when a more complicated plasma is discussed.

6.3. N_2 Calibration

Nitrogen was the second gas chosen to calibrate the Langmuir Probe. Like He, N_2 is relatively inert and electropositve, but it differs in that it is a molecular gas. This means that not only will ionizations and inelastic collisions affect the distribution of electrons, but the molecular bonds will also play a role. Nitrogen also presents an interesting test case because it is known that as pressure increases the EEDF changes shape and a "hole" develops at the resonant energy of the bond vibrational energy [13, 15]. With this in mind, and because J. Sia and K. Nordheden observed etch rate enhancement with a BCl_3/N_2 mixture at 15 mTorr and 50 W power [4, 6], N_2 calibration was centered on these values.

While taking data in N_2 (and He), the probe was adjusted so that it was at its highest position possible to ensure that the tip remained in the bulk region of the plasma throughout the runs and well above the driven electrode and its sheath. This is because N_2 (in addition to gaining a hole at higher pressure) exhibits anomalous sheath heating at low pressures in RF plasmas [13]. Turner describes the effect as a "push-pull" mechanism that the driving RF creates when it induces the sheath around the electrode to contract and expand. The time varying sheath alternately draws in and expels the electrons in the boundary layer between the bulk plasma and the sheath. The elastic and inelastic collisions these highly energetic electrons undergo with neutrals as they are driven back into the bulk plasma rapidly attenuate their energy and confine the unusual heating effects to a thin boundary layer at the edge of the bulk. The electrons that do not collide with the N_2 neutrals then heat the bulk of the plasma normally. It should be noted that if N_2 were an atomic gas with a high first ionization energy, the effect would not change the energy distribution of the bulk plasma. Because it can store energy in its bond in the form of vibration, however, the N_2 robs the electrons of a specific range of energies. Further, as pressure increases, the sheer quantity of targets increases and consequently the boundary layer where those energetic

electrons lose their energy becomes thinner, localizing the effect even more, creating a deeper hole in the EEDF.

6.4. Variation and Relevance of kT_e and N_e, and the Evolution of the EEDF in N_2

Pressure Variation

Unlike He, N_2 is known to not follow classical gas kinetics at higher pressures in plasmas. It is however, known to have a Maxwellian or Bi-Maxwellian distribution at lower pressures. To see the effects of pressure variation, the power was kept at 50 W, and the pressure initially varied from 10–75 mTorr. The electron temperature (or its equivalent) and N_e were calculated using direct EEDF analysis, the Log-Slope Method, the SmartProbe Method, and the SmartProbe method with a LaFramboise correction. Figure 6.23 summarizes the results with one major omission: kT_e calculated via the SmartProbe method with LaFramboise correction. These were omitted because excessive noise in the data at 50 W noticeably confused the automated LaFramboise correction and resulted in clearly erroneous values for kT_e.

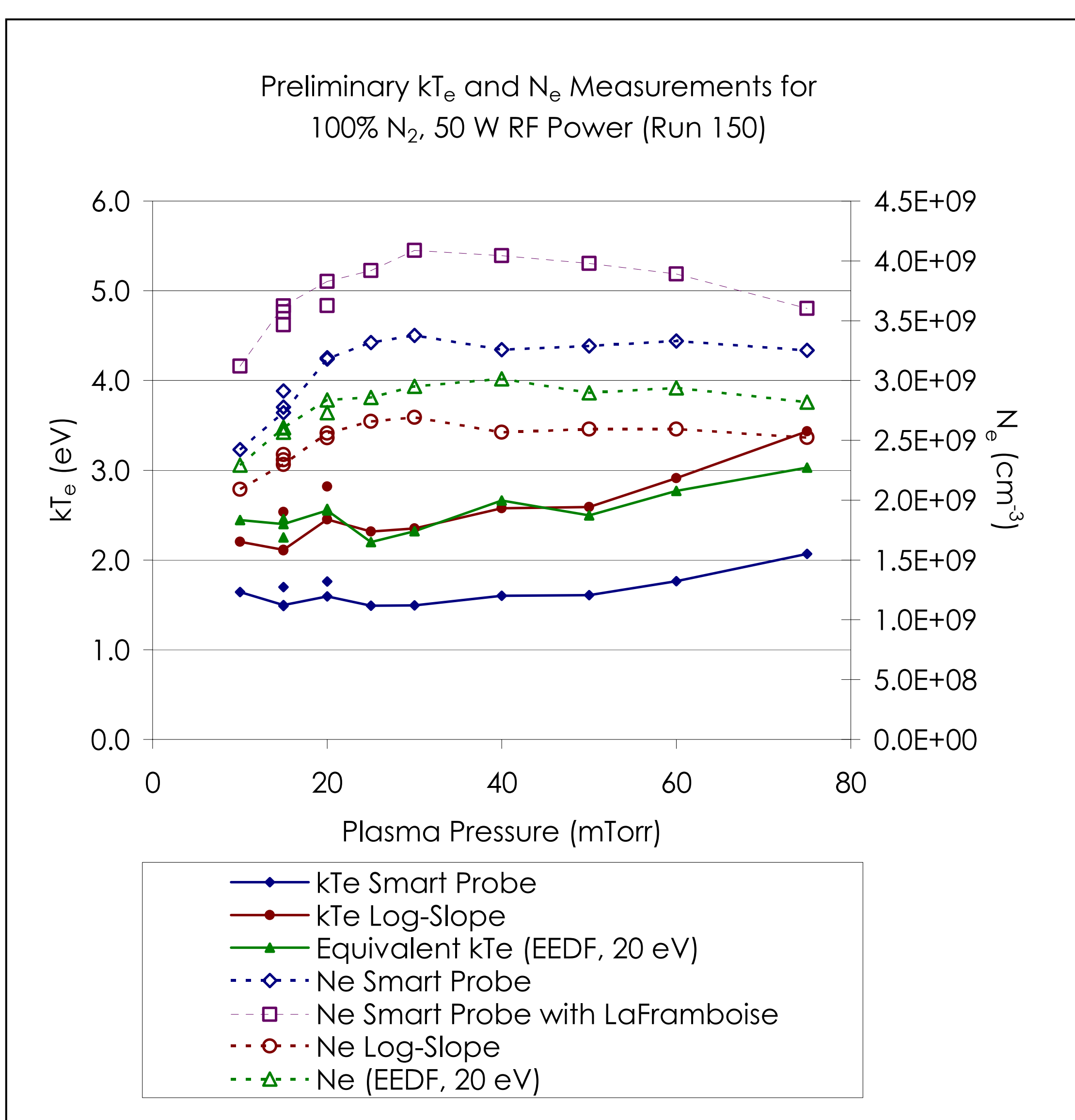

Figure 6.23: Comparison of the equivalent kT_e and N_e values obtained using various techniques (including LaFramboise correction) in 50 W N_2 calibration plasmas.

In Figure 6.23, kT_e or its equivalent stays fairly constant with pressure up to about 40 mTorr and then increases with pressure but only slightly. N_e increases up to 30 mTorr, and then saturates. Again, the exception to this is the SmartProbe method with LaFramboise correction which had problems discerning when the electron current saturated. The fact that kT_e and N_e have clear transitions encourages one to examine the evolution of the EEDFs directly.

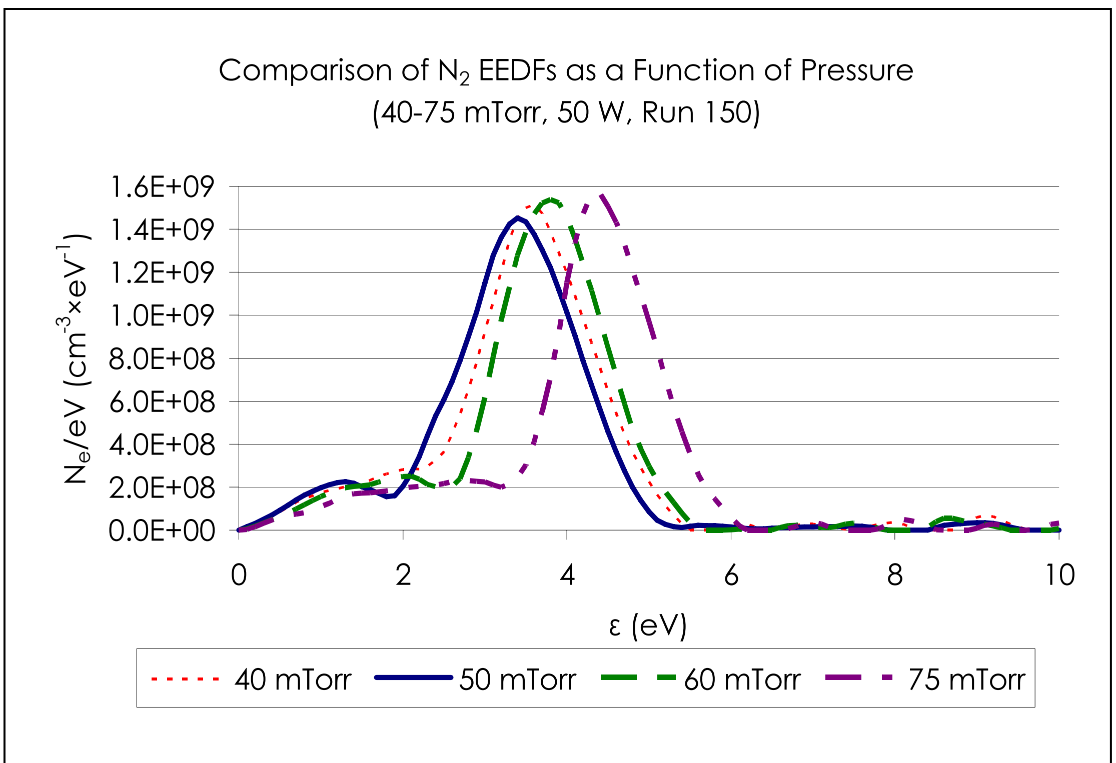

Figure 6.24: Comparison of the EEDFs of 40-75 mTorr N_2 calibration plasmas.

After examining the EEDFs, they fall into two categories: below ~40 mTorr and above 40 mTorr, with 40 mTorr being a transition point. Figure 6.25 shows that below 40 mTorr, the EEDF appears to have a fairly constant <ε>, and the area under the curve simply increases with increasing pressure. This indicates that up to 40 mTorr, as pressure increases, the dissociation rate continues to increase relative to the recombination and bond excitation rate increasing the electron density without a corresponding change in kT_e. Above 40 mTorr, there are enough N_2 molecules available that collisions result more readily in both direct

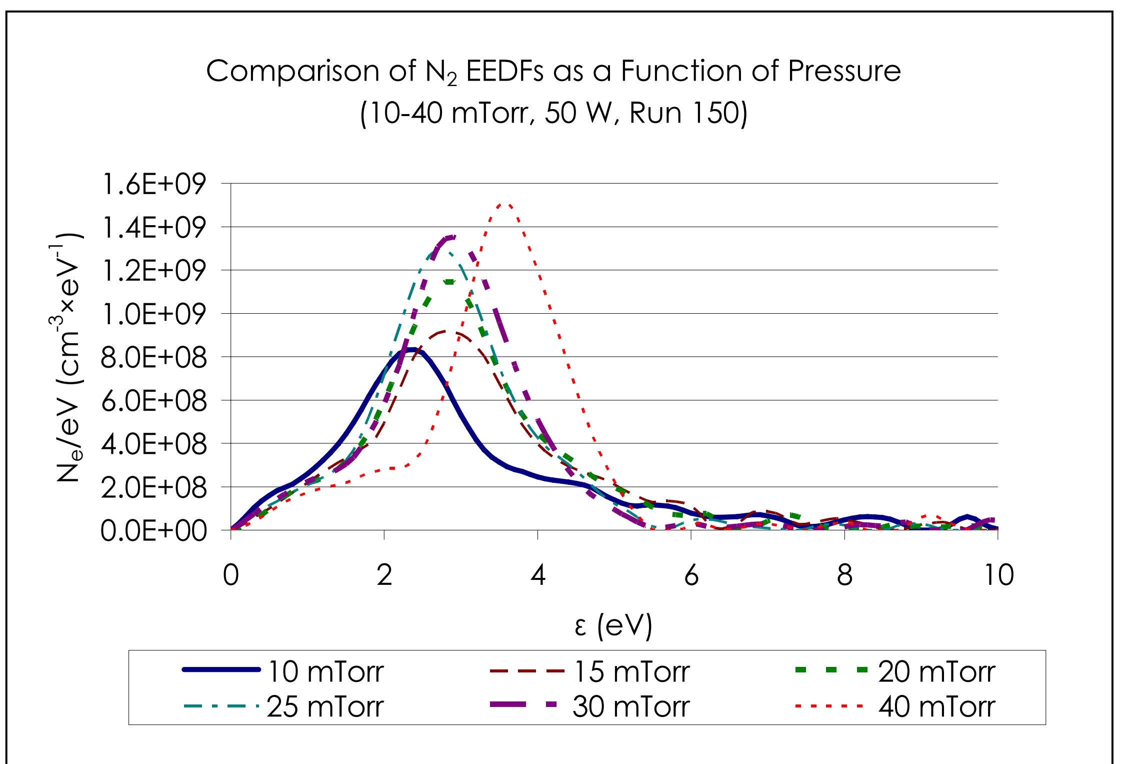

Figure 6.25: Comparison of the EEDFs of 10-40 mTorr N_2 calibration plasmas.

dissociation and vibrational bond excitation. The low energy electrons are very readily scavenged by collisions that result in bond vibration excitation, and this drives the number of free electrons down, which increases kT_e. Regardless of how one looks at the results, however, 40 mTorr clearly represents a change in the character of the EEDF. At this point, one begins to see a “hole” before the main peak of the electron distribution and a shift in the EEDF toward higher energies. (See Figure 6.24.) This trend continues with increasing pressures, and the hole remains. This hole corresponds to vibrational excitation of the N≡N bond and has been described in the literature as a marker of a well designed probe [13, 15], and while those papers show that it is often not very deep until higher powers and pressures, it is reassuring to see its beginnings. It is also worthwhile to note that 40 mTorr actually has a higher $\langle\varepsilon\rangle$ than 50 mTorr and less of a hole before the main electron peak making it a nice example of blending of the lower and higher pressure EEDFs.

Since the EEDF reflects intra-molecular dynamics in N_2, and clearly shows non-Maxwellian characteristics, one would be remiss in thinking that trends in kT_e and N_e explained all the electron dynamics in a molecular gas plasma. This is especially important since virtually all processing gases are even more complicated molecular gases than N_2, and might therefore exhibit more, not fewer intra-molecular effects.

Power Variation

For N_2 power variation calibration, the pressure was kept constant at 15 mTorr and the power varied from 25–300 W. Because the observed N_2 EEDF transitioned from a one type of distribution to another at 40 mTorr, it was unclear whether a similar transition would present itself somewhere in the power spectrum. Because of this, the only viable method was to examine the EEDFs directly and only then decide whether a summary chart of equivalent kT_e and N_e values would be worthwhile.

Figure 6.26 shows the evolution of the EEDFs with increasing power. In order not to oversmooth the EEDFs because any fine structures such as holes would be important in determining the EEDFs' character, the smoothing parameters were kept to a minimum. This obviously results in EEDFs with less smooth profiles. Still, it is clear that the shape of the distribution does not change with power at 15 mTorr and resembles a Druyvesteyn distribution. With this in mind, the Log-Slope and SmartProbe methods can be compared with an equivalent kT_e and N_e directly calculated from the EEDF just like in the He calibrations.

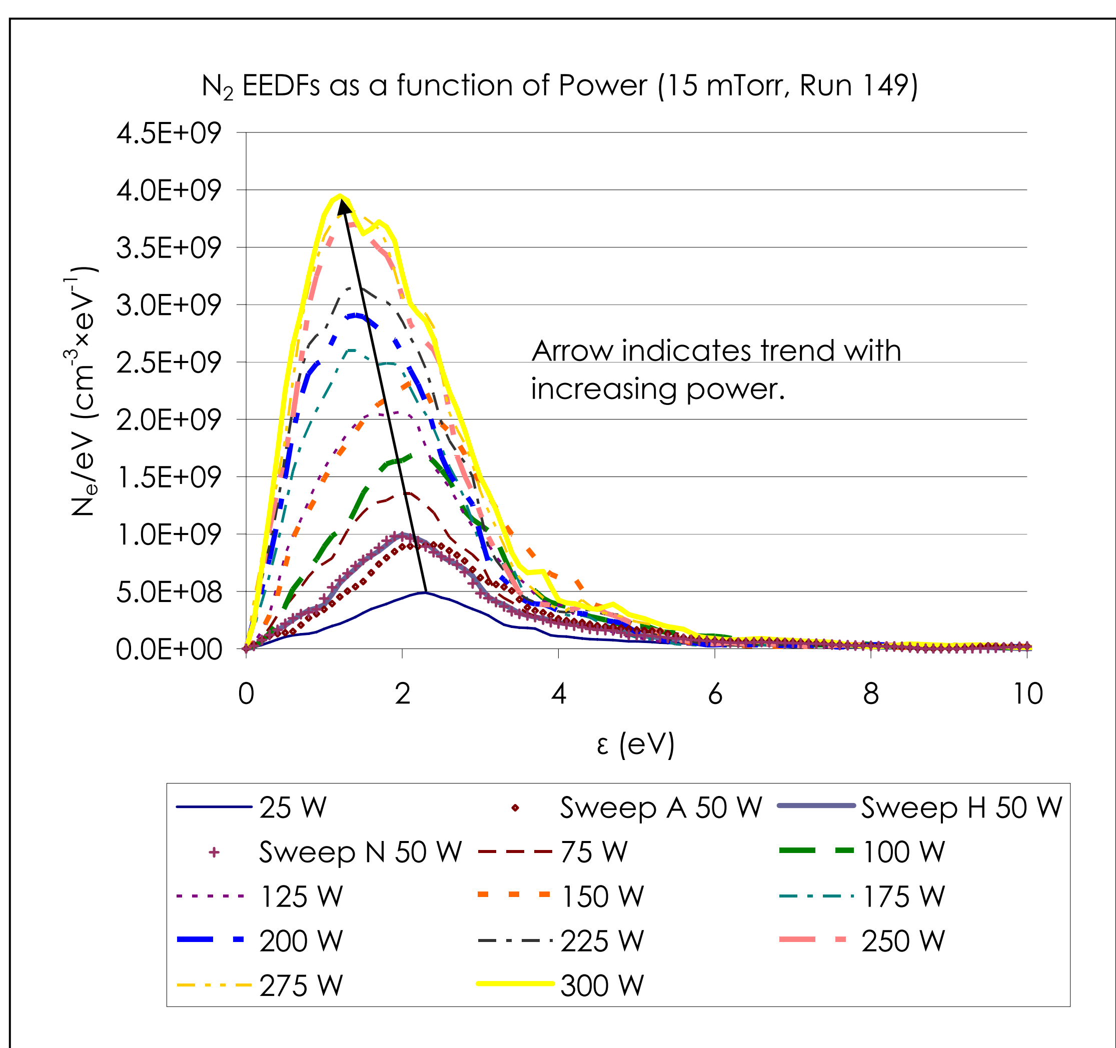

Figure 6.26: Comparison of EEDFs for 25-300 W N_2 calibration plasmas.

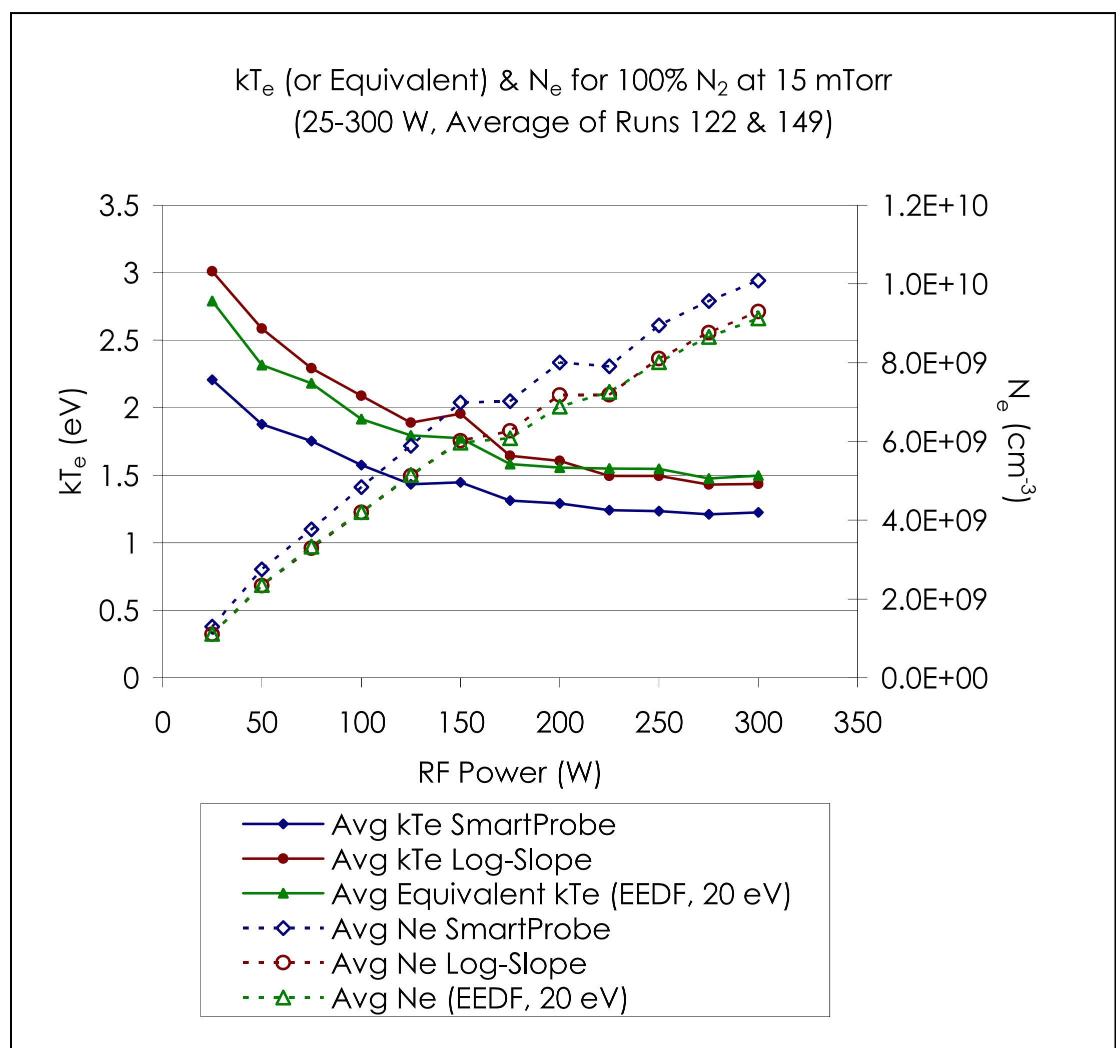

Figure 6.27: Comparison of the equivalent kT_e and N_e values obtained using various techniques in 15 mTorr N_2 calibration plasmas.

In Figure 6.27, kT_e and N_e evolve as gas kinetic theory predicts, with no hint of intra-molecular effects. Again, with increasing power, kT_e decreases on a power curve while N_e increases linearly because of increased dissociation. Figure 6.27 averages Runs 122 and 149 because while they both exhibit the power trend for kT_e and the linear trend for N_e, they vary in when they were taken and what gases were introduced into the chamber between runs. Run 122 was taken immediately after He calibrations, while run 149 was taken after the chamber was conditioned with N_2 for an extended period of time to alleviate any concerns that residual He would affect N_2 calibration.

6.5. BCl_3 Calibration & Investigation

BCl_3 is a common parent species in etching plasmas, particularly for III-V substrates because it provides the necessary Cl and Cl_2 species upon dissociation. BCl_3 is also intriguing because of its electronegativity. While He and N_2 both donate electrons and are quite stable as positive ions, electrons can attach to BCl_3, forming BCl_3^-, and to the active species Cl and Cl_2, forming Cl^- and Cl_2^- respectively. Both attachment to BCl_3 and Cl are even energetically favored (by 0.33 eV for $BCl_3 + e^- \rightarrow BCl_3^-$, and 1.132 eV for $Cl + e^- \rightarrow Cl^-$) so the species actually gain energy once the attachment occurs [21, 48, 49]. Again, because J. Sia's and K. Nordheden's

work in BCl_3/N_2 focused on 15 mTorr and 50 W, these experiments are centered on that pressure and power [4, 6].

6.6. Variation in N_e and kT_e, as well as Evolution of the EEDF in BCl_3

Pressure Variation

G. Franz has shown that the electronegative nature of BCl_3 only presents itself above pressures of 25 mTorr in CCPs and that it behaves much like a classic monoatomic gas below this threshold pressure [8]. To see if we could discern this transition in our experiments, the BCl_3 plasma power was kept constant at 50 W and pressures were varied between 10 and 100 mTorr.

Figure 6.28 shows the summarized results of the experiment. Because the EEDFs were clearly neither Maxwellian nor Druyvesteyn, the equivalent kT_e and N_e values were computed directly from the EEDF. Clearly, the N_e values below 25 mTorr behave as if classical gas kinetics applied, with the density rising linearly with increasing pressure. And while kT_e decreases following a power curve only up to 20 mTorr, rising slightly at 25 mTorr, it too confirms Franz's findings. The values of N_e and kT_e above 25 mTorr also clearly show that the fundamental nature of the plasma has somehow changed. Instead of rising linearly with further increases in pressure, N_e drops linearly and kT_e rises instead of falling.

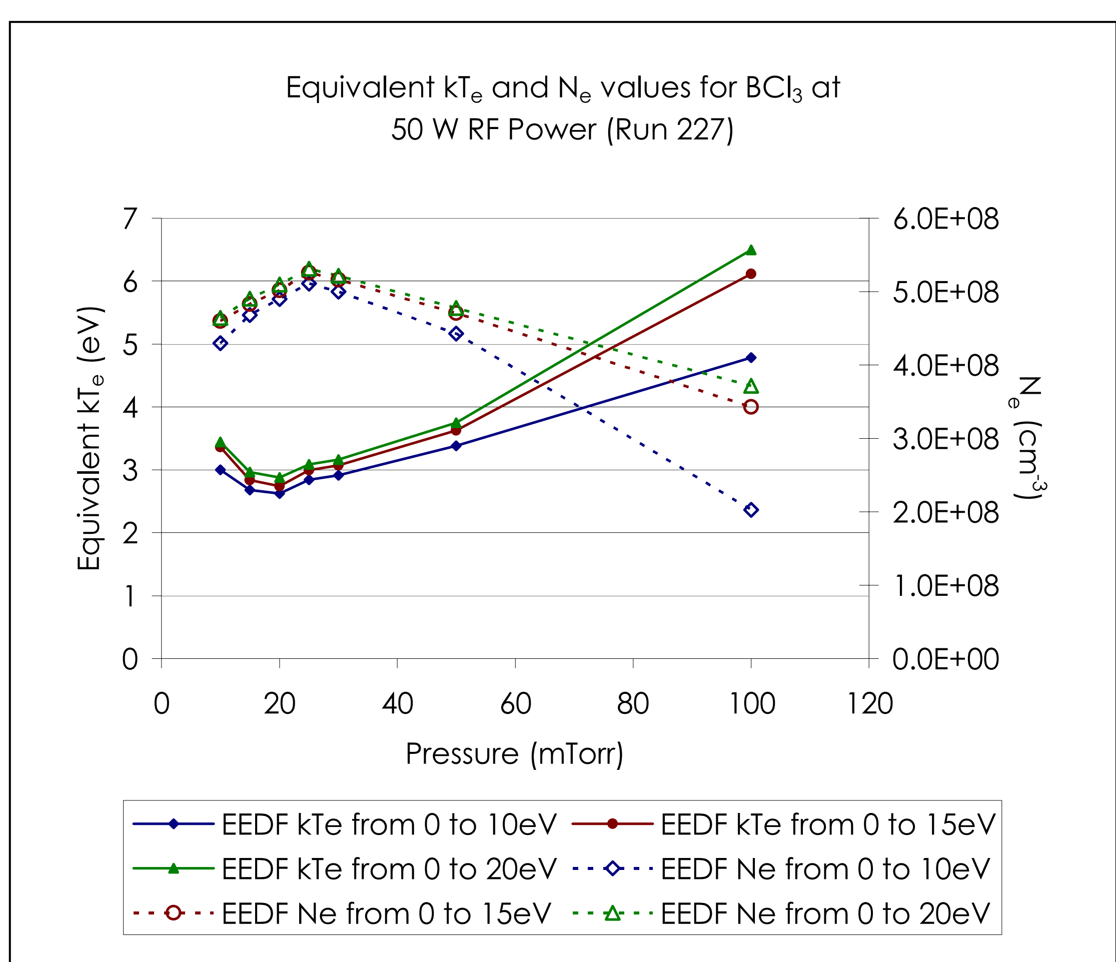

Figure 6.28: Comparison of the equivalent kT_e and N_e values obtained using various ranges for the EEDF in 50 W BCl_3 calibration plasmas.

Recall that in Figure 6.22 the direct calculation of equivalent kT_e and N_e from the EEDF was performed with different EEDF ranges, and that despite the choice between 20 eV and 30 eV, the trends and values were remarkably similar. A similar look at Figure 6.28 shows that this is no longer the case. As the EEDF range was increased from 10 eV to 20 eV, the trends in the values of N_e differ markedly. Based on these results, one can see that an EEDF range of 15 or 20 eV is necessary to properly capture all the active electrons in the EEDF when BCl_3 is involved. It was found, however, that increasing the EEDF range to 30 eV introduced excessive noise and artificially inflates both N_e and kT_e.

Figure 6.29 shows the evolution of the EEDF in BCl_3 with pressure above 25 mTorr. The change in distribution characteristics suggests that the plasma becomes increasingly electronegative with increased pressure. The trends observed in Figure 6.28 can be explained by Cl or BCl_3 scavenging the lower energy electrons for attachment and consequently decreasing N_e while increasing $<\varepsilon>$, particularly at higher pressures. In fact, R. Gottscho and C. Gaebe observed that at higher pressures (in the 100–300 mTorr range), both BCl_3^- and Cl^- ions were present, although the excitation frequencies used in their experiments only ranged between 50 and 750 kHz, and "[a]t higher frequencies, electrons have insufficient time

to attach before they are reheated and the instantaneous anion density in the sheath is greatly reduced [21].” It may also be possible that electron density decreases because of B–Cl bond vibrations that relax into BCl and Cl_2 or BCl_2 and Cl, similar to what is observed in N_2. This is based on the squelching not only of the very low electron energies, but also that of more energetic electrons around the BCl–Cl_2 bond energy of 5.65 eV, and BCl_2–Cl bond energy of 4.61 eV in the 100 mTorr EEDF.

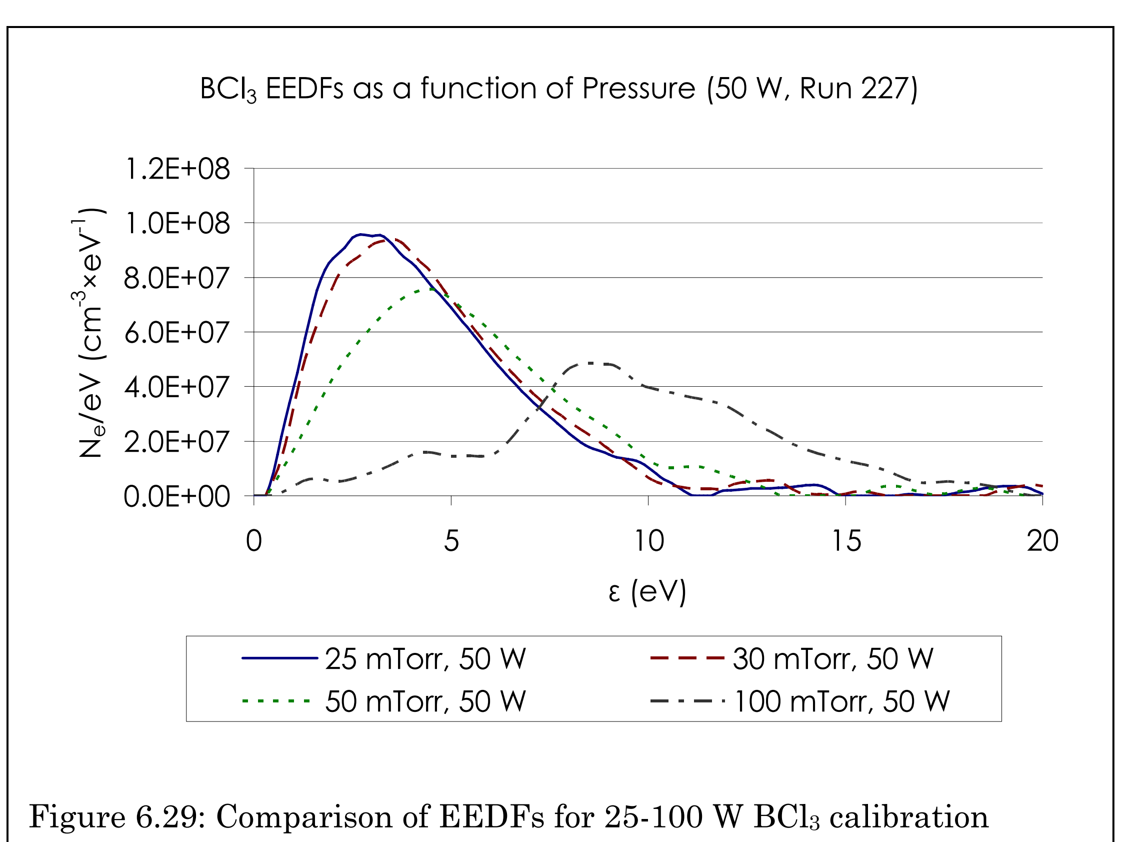

Figure 6.29: Comparison of EEDFs for 25-100 W BCl_3 calibration plasmas.

Power Variation

For this experiment, the pressure of the BCl_3 plasma was kept at 15 mTorr and the power was varied from 50 to 200 W. Unlike He or N_2, BCl_3 did not follow classical gas kinetics with increasing power.

Figure 6.30 shows trends in BCl_3 with increasing power. Unlike He or N_2, the increase in N_e saturates above 100 W, and the equivalent kT_e increases. While the effect of having kT_e increase if N_e remains constant with increasing power is not surprising, if the heating of electrons is based on elastic collisions, classical gas kinetics predicts that N_e would continue to increase well past 100 mTorr. However, if one compares the maximum N_e value in Figure 6.28 with the N_e saturation value in Figure 6.30, BCl_3 is likely to also exhibit increased electronegativity at higher powers. For comparison, C. Fleddermann and G. Hebner report that in a BCl_3 ICP at 20 mTorr and 200–400 W, Cl^- ions are present but BCl_3^- ions are not, and that their density increases with increasing power [27, 50]. This is consistent with our counterintuitive observation that both kT_e and N_e increase from 50 to 100 mTorr, and their conditions are closer to ours than are those of Gottscho and Gaebe. (See Figure 6.30.)

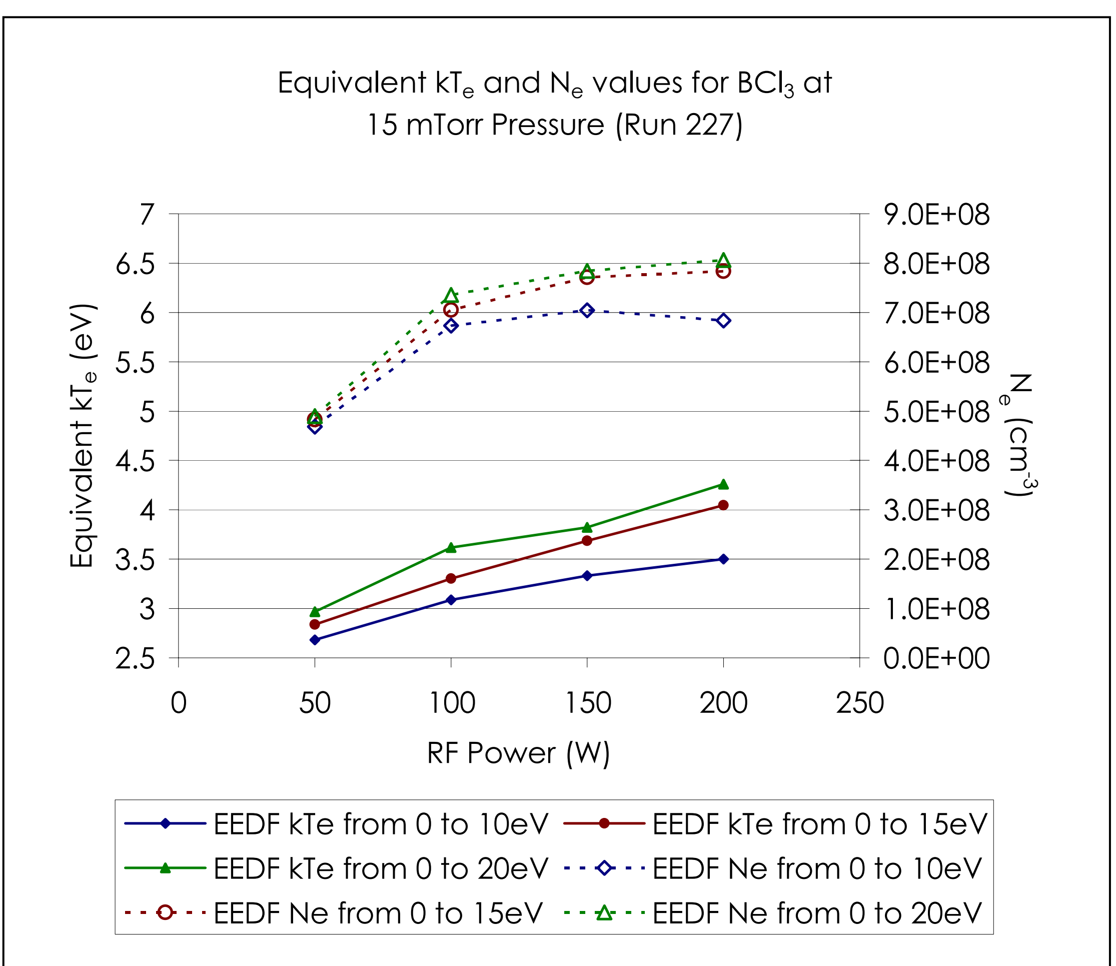

Figure 6.30: Comparison of the equivalent kT_e and N_e values obtained using various ranges for the EEDF in 15 mTorr BCl_3 plasmas.

6.7. BCl_3/N_2 Composition Experiments

BCl_3/N_2 plasmas appear to behave counterintuitively. The addition of N_2 to a BCl_3 plasma (up to a point) greatly increases the etch rate of both copper and GaAs materials. J. Sia and K. Nordheden conducted GaAs etch rate experiments at 15 mTorr and 50 W, and varied the concentration of BCl_3 and N_2, while B. Howard conducted his Cu etch rate experiments at 50 mTorr, −300 V, and 250°C [3, 4, 6, 12]. Because both experiments obtained very similar results relating etch rate to N_2 concentration, this Langmuir probe study of BCl_3/N_2 plasmas focused on J. Sia's and K. Nordheden's experimental conditions.

6.8. Effect of Composition on Negative Ion Density, the EEDF, kT_e, and N_e

EEDF and Second Derivative Structure—Evidence of Negative Ions

In both BCl_3 and N_2 plasmas, the EEDFs not only change their aggregate characteristics (i.e., $<\varepsilon>$, kT_e, and N_e) but also their overall electron distributions. By examining these changes, one can uncover important information that is often hidden when only the arithmetic mean of the electron energies (i.e., $<\varepsilon>$) is taken into consideration. This is especially important because for a collision with an electron to liberate an active etching species, the electron must be highly energetic, and this often means that it would be in the tail of the energy distribution.

Further, because negative ions are also attracted to the probe as negative charge carriers, they too can impact the I–V curve, and consequently what would initially appear to be an EEDF, but is really a summation of an EEDF and a scaled negative ion energy distribution function (negative ion EDF).

Figure 6.31 and Figure 6.32 show that BCl_3/N_2 EDFs appear to fall into two broad categories—mixtures where the BCl_3 EDF determines the shape of the mixture EDF, and mixtures where the N_2 EEDF visibly influences the shape of the EDF. For our region of interest (100%:0% $BCl_3:N_2$–40%:60% $BCl_3:N_2$), the EDFs (and consequently the energy probability function and second derivative) follow the BCl_3 EDF archetype, with the important exception of the region below 1 eV, which increases and then falls off again with N_2 addition. After examining the second derivative of the BCl_3/N_2 mixtures with an eye toward Amemiya's schematics (refer back to Figure 4.6), the shape of his schematics and that of our data was surprisingly similar. A second peak before V_p in the second derivative presented itself from 100% BCl_3 all the way down to 15% BCl_3 suggesting that 1) BCl_3 intrinsically produces negative ions (more likely Cl^- than BCl_3^- based on [50], but possibly BCl_3^- at lower powers) and 2) N_2 enhances negative ion formation if there is a sufficient concentration of BCl_3.

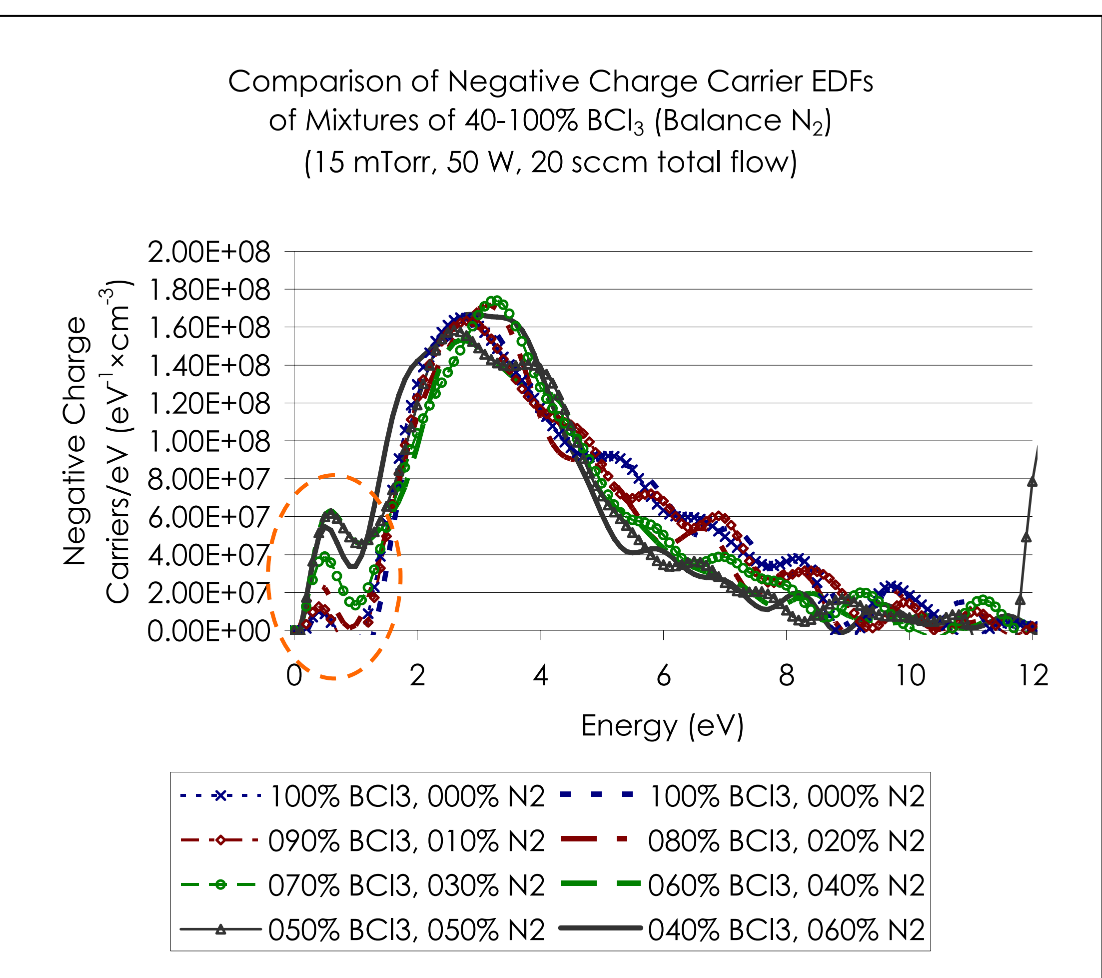

Figure 6.31: Comparison of EDFs of mixtures of 40-100% BCl_3 (balance N_2) plasmas at 15 mTorr and 50 W.

The mass of all anions is taken to be that of an electron.

N.B: Notice that in the highlighted area, as N_2 is added the area under the curve increases to a maximum at 40% N_2, and then begins to decrease.

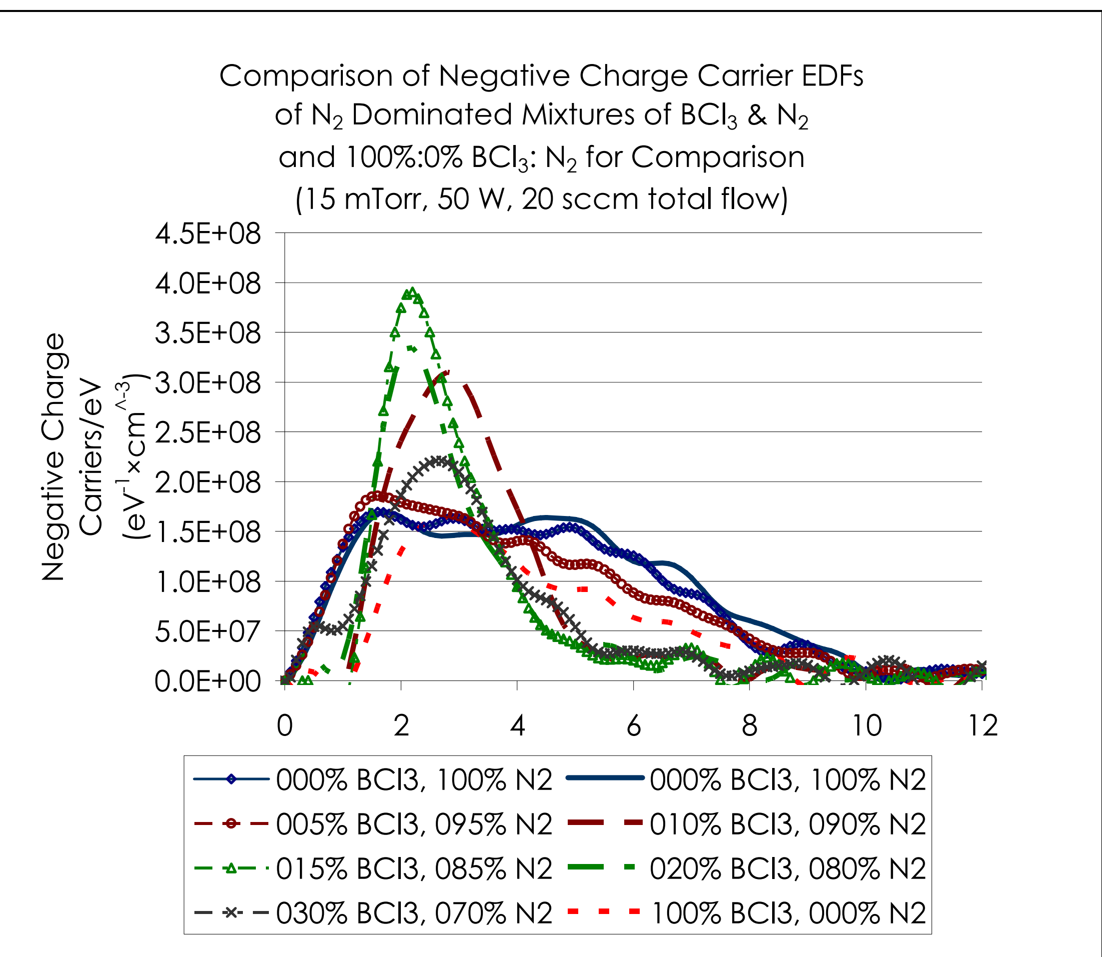

Figure 6.32: Comparison of EDFs of mixtures of 0-40% BCl_3 (balance N_2) plasmas with the EDF of a 100% BCl_3 plasma at 15 mTorr and 50 W.

The mass of all anions is taken to be that of an electron.

Aggregate Metrics—Equivalent kT_e and N_e

Originally, the MathCAD sheets used to calculate the equivalent kT_e and N_e values from an I–V sweep via an observed (electron) EDF ignored the possibility of negative ions and would treat them as just additional electrons. This resulted in the trends in Figure 6.33 labeled "Neg Ions as Electrons". The electron density in mixtures with >40% BCl_3 (<60% N_2) remained relatively constant and kT_e decreased with the addition of N_2 to BCl_3. Further, even after the MathCAD sheets were modified to eliminate the negative ions from consideration by zeroing out the area under the EDF curves with energy less than the local minimum at ~1 eV, there was no significant change in either the equivalent kT_e or N_e values. This, along with Figure 6.31's comparison of the electron portion of the EDFs shows that our initial hypothesis regarding kT_e influencing etch rate was wrong. In fact, when one discounts the negative ion portion of the EEDF (below 1 eV) the electrons all appear to follow a remarkably similar energy distribution to that of pure BCl_3 for plasma mixtures with >40% BCl_3 (<60% N_2).

It is worth noting that some BCl_3 always adsorbs onto the chamber walls or forms a BN film and then degasses into even "pure" N_2 plasmas. This adsorption and formation followed by degassing also explains why

the N_e observed at 100% N_2 in this experiment is so markedly lower than that of the initial N_2 calibrations due to the residual BCl_3 components.

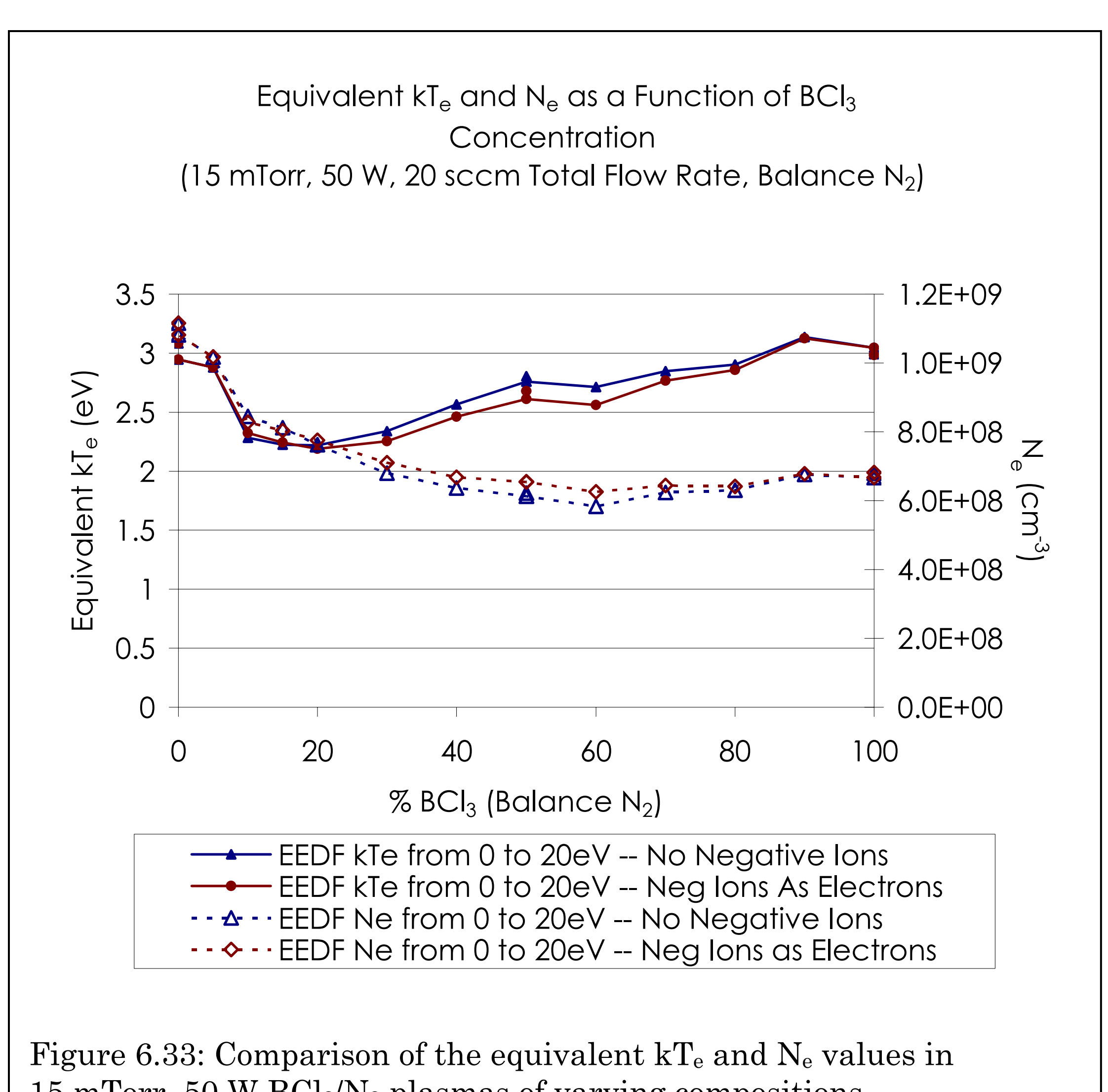

Figure 6.33: Comparison of the equivalent kT_e and N_e values in 15 mTorr, 50 W BCl_3/N_2 plasmas of varying compositions.

6.9. Comparing Negative Ion Density with Etch Rate in BCl_3/N_2 Plasmas

The apparent lack of change in the electron energy distribution from 0% to 60% N_2 (40% to 100% BCl_3) necessitates a change in thinking away from our original hypothesis that an increase in average electron energy (or kT_e) might be responsible for an etch rate increase as one adds N_2 to BCl_3 plasmas. Figure 6.34 clearly shows that to which was alluded before: the area under the negative ion peak in the EDF increases as N_2 is added up to a 40% N_2:60% BCl_3 mixture, and then decreases until the second peak becomes quite small in comparison at 85% N_2.

Interestingly, the area under the negative ion portion of the EDFs seems to follow a similar trend with N_2 concentration to that of the observed etch rate enhancement. In fact, comparing the magnitude of that area (i.e., the portion of the curve thought to correspond to negative ions, giving a relative negative ion concentration) with both the GaAs and Cu etch rate curves (Figure 6.34 to Figure 2.1 and Figure 2.2), one is struck by their similarity. Both etch rate and negative ion densities peak between 40% and 60% N_2. While this does not imply a causative relationship, previous work by Hebner and Fleddermann in an ICP at 10 mTorr and 400 W using laser induced photodetachment showed a 67% increase in Cl^- ion density in a 33% N_2:67% BCl_3 plasma over pure BCl_3,

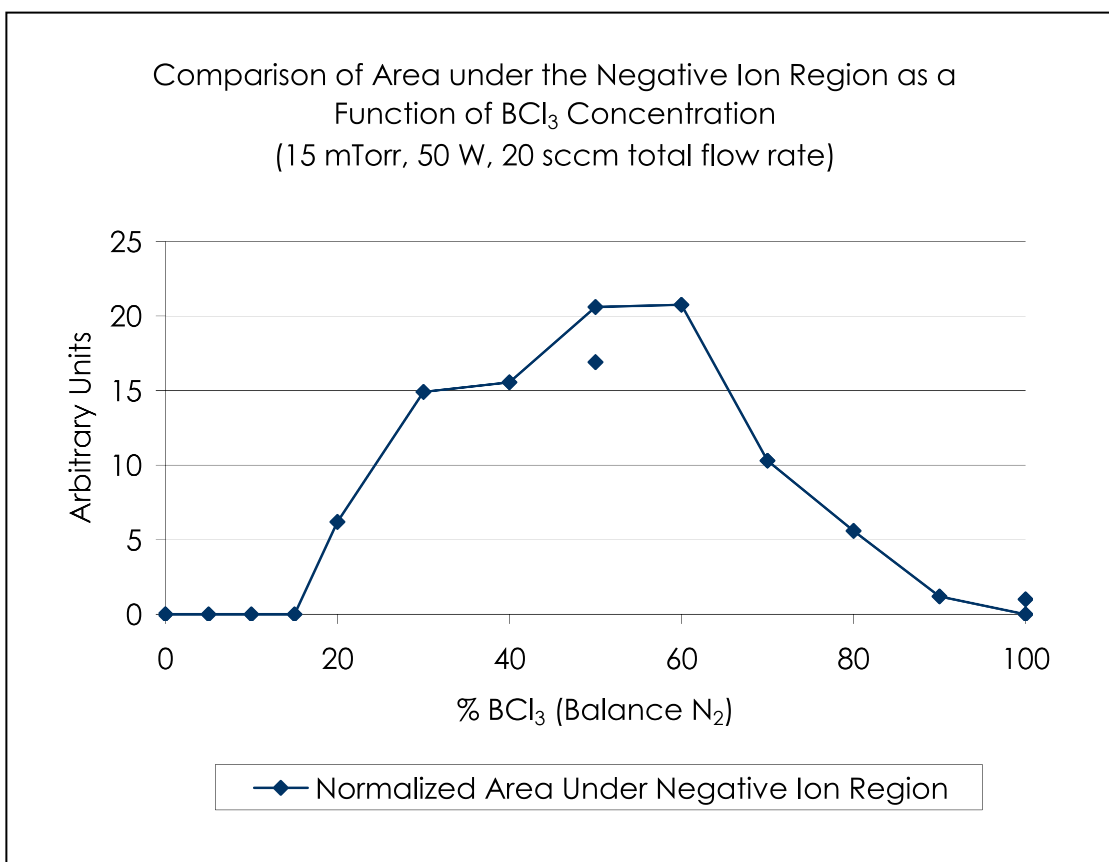

Figure 6.34: Comparison of normalized area under the negative ion region of the EEPF (or second derivative).

and failed to detect any BCl_x^- ions [50]. Also, using laser induced fluorescence (LIF) they observed a 400% increase in Cl^{+*} metastable ion density at the same 33% N_2:67% BCl_3 ratio over pure BCl_3 which could directly contribute to an etch rate increase [27].

In [50] and a later work [51], Fleddermann and Hebner propose a set of reactions based on Breitbarth's, Rothe's, and Howard's results and suppositions [3, 49, 52] starting with vibrationally excited N_2 or N_2

metastables that create Cl neutrals from BCl_3 or BCl radicals, see Equation (6.1). These Cl neutrals then ionize into active etching species or recombine into a Cl_2 molecule (ostensibly at a surface, but Cl might recombine into Cl_2 in the gas phase as well), and finally dissociate into Cl^- ions and Cl neutrals upon re-entering the plasma, see Equations (6.2) and (6.3).

$$\begin{gathered} N_2^* + BCl_3 \rightarrow BCl + 2Cl + N_2 \\ N_2^* + BCl \rightarrow B^* + Cl + N_2 \end{gathered} \tag{6.1}$$

$$Cl + e^- \rightarrow Cl^+ + 2e^- \; OR \; \begin{gathered} 2Cl \xrightarrow{Surface} Cl_2 \\ 2Cl \xrightarrow{Gas\ Phase} Cl_2 \end{gathered} \tag{6.2}$$

$$e^- + Cl_2 \rightarrow Cl + Cl^- \tag{6.3}$$

Unfortunately, although they examined electron density, none of the previous authors examined the actual distribution of electrons. Further, Hebner and Fledermann only investigated 100%:0% BCl_3:N_2–50%:50% BCl_3:N_2 mixtures and conducted their experiments in an ICP [27, 50, 51]; and Breitbarth only investigated 0%:100% BCl_3:N_2–5%:95% BCl_3:N_2 mixtures and conducted his experiments in a BCl_3/N_2 plasma afterglow [52]. Although their experimental conditions differ from those in this work, similarities do exist. Hebner's and Fleddermann's results in an ICP in particular are very similar to those of our work in

BCl_3/N_2 plasmas, especially when one considers that their negative ion densities peak at 33% N_2 (67% BCl_3) and ours peak at 40%.

For pure BCl_3 plasmas, however, N_2 does not play a role so another possible pathway comes to mind if the observed negative ions are responsible for catalyzing the formation of active species. The direct formation of negative ions from $e^- + BCl_3 \rightarrow BCl_2 + Cl^-$ dissociation has a very low threshold energy (0.14 eV), and is likely to be occur whether or not N_2 is present in the plasma. It could be followed by the electron detachment reaction $e^- + Cl^- \rightarrow Cl + 2e^-$ that also has a relatively low threshold energy (3.61 eV) [53]. The Cl neutral could then continue along any number of paths to become an active etch species. This direct dissociation, along with the recombination and ionization reactions described in Equations (6.2) and (6.3) could adequately explain why one would see Cl^- ions in low pressure, RF BCl_3 plasmas.

Chapter 7. Conclusions

This work set out to conduct Langmuir probe measurements in BCl_3/N_2 to help determine the cause of the etch rate enhancement seen by J. Sia [4, 6]. Sia posited that the two remaining viable causes of rate enhancement were an increase in kT_e and/or energy transfer from N_2 metastables. The observed EDFs in BCl_3/N_2 composition experiments show that adding N_2 to a BCl_3 plasma *does not* increase kT_e or <ε> at concentrations up to 60% N_2, in fact a small decrease was observed. Therefore, a change in kT_e or <ε> is not responsible for the etch rate enhancement. Further, while J. Sia did see a small (<20%) increase in N_e, in this work N_e decreased slightly, suggesting the value remains nearly constant and is not sufficient to explain the etch rate enhancement. This leaves N_2 metastables as the last viable mechanism to explain the increase in etch rate, and with other work implicating N_2 metastables in the creation active etch species produced from BCl_3 it appears very likely that this is the case.

What is remarkably coincidental is that the increase in negative ions observed in this work mirrors the etch rate enhancement observed by Howard, Nordheden, and Sia [4, 6, 12]. This in and of itself still does not explain the etch rate enhancement because negative ions do not participate in any etching mechanism since they are repelled by the strong negative DC bias that the powered electrode acquires. It does, however, become much

more plausible that the increase in negative ions is a consequence of a process (or processes) that both produces negative ions as well as active species.

As N_2 is added, the negative ions are most likely a consequence of the production of active etch species due to the interaction of BCl_3 and BCl_x with N_2 metastables and vibrationally excited N_2 molecules through the direct dissociation reactions of BCl_x mentioned in the previous chapter. The most likely pathway is that of vibrationally excited N_2 and N_2 metastable species starting a reaction chain that creates Cl neutrals that enhance etch species formation or recombine and form negative ions that are quickly repelled back into the bulk plasma [27, 49-52]. The specifics of this mechanism were presented in Section 6.9, and are well documented in the literature.

This clearly suggests new directions for study. Perhaps using similar techniques to examine other mixtures of tri-, tetra-, and hexa-halides mixtures with N_2; investigate other additives to BCl_3 that have active metastables like N_2; or explore strongly electronegative additives such as SF_6, which would be more likely to induce electron temperature changes than N_2 would be good starting points. This would help to separate out different mechanisms of etch rate enhancement as well as the differences and commonalities of BCl_3, $SiCl_4$, and SF_6 mixtures.

"Sit down before fact as a little child,
be prepared to give up every preconceived notion,
follow humbly wherever
and to whatever abysses nature leads,
or you will learn nothing."

—Thomas Henry Huxley

References

[1] G. E. Moore, "Cramming more components onto integrated circuits (Cramming more components onto integrated circuit for improved reliability and cost)," *Electronics,* vol. 38, pp. 114-117, 1965.

[2] R. Alapati, "Reactive ion etching of SiC SF_6/He plasmas," Thesis (M.S.), University of Kansas, Chemical and Petroleum Engineering, 2004.

[3] B. J. Howard, and C. Steinbrüchel, "Reactive ion etching of copper with BCl_3 and $SiCl_4$: Plasma diagnostics and patterning," *Journal of Vacuum Science & Technology A: Vacuum, Surfaces, and Films,* vol. 12, pp. 1259, 1994.

[4] K. J. Nordheden, and J. F.-F. Sia, "Characterization of BCl_3/N_2 plasmas," *Journal of Applied Physics,* vol. 94, no. 4, pp. 2199-2202, 2003.

[5] K. J. Nordheden, K. Upadhyaya, Y. S. Lee *et al.*, "GaAs Etch Rate Enhancement with SF_6 Addition to BCl_3 Plasmas," *Journal of The Electrochemical Society,* vol. 147, no. 10, pp. 3850-3852, 2000.

[6] J. F.-F. Sia, "Characterization of BCl_3/N_2 plasmas," Thesis (M.S.), University of Kansas, Chemical and Petroleum Engineering, 2002.

[7] D. Basak, T. Nakanishi, and S. Sakai, "Reactive ion etching of GaN using BCl3, BCl3/Ar and BCl3/N2 gas plasmas," *Solid State Electronics,* vol. 44, no. 4, pp. 725-728, 2000.

[8] G. Franz, "Comprehensive analysis of chlorine-containing capacitively coupled plasmas," *Journal of Vacuum Science & Technology A: Vacuum, Surfaces, and Films,* vol. 23, pp. 369, 2005.

[9] A. Grill, *Cold plasma in materials fabrication: from fundamentals to applications*, Piscataway, NJ; New York: IEEE Press; Institute of Electrical and Electronics Engineers, 1994.

[10] K. J. Nordheden, and J. T. Verdeyen, "The Effect of Oxygen on the Etch Rate of NF_3 Discharges," *Journal of The Electrochemical Society,* vol. 133, pp. 2168, 1986.

[11] A. Picard, G. Turban, and B. Grolleau, "Plasma diagnostics of a SF 6 radiofrequency discharge used for the etching of silicon," *Journal of Physics D. Applied Physics,* vol. 19, pp. 991-1005, 1986.

[12] B. J. Howard, "A Plasma Diagnostic Study of the Reactive Etching of Copper," Doctor of Philosophy, Materials Engineering, Renssalaer Polytechnic Institute, Troy, New York, 1993.

[13] M. M. Turner, and M. B. Hopkins, "Anomalous sheath heating in a low pressure rf discharge in nitrogen," *Physical Review Letters,* vol. 69, 1992.

[14] G. Gozadinos, M. M. Turner, and D. Vender, "Collisionless Electron Heating by Capacitive rf Sheaths," *Physical Review Letters,* vol. 87, no. 13, pp. 135004, 2001.

[15] M. B. Hopkins, "Langmuir Probe Measurements in the Gaseous Electronics Conference RF Reference Cell," *Journal of Research of the National Institute of Standards and Technology,* vol. 100, no. 4, 1995.

[16] H. Amemiya, "Probe diagnostics in negative ion containing plasma," *Journal of the Physical Society of Japan,* vol. 57, no. 3, pp. 887-902, 1988.

[17] H. Amemiya, "Plasmas with negative ions–probe measurements and charge equilibrium," *Journal of Physics D: Applied Physics,* vol. 23, pp. 999-1014, 1990.

[18] B. M. Annaratone, and N. S. J. Braithwaite, "Comparison of a passive(filtered) and an active(driven) probe for r. f. plasma diagnostics," *Measurement Science and Technology,* vol. 2, no. 8, pp. 795-800, 1991.

[19] F. F. Chen, "RF Langmuir Probes Revisited," *GEC*, 2005.

[20] R. N. Franklin, "A critique of models of electronegative plasmas," *Plasma Sources Science and Technology,* vol. 10, no. 2, pp. 162-167, 2001.

[21] R. A. Gottscho, and C. E. Gaebe, “Negative ion kinetics in RF glow discharges,” *IEEE Transactions on Plasma Science,* vol. 14, no. 2, 1986.

[22] M. B. Hopkins, and P. Heynen, *Radio Frequency Langmuir Probe*, USA US 7015703 B2,to Scientific Systems Research Ltd, U. S. PTO, 2006.

[23] A. Karamcheti, and C. Steinbrüchel, “Parametrization of Laframboise’s results for spherical and cylindrical Langmuir probes,” *Journal of Vacuum Science & Technology A: Vacuum, Surfaces, and Films,* vol. 17, pp. 3051, 1999.

[24] A. I. Kilvington, R. P. Jones, and J. D. Swift, “Effect of ac amplitude on the measurement of electron energy distribution functions,” *Journal of Scientific Instruments,* vol. 44, no. 7, pp. 517-520, 1967.

[25] A. P. Paranjpe, J. P. McVittie, and S. A. Self, “A tuned Langmuir probe for measurements in rf glow discharges,” *Journal of Applied Physics,* vol. 67, pp. 6718, 1990.

[26] I. D. Sudit, and R. C. Woods, “A study of the accuracy of various Langmuir probe theories,” *Journal of Applied Physics,* vol. 76, pp. 4488, 1994.

[27] G. A. Hebner, C. B. Fleddermann, and P. A. Miller, “Metastable chlorine ion kinetics in inductively coupled plasmas,” *Journal of Vacuum Science & Technology A: Vacuum, Surfaces, and Films,* vol. 15, pp. 2698, 1997.

[28] M. J. Druyvesteyn, “Der Niedervoltbogen,” *Zeitschrift für Physik A Hadrons and Nuclei,* vol. 64, no. 11, pp. 781-798, 1930.

[29] H. M. Mott-Smith, and I. Langmuir, “The theory of collectors in gaseous discharges,” *Physical Review,* vol. 28, 1926.

[30] M. A. Lieberman, and A. J. Lichtenberg, *Principles of plasma discharges and materials processing*, New York: Wiley, 1994.

[31] R. L. Merlino, “Understanding Langmuir probe current-voltage characteristics,” *American Journal of Physics,* vol. 75, no. 12, pp. 1078-1085, 2007.

[32] N. Hershkowitz, "How Langmuir Probes Work," *Plasma Diagnostics, Discharge parameters and Chemistry*, O. Auciello, ed., 1989.

[33] I. Langmuir, “Positive Ion Currents from the Positive Column of Mercury Arcs,” *Science,* vol. 58, no. 1502, pp. 290-291, 1923.

[34] F. F. Chen, "Personal Communication: RF Probe Structure and OML Analysis Technique," 2007.

[35] L. J. Overzet, and M. B. Hopkins, “Comparison of electron-density measurements made using a Langmuir probe and microwave interferometer in the Gaseous Electronics Conference reference reactor,” *Journal of Applied Physics,* vol. 74, pp. 4323, 1993.

[36] Scientific Systems, *SmartProbe Technical Note #9*, 2002.

[37] S. V. Singh, “Investigation of ICP RF discharges by means of a Langmuir probe ”, Fakultät für Physik und Astronomie, Ruhr-Universität Bochum, Bochum, 2004.

[38] Z. Sternovsky, and S. Robertson, “Langmuir probe interpretation for plasmas with secondary electrons from the wall,” *Physics of Plasmas,* vol. 11, pp. 3610, 2004.

[39] J. G. Laframboise, *Theory of spherical and cylindrical Langmuir probes in a collisionless Maxwellian plasma at rest*, University of Toronto, Institute for Aerospace Studies, Toronto, 1966.

[40] M. Mausbach, “Parametrization of the Laframboise theory for cylindrical Langmuir probe analysis,” *Journal of Vacuum Science & Technology A: Vacuum, Surfaces, and Films,* vol. 15, pp. 2923, 1997.

[41] C. Steinbrüchel, “A new method for analyzing Langmuir probe data and the determination of ion densities and etch yields in an etching plasma,” *Journal of Vacuum Science & Technology A: Vacuum, Surfaces, and Films,* vol. 8, pp. 1663, 1990.

[42] Scientific Systems, *SmartProbe Technical Note #3*, 2002.

[43] Scientific Systems, *SmartProbe Technical Note #2*, 2002.

[44] R. N. Franklin, "Electronegative plasmas-why are they so different?," *Plasma Sources Science and Technology,* vol. 11, no. 3A, pp. A31-A37, 2002.

[45] K. Wiesemann, "The influence of electron emission on probe characteristics," *Zeitschrift für Physik A Hadrons and Nuclei,* vol. 219, no. 5, pp. 462-466, 1969.

[46] W. S. Cleveland, "Robust locally weighted regression and smoothing scatterplots," *Journal of the American Statistical Association,* vol. 74, no. 368, pp. 829-836, 1979.

[47] W. S. Cleveland, and S. J. Devlin, "Locally weighted regression: an approach to regression analysis by local fitting," *Journal of the American Statistical Association,* vol. 83, no. 403, pp. 596-610, 1988.

[48] M. V. Kurepa, and D. S. Belic, "Electron-chlorine molecule total ionisation and electron attachment cross sections," *Journal of Physics B: Atomic and Molecular Physics,* vol. 11, no. 21, pp. 3719-3729, 1978.

[49] E. W. Rothe, B. P. Mathur, and G. P. Reck, "Measurement of boron trihalide electron affinities: correlation with boron-nitrogen adduct strengths," *Inorganic Chemistry,* vol. 19, no. 4, pp. 829-831, 1980.

[50] C. B. Fleddermann, and G. A. Hebner, "Negative ion densities in chlorine-and boron trichloride-containing inductively coupled plasmas," *Journal of Vacuum Science & Technology A: Vacuum, Surfaces, and Films,* vol. 15, pp. 1955, 1997.

[51] C. B. Fleddermann, and G. A. Hebner, "Measurements of relative BCl density in BCl-containing inductively coupled radio frequency plasmas," *Journal of Applied Physics,* vol. 83, pp. 4030, 1998.

[52] F. W. Breitbarth, "Spectroscopic investigation of energy-transfer reactions in BCl_3/N_2 discharges," *Plasma Chemistry and Plasma Processing,* vol. 12, no. 3, pp. 261-274, 1992.

[53] E. Meeks, P. Ho, A. Ting *et al.*, "Simulations of BCl_3/Cl/Ar plasmas with comparisons to diagnostic data," *Journal of Vacuum Science & Technology A: Vacuum, Surfaces, and Films,* vol. 16, pp. 2227, 1998.

Appendix A. Chamber Description

This section is excerpted from J. Sia's Thesis [6].

A.1. Reactive Ion Etching System

The reactive ion etching system used to generate the plasma and etch GaAs samples was a Plasma-Therm 790 series parallel plate system. A schematic of the equipment is shown in Figure A.35. The system generates the plasma at the standard frequency of 13.56 MHz and has the capability to control RF power, DC Bias, flow rate of inlet gases, and pressure.

The chamber is 15" in diameter and 10" in height. The diameter of the powered electrode is 10". The system is comprised of a parallel plate capacitively coupled electrodes separated by 3 inches. Samples as large as 8" can be loaded into the system manually by lifting the chamber lid. The lower electrode in the system, where the sample is placed, is the powered one and the chamber walls are grounded. The chamber is equipped with three Pyrex glass viewports to facilitate visual inspection of the plasma and can be used for plasma diagnostic tools. The gases enter the system from a showerhead in the chamber lid.

The lower powered electrode is temperature controlled by a water circulator system (Neslab RTE 111). The base pressure inside the system is maintained at 10^{-6} Torr to avoid any contamination from the atmosphere. This low pressure is maintained by pumping the chamber through a 150 l/s Leybold turbo-molecular pump backed by a 32 cfm Leybold rotary vane mechanical pump.

All the controls in the system are performed by control software operational on Microsoft Windows 3.0. This software provides a graphical interface for the user to operate and adjust various parameters.

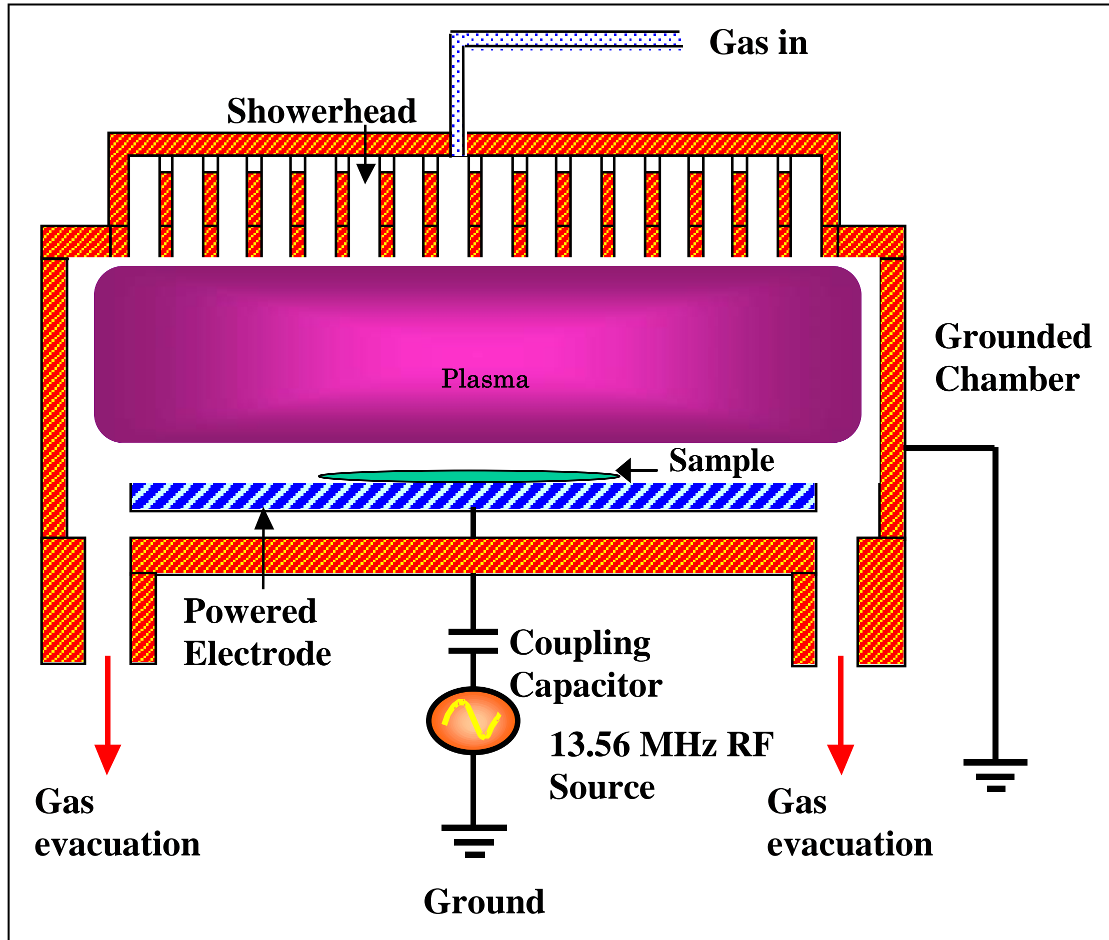

Figure A.35: Schematic of the PlasmaTherm 790 series capacitively coupled plasma chamber used in the Langmuir probe and etching experiments [6].

Appendix B. Sample MathCAD Worksheets

Langmuir Probe Data Analysis (EEDF)

At its simplest, a Langmuir probe is simply a wire (or disk) placed in the plasma. The probe collects mostly electrons when biased positively and mostly ions when biased negatively. When the bias is negative, the electrons that are collected are the ones with sufficient energy to overcome the potential barrier of the probe. In this exercise we will analyze data from a cylindrical Langmuir probe. The random current of electrons to a surface in a plasma is

$$J_{sat} = n_e q \sqrt{kT_e / 2\pi m_e}$$

where J_{sat} is the current density, n_e is the electron density, m_e is the electron mass, and q is the elementary charge. The surface is assumed to be at the plasma potential. The electron temperature T_e will be written in electron volts below, which means that the thermal energy will be qT_e rather than kT_e. When the probe is at the plasma potential, the current collected is the **saturation current** I_{sat}:

$$I_{sat} = A_p J_{sat} = 2\pi a L J_{sat}$$

where a is the probe radius, L is the probe length and A_p is the probe area.

When the probe voltage is negative relative to the plasma potential, Vplasma, the current is estimated as:

$$I(V) = I_{sat} \exp[(V - V_{plasma})/T_e]$$

Vplasma is the potential in the space between plasma electrons and ions.

Characteristics of the probe used to acquire the data:

$D_p := 0.25 \cdot 10^{-3}$ Probe diameter in m. The wire diameter is $D_p \cdot m = 0.25\,mm$.

$L_p := 0.5 \cdot 10^{-2}$ Probe length in m. The length is approximately $L_p \cdot m = 0.5\,cm$.

$A_p := \pi \cdot D_p \cdot L_p$ Probe surface area in m^2. The area is approximately $A_p \cdot m^2 = 3.927\,mm^2$

Required Physical Constants

$q_e := 1.602 \times 10^{-19} C$ Elementary Charge (of an electron)

$m_e := 9.109 \times 10^{-31} kg$ Mass of an Electron

$eV := 1.602 \times 10^{-19} J$

Import the sweep data from a CSV File:

RAW := .....\Run 121K1 - 100% He - 40 mTorr 175 W -360 V from -20.00 to 60.00 by 0.10 V.csv

Probe current in amps versus probe voltage

$\mathrm{rows(RAW)} = 801$

Rows in the file...

$dV := \left|RAW_{1,0} - RAW_{0,0}\right|$

$dV = 0.1$

$$RAW := \begin{cases} \mathrm{reverse(RAW)} & \text{if } RAW_{1,0} > RAW_{2,0} \\ RAW & \text{otherwise} \end{cases}$$

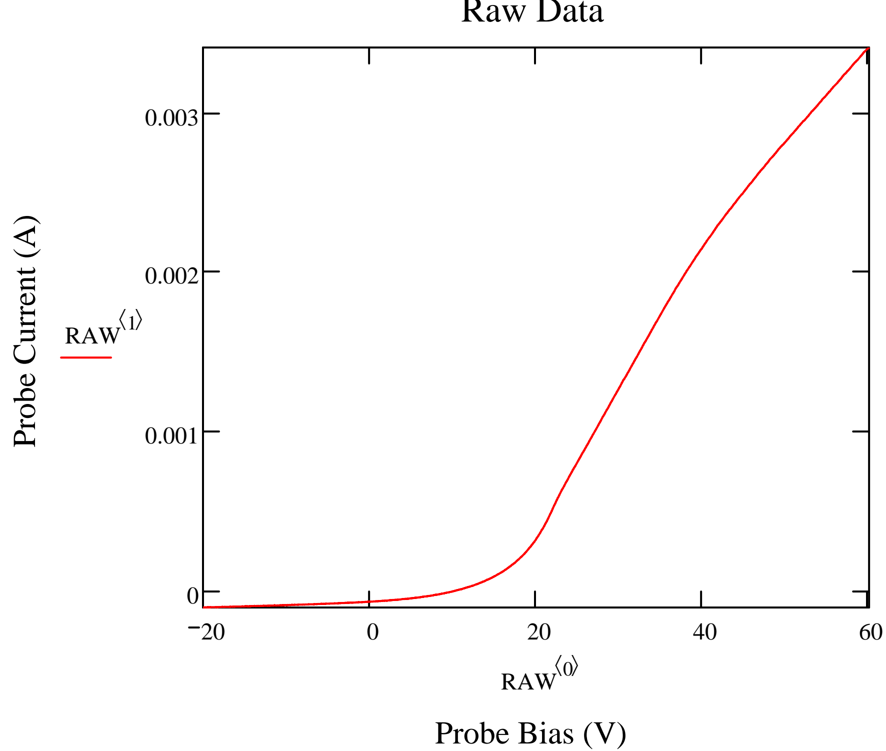

Limit the sweep data to a useful region.

$VRaw_{min} := RAW_{0,0}$ $VRaw_{max} := RAW_{rows(RAW)-1,0}$

$VRaw_{min} = -20$ $VRaw_{max} = 60$

$V_{min} := -10$ $idx_{min} := rows(RAW) - 1 - floor\left(\frac{VRaw_{max} - V_{min}}{dV}\right)$ $idx_{min} = 101$

$V_{max} := 50$ $idx_{max} := rows(RAW) - 1 - floor\left(\frac{VRaw_{max} - V_{max}}{dV}\right)$ $idx_{max} = 701$

Create an initial DATA array that has the current data, the first derivative, and the second derivative.

$DAT := submatrix(RAW, idx_{min}, idx_{max}, 0, 1)$ $kdx := 2, 3 .. rows(DAT) - $

$DAT^{\langle 1 \rangle} := 10^6 \cdot DAT^{\langle 1 \rangle}$ Convert currents to microamps $DatRows := rows(DAT) - 1$

$$DAT_{kdx,2} := \frac{1}{12 \cdot dV} \cdot \left(-DAT_{kdx+2,1} + 8\,DAT_{kdx+1,1} - 8 \cdot DAT_{kdx-1,1} + DAT_{kdx-2,1}\right)$$

$$DAT_{kdx,3} := \frac{1}{12 \cdot dV^2} \cdot \left(-DAT_{kdx+2,1} + 16\,DAT_{kdx+1,1} - 30 \cdot DAT_{kdx,1} \cdots + 16 \cdot DAT_{kdx-1,1} - DAT_{kdx-2,1}\right)$$

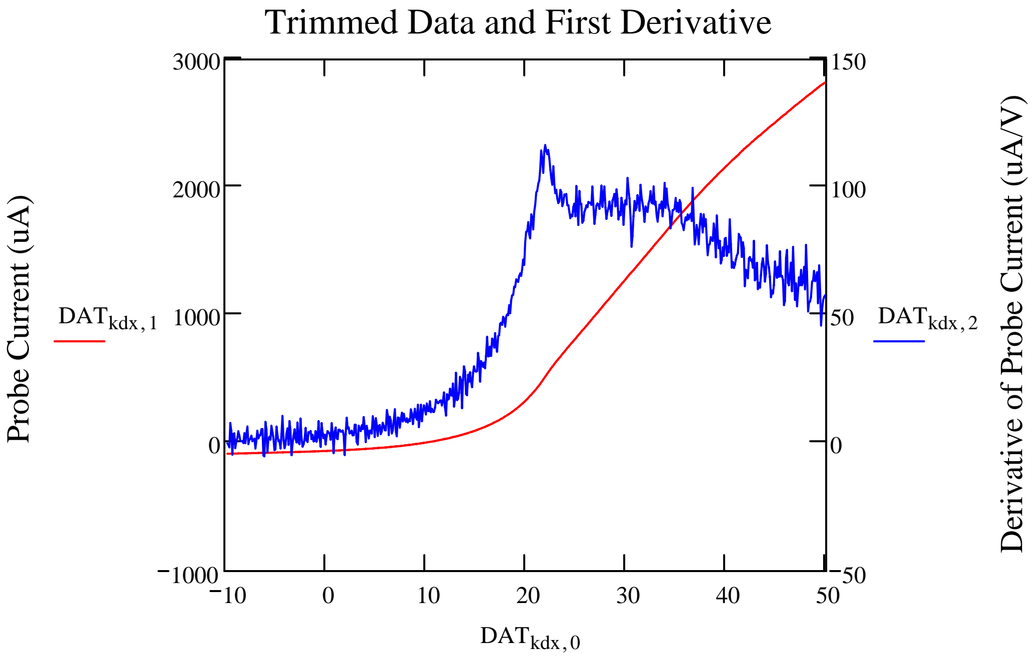

Smooth the original data, the first derivative, and the second derivative to see if they can be more usable.

$smoothrange := 0.5$

$DAT^{\langle 1 \rangle} := ksmooth\left(DAT^{\langle 0 \rangle}, DAT^{\langle 1 \rangle}, smoothrange\right)$

$DAT^{\langle 2 \rangle} := ksmooth\left(DAT^{\langle 0 \rangle}, DAT^{\langle 2 \rangle}, 2 \cdot smoothrange\right)$

$DAT^{\langle 3 \rangle} := ksmooth\left(DAT^{\langle 0 \rangle}, DAT^{\langle 3 \rangle}, 4 \cdot smoothrange\right)$

Find the Floating potential and the Plasma potential based on the smoothed data.

The floating potential is the potential at which the probe current is equal to zero

$$i_{Vf} := \left| \begin{array}{l} j \leftarrow DatRows - 1 \\ \text{while } DAT_{j,1} > 0 \\ \quad j \leftarrow j - 1 \end{array} \right.$$

$i_{Vf} = 196$ Find the index of Vf

$V_F := DAT_{i_{Vf},0}$

$V_F = 9.7$ This is the floating potential

The plasma potential is at first estimation equal to the maximum of the first derivative.

$i_{Vp} := \text{match}\left(\max\left(DAT^{\langle 2 \rangle}\right), DAT^{\langle 2 \rangle}\right)_0$

$i_{Vp} = 320$ Find the index of Vp

$i_{Vp} := i_{Vp}$ If you don't like that Vp, pick another one...

$V_P := DAT_{i_{Vp},0}$

$V_P = 22.1$ This is the plasma potential

extension := 5 points to plot before and after VF and VP

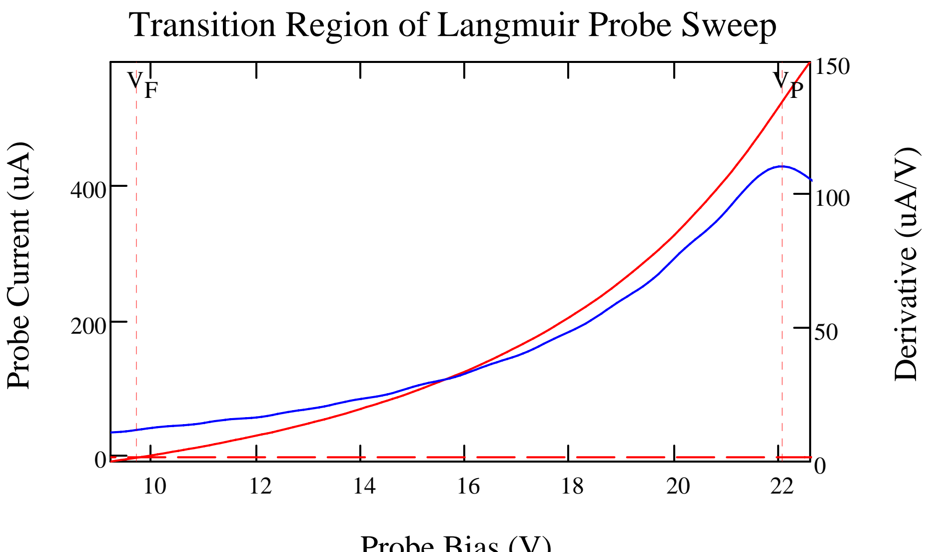

Create an EEPF and EEDF based on the second derivative and the found VP

$EERange := 20$ How many volts the EEPF and EEDF extend out

$$idx_{EEmin} := i_{Vp} - \frac{EERange}{dV}$$

$$EEF_V := \left(-submatrix\left(DAT, idx_{EEmin}, i_{Vp}, 0, 0\right) + V_P\right) \cdot eV \qquad EEF_V := reverse\left(EEF_V\right)$$

$$EEPF := 2 \cdot \frac{\sqrt{2 \cdot m_e}}{{q_e}^3 \cdot A_p \cdot m^2} \cdot submatrix\left(DAT, idx_{EEmin}, i_{Vp}, 3, 3\right) \cdot \frac{\mu A}{V^2}$$

$$EEPF := \overrightarrow{(EEPF \cdot \Phi(EEPF))} \qquad EEPF := reverse(EEPF)$$ Manipulate EEPF to get it to behave...

$$EEDF := \overrightarrow{\left(EEPF \cdot \sqrt{EEF_V}\right)}$$

Note that both the EEPF and EEDF shouldn't have any negative values, so if the values are negative, we switch them to zero.

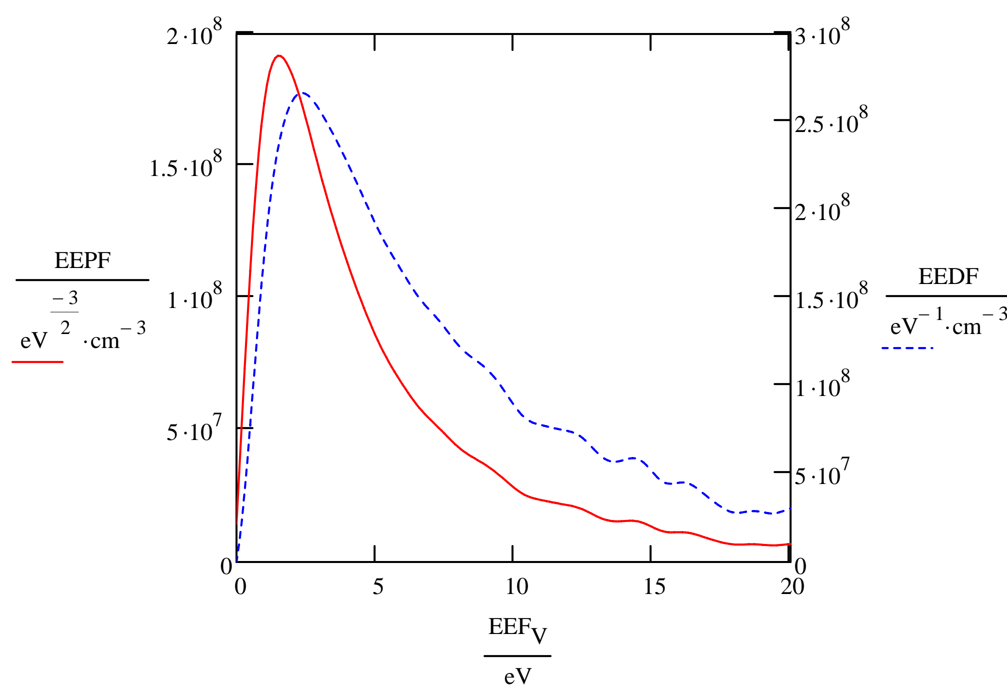

Try and find an equivalent kTe from the EEDF

Integrate the EEDF both with and without multiplying it by the voltage...

$$\text{Integral}_{\text{EEDF}} := \left[\sum_{m=0}^{\text{rows(EEDF)}-2}\left[\frac{1}{2}\cdot\left(\text{EEDF}_m + \text{EEDF}_{m+1}\right)\left(\text{EEF}_{V_{m+1}} + -\text{EEF}_{V_m}\right)\right]\right]$$

$$\text{WeightedIntegral}_{\text{EEDF}} := \sum_{m=0}^{\text{rows(EEDF)}-2}\left[\frac{1}{4}\cdot\left(\text{EEDF}_m + \text{EEDF}_{m+1}\right)\left(\text{EEF}_{V_{m+1}} + -\text{EEF}_{V_m}\right)\cdot\left(\text{EEF}_{V_{m+1}} + \text{EEF}_{V_m}\right)\right]$$

$\text{Integral}_{\text{EEDF}} = 2.226 \times 10^{9}\,\text{cm}^{-3}$ $\text{WeightedIntegral}_{\text{EEDF}} = 1.502 \times 10^{10}\,\text{eV}\cdot\text{cm}^{-3}$

$\text{Avg}_{\text{EE}} := \dfrac{\text{WeightedIntegral}_{\text{EEDF}}}{\text{Integral}_{\text{EEDF}}}$ $\text{Avg}_{\text{EE}} = 6.745\,\text{eV}$

$\text{kTe}_{\text{equiv}} := \dfrac{2}{3}\cdot\text{Avg}_{\text{EE}}$ $\text{kTe}_{\text{equiv}} = 4.497\,\text{eV}$

$N_e := \text{Integral}_{\text{EEDF}}$ $N_e = 2.226 \times 10^{9}\,\text{cm}^{-3}$

Compare the EEDF to a Maxwellian and Druyvesteyn with an equal aver electron energy (equivalent kTe for the Maxwellian)

$$dmaxwellian_e(\varepsilon, kT_e) := \frac{2}{\sqrt{\pi}} \cdot \frac{\sqrt{\varepsilon}}{\sqrt{kT_e^3}} \cdot e^{\frac{-\varepsilon}{kT_e}} \qquad 1 - \int_0^{EERange} dmaxwellian_e\left(\varepsilon, \frac{kTe_{equiv}}{eV}\right) d\varepsilon = 0.031$$

$$ddruyvesteyn_e(\varepsilon, kT_e, \alpha) := \frac{2}{\sqrt{\pi}} \cdot \frac{\sqrt{\varepsilon}}{\sqrt{kT_e^3}} \cdot \exp\left[-\left(\frac{\varepsilon}{kT_e}\right)^{\alpha}\right]$$

N.B. $\alpha = 2$ for a true Druyvesteyn

$$ndruyvesteyn_e(\varepsilon, kT_e, \alpha) := \frac{ddruyvesteyn_e(\varepsilon, kT_e, \alpha)}{\int_0^{\infty} ddruyvesteyn_e(\varepsilon, kT_e, \alpha)\, d\varepsilon}$$

$$avgEEndruy(kT_e, \alpha) := \int_0^{\infty} \varepsilon \cdot ndruyvesteyn_e(\varepsilon, kT_e, \alpha)\, d\varepsilon \qquad norm_{AvgEE}(\alpha) := avgEEndruy(1, \alpha)^{-1}$$

$\alpha := 2$ $\quad$ $\alpha = 2$ for a true Druyvesteyn $\quad$ $Avg_{EE} = 6.745\ eV$ $\quad$ $E := 0, dV .. EERange$

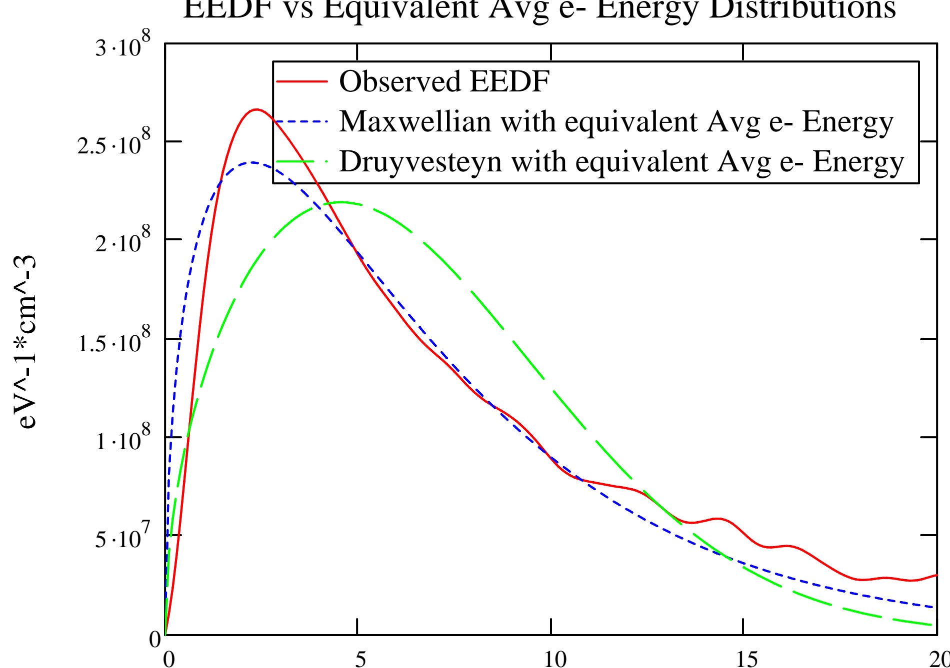

Excel Line for ease of import:

$$\text{Excel} := \text{augment}\left(\frac{kTe_{equiv}}{eV}, \frac{N_e}{cm^{-3}}\right)$$

Excel =

	0	1
0	4.497	$2.226 \cdot 10^9$

Error in the Distributions caused by limits

$$1 - \int_0^{EERange} dmaxwellian_e\left(\varepsilon, \frac{kTe_{equiv}}{eV}\right) d\varepsilon = 3.072\ \%$$

$$1 - \int_0^{EERange} ndruyvesteyn_e\left(\varepsilon, \frac{Avg_{EE}}{eV}, \alpha\right) d\varepsilon = 7.006 \times 10^{-3}\ \%$$

$$\frac{EEDF}{eV^{-1} \cdot cm^{-3}} =$$

	0
0	0
1	$1.071 \cdot 10^7$
2	$2.399 \cdot 10^7$
3	$4.015 \cdot 10^7$
4	$5.84 \cdot 10^7$
5	$7.799 \cdot 10^7$
6	$9.822 \cdot 10^7$
7	$1.184 \cdot 10^8$
8	$1.38 \cdot 10^8$
9	$1.566 \cdot 10^8$
10	$1.738 \cdot 10^8$
11	$1.894 \cdot 10^8$
12	$2.032 \cdot 10^8$
13	$2.154 \cdot 10^8$
14	$2.259 \cdot 10^8$
15	$2.348 \cdot 10^8$

Langmuir Probe Data Analysis (Log-Slope and SmartProbe)

A Langmuir probe is simply a wire (or disk) placed in the plasma. The probe collects mostly electrons when biased positively and mostly ions when biased negatively. When the bias is negative, the electrons that are collected are the ones with sufficient energy to overcome the potential barrier of the probe. In this exercise we will analyze data from a cylindrical Langmuir probe. The random current of electrons to a surface in a plasma is

$$J_{sat} = n_e q \sqrt{kT_e / 2\pi m_e}$$

where J_{sat} is the current density, n_e is the electron density, m_e is the electron mass, and q is the elementary charge. The surface is assumed to be at the plasma potential. The electron temperature T_e will be written in electron volts below, which means that the thermal energy will be qT_e rather than kT_e. When the probe is at the plasma potential, the current collected is the **saturation current** I_{sat}:

$$I_{sat} = A_p J_{sat} = 2\pi a L J_{sat}$$

where a is the probe radius, L is the probe length and A_p is the probe area.

When the probe voltage is negative relative to the plasma potential, Vplasma, the current is estimated as:

$$I(V) = I_{sat} \exp[(V - V_{plasma})/T_e]$$

Vplasma is the potential in the space between plasma electrons and ions.

Characteristics of the probe used to acquire the data:

$a := 0.125 \cdot 10^{-3}$ Probe radius in m. The wire diameter is 0.25 mm.

$L := 0.5 \cdot 10^{-2}$ Probe length in m. The length is approximately 1.05 cm.

$Ap := 2 \cdot \pi \cdot a \cdot L$ $Ap = 3.927 \times 10^{-6}$ Probe surface area in m^2.

Import the two sweeps and "average" data from a CSV File:

$DAT :=$ .....\Run 121A1 - 100% He - 125 mTorr 175 W -308 V from -20.00 to 60.00 by 0.10 V.csv

Probe current in amps versus probe voltage:

$\text{rows}(DAT) = 801$ Number of rows in the file.

$dV := \left| DAT_{1,0} - DAT_{0,0} \right|$ $dV = 0.1$

$DatRows := \text{rows}(DAT) - 1 - \text{floor}\left(\frac{21}{dV}\right)$ The last data row is numbered DatRows

$$DAT := \begin{array}{|l} \text{reverse}(DAT) \;\; \text{if} \;\; DAT_{1,0} > DAT_{2,0} \\ DAT \;\; \text{otherwise} \end{array}$$

$swp := 0 .. 0$

$DAT^{\langle 2\cdot swp+1\rangle} := 10^{6}\cdot DAT^{\langle 2\cdot swp+1\rangle}$ Switch to microamps

$n_{Smoothing} := 1$ $n_{Smthlow} := \text{floor}\left(-\frac{n_{Smoothing}}{2} + 1\right)$ $n_{Smthlow} = 0$

$n_{Smthhigh} := \text{floor}\left(\frac{n_{Smoothing}}{2}\right)$ $n_{Smthhigh} = 0$

$k := -n_{Smthlow}, -n_{Smthlow} + 1 .. DatRows - \left(n_{Smthhigh}\right)$

$$DAT_{Smth_{k,1}} := \sum_{i = n_{Smthlow}}^{n_{Smthhigh}} \frac{DAT_{k+i,1}}{n_{Smoothing}}$$

$DAT^{\langle 2\cdot swp+1\rangle} := DAT_{Smth}^{\langle 2\cdot swp+1\rangle}$

$$i_{Vf_{swp}} := \begin{array}{|l} j \leftarrow DatRows - 1 \\ \text{while } DAT_{j,2swp+1} > 0 \\ \quad j \leftarrow j - 1 \end{array}$$

$i_{Vf} = (342)$ Find the index of Vf

$Vf_{swp} := \left(DAT^{\langle 2\cdot swp\rangle}\right)_{i_{Vf_{swp}}}$ $Vf = (14.2)$ Find the Value of Vf

DAT2 := .....\Run 121A1 - 100% He - 125 mTorr 175 W -308 V from -20.00 to 60.00 by 0.10 V.csv

$\mathrm{rows}(DAT2) = 801$

$dV2 := \left| DAT2_{1,0} - DAT2_{0,0} \right| \qquad dV2 = 0.1$

$Dat2Rows := \mathrm{rows}(DAT2) - 1 - \mathrm{floor}\left(\frac{25}{dV}\right)$

$$DAT2 := \begin{cases} \mathrm{reverse}(DAT2) & \text{if } DAT2_{1,0} > DAT2_{2,0} \\ DAT2 & \text{otherwise} \end{cases}$$

$DAT2^{\langle 2\cdot swp+1\rangle} := 10^{6}\cdot DAT2^{\langle 2\cdot swp+1\rangle}$

$n2_{Smoothing} := 1 \qquad n2_{Smthlow} := \mathrm{floor}\left(-\frac{n2_{Smoothing}}{2} + 1\right) \quad n2_{Smthlow} = 0$

$n2_{Smthhigh} := \mathrm{floor}\left(\frac{n2_{Smoothing}}{2}\right) \qquad n2_{Smthhigh} = 0$

$k2 := -n2_{Smthlow}, -n2_{Smthlow} + 1 \,..\, Dat2Rows - \left(n2_{Smthhigh}\right)$

$$DAT2Smth_{k2,1} := \sum_{i = n2_{Smthlow}}^{n2_{Smthhigh}} \frac{DAT2_{k2+i,1}}{n2_{Smoothing}}$$

$DAT2^{\langle 2\cdot swp+1\rangle} := DAT2Smth^{\langle 2\cdot swp+1\rangle}$

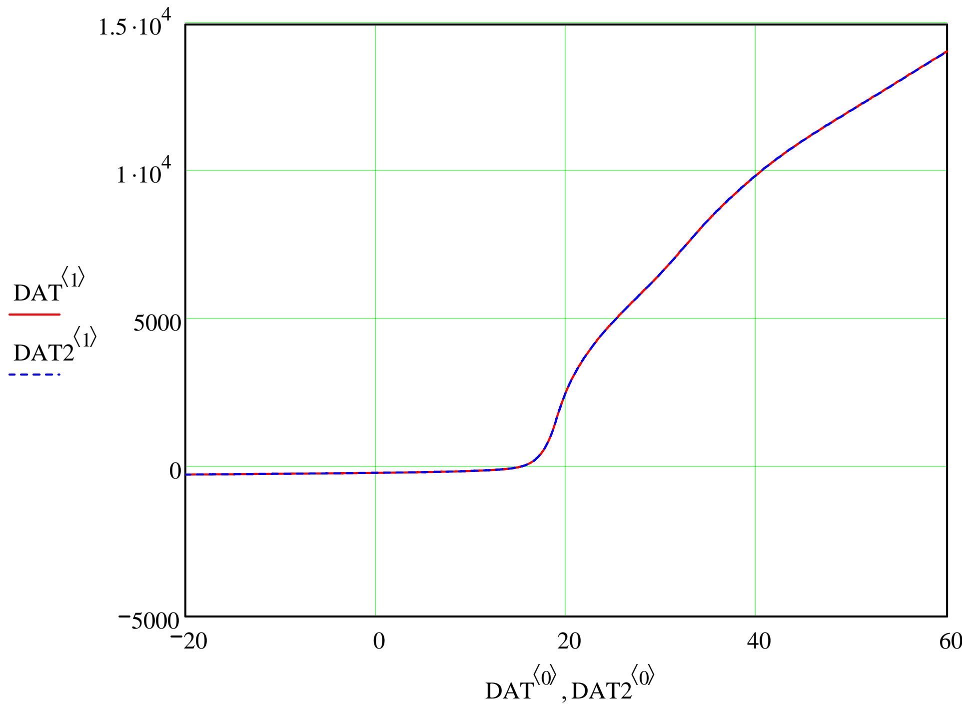
1.5·10^4
1·10^4
5000
0
−5000
−20
0
20
40
60
DAT⟨1⟩
DAT2⟨1⟩
DAT⟨0⟩, DAT2⟨0⟩

$$e_{satregion} := \text{floor}\left(\frac{15}{dV}\right)$$

$$e_{satregion2} := \text{floor}\left(\frac{10}{dV}\right)$$ Points

$$n := DatRows - \left(n_{Smthhigh}\right) - e_{satregion} .. DatRows - \left(n_{Smthhigh}\right)$$
$$n2 := Dat2Rows - \left(n2_{Smthhigh}\right) - e_{satregion2} .. Dat2Rows - \left(n2_{Smthhigh}\right)$$

$$Satregion_{n-\left(DatRows-n_{Smthhigh}-e_{satregion}\right),0} := DAT_{n,0}$$
$$Satregion2_{n2-\left(Dat2Rows-n2_{Smthhigh}-e_{satregion2}\right),0} := DAT2_{n2,0}$$

$$Satregion_{n-\left(DatRows-n_{Smthhigh}-e_{satregion}\right),1} := DAT_{n,1}$$
$$Satregion2_{n2-\left(Dat2Rows-n2_{Smthhigh}-e_{satregion2}\right),1} := DAT2_{n2,1}$$

$$LFsatParam := \text{line}\left(Satregion^{\langle 0 \rangle}, Satregion^{\langle 1 \rangle}\right)$$
$$LFsat2Param := \text{line}\left(Satregion2^{\langle 0 \rangle}, Satregion2^{\langle 1 \rangle}\right)$$

$$LFsatParam_1 = 341.094$$

$$LFsat2Param_1 = 345.039$$

$$k2 := n2_{Smthhigh} + 2 .. Dat2Rows + n2_{Smthlow} - 2$$

$$Deriv2_{k2,swp} := \frac{1}{12 \cdot dV2} \cdot \left(-DAT2_{k2+2,2 \cdot swp+1} + 8 \cdot DAT2_{k2+1,2 \cdot swp+1} \cdots + 8 \cdot DAT2_{k2-1,2 \cdot swp+1} + DAT2_{k2-2,2 \cdot swp+1}\right)$$

$LaFramsat(x) := LFsatParam_0 + LFsatParam_1 \cdot x$ $LaFramsat2(x) := LFsat2Param_0 + LFsat2Param_1 \cdot x$

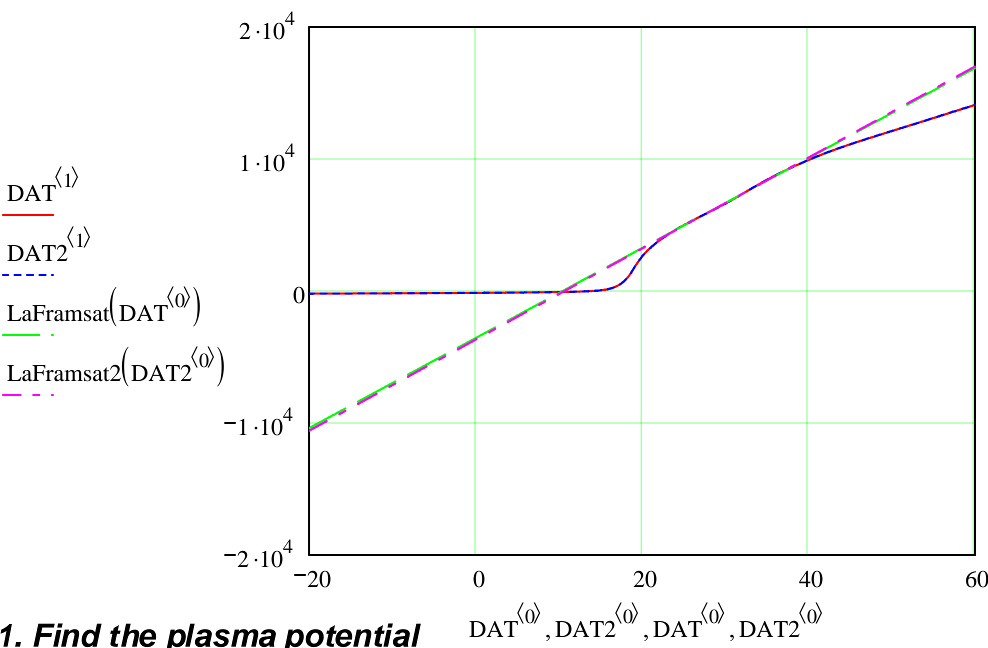

1. Find the plasma potential

The plasma potential is located at the maximum in the first derivative of the current. We find thi derivative from the difference between the next current data point and the previous one.

Because we need the difference between the data at k+1 and at k-1, our counter k must begin and end one point from the ends. (There is no k= -1 data point.)

$k := n_{Smthhigh} + 2 .. DatRows + n_{Smthlow} - 2$

$$\mathrm{Deriv}_{k,swp} := \frac{1}{12 \cdot dV} \cdot \left(\begin{array}{l} -\mathrm{DAT}_{k+2,\,2\cdot swp+1} + 8\cdot \mathrm{DAT}_{k+1,\,2\cdot swp+1} \cdots \\ + -8\cdot \mathrm{DAT}_{k-1,\,2\cdot swp+1} + \mathrm{DAT}_{k-2,\,2\cdot swp+1} \end{array} \right)$$

Find the maximum.

$$i_{Vp_{swp}} := \mathrm{match}\left(\max\left(\mathrm{Deriv}^{\langle swp \rangle}\right), \mathrm{Deriv}^{\langle swp \rangle}\right)_0$$

Use the **match** function to find the index.

There is some sneakiness involved here: the sub zero is required because match returns an array, and we want the values, not the "1x1 array"

$i_{Vp} = (388)$

The indices corresponding to the maximum derivative.

Probe voltage at the plasma potential, Vplasma. And the Saturation Current, Isat.

$$\mathrm{Vplasma}_{swp} := \left(\mathrm{DAT}^{\langle 2\cdot swp \rangle}\right)_{i_{Vp_{swp}}}$$

$\mathrm{Vplasma} = (18.8)$ Volts

$$\mathrm{Isat}_{swp} := \left(\mathrm{DAT}^{\langle 2\cdot swp+1 \rangle}\right)_{i_{Vp_{swp}}}$$

$\mathrm{Isat} = \left(1.495 \times 10^3\right)$ microamps

Define a region near the plasma potential for plotting.

$10^{-6} \cdot \mathrm{Isat} = \left(1.495 \times 10^{-3}\right)$

$\mathrm{kmin} := i_{Vp} - 10 \qquad \mathrm{kmax} := i_{Vp} + 10$

$\mathrm{IPlot}_{swp} := \mathrm{submatrix}\left(\mathrm{DAT}, \mathrm{kmin}_{swp}, \mathrm{kmax}_{swp}, 2\cdot swp, 2swp + 1\right)$

$\mathrm{dIPlot}_{swp} := \mathrm{submatrix}\left(\mathrm{Deriv}, \mathrm{kmin}_{swp}, \mathrm{kmax}_{swp}, swp, swp\right)$

The probe current near the plasma potential:

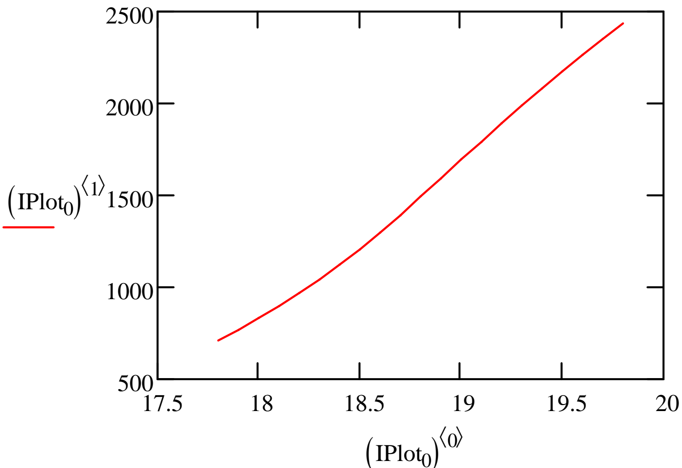

The derivative of the probe current with Vplasma indicated by lines:

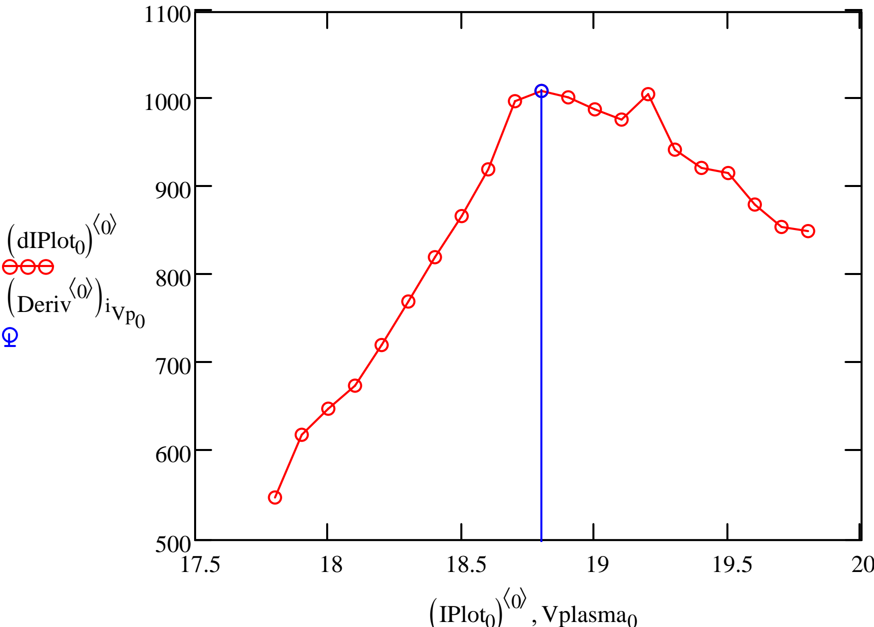

$$LFxitionParam := \left[\left(DAT^{\langle 1 \rangle}\right)_{iVp_0} - \left(Deriv^{\langle 0 \rangle}\right)_{iVp_0} \cdot \left(DAT^{\langle 0 \rangle}\right)_{iVp_0} \quad \left(Deriv^{\langle 0 \rangle}\right)_{iVp_0} \right]$$

$$LFxitionParam = \left(-1.75 \times 10^{4} \quad 1.01 \times 10^{3}\right)$$

$LaFramxition(x) := LFxitionParam_{0,0} + LFxitionParam_{0,1} \cdot x$

$$V_{ZXLF} := \frac{-LFxitionParam_{0,0}}{LFxitionParam_{0,1}}$$

$$Vp_{LF} := -\frac{LFxitionParam_{0,0} - LFsatParam_{0}}{LFxitionParam_{0,1} - LFsatParam_{1}} \qquad Vp_{LF} = 20.809$$

$$i_{VpLF_{swp}} := \left| \begin{array}{l} j \leftarrow DatRows - 1 \\ \text{while } DAT_{j,2swp} > Vp_{LF} \\ \quad j \leftarrow j - 1 \end{array} \right. \qquad i_{VpLF} = (408)$$

$Isat_{LF} := linterp\left(DAT^{\langle 0\rangle}, DAT^{\langle 1\rangle}, Vp_{LF}\right)$ $Isat_{LF} = 3.151 \times 10^{3}$ microamps

$extension := 2$

$i_m := V_{ZXLF} - extension, V_{ZXLF} + dV - extension .. Vp_{LF} + extension$

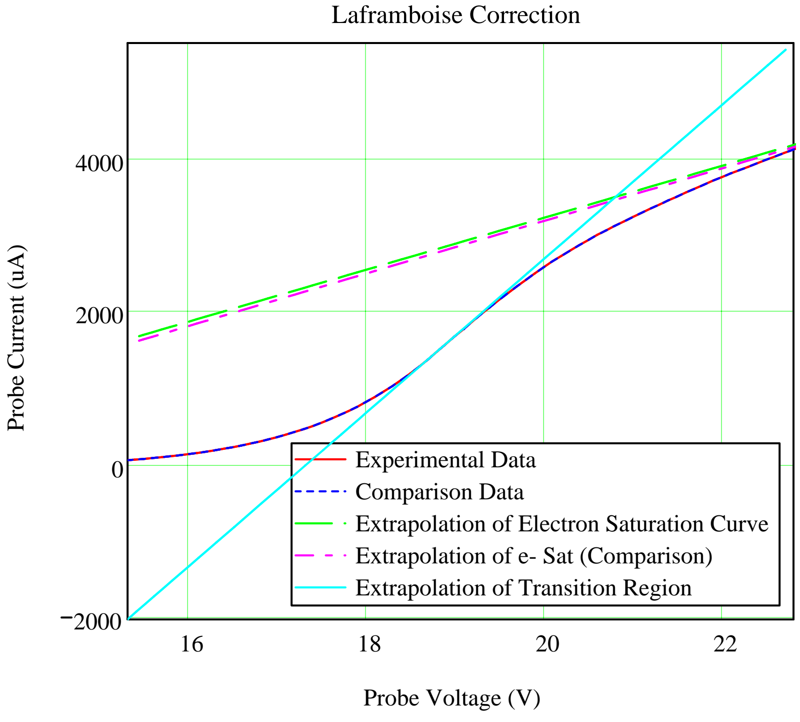

Option 1: Find the temperature from the slope of the logarithm of the current

Create a vector of subsets of 5 data points to the left of the plasma potential.

$$Sub_{swp} := \text{submatrix}\left(DAT, i_{Vp_{swp}} - 5, i_{Vp_{swp}} - 1, 0, 1\right)$$

Create a vector logI with the logarithms of the currents:

$$logI_{swp} := \overrightarrow{\ln\left[\left(Sub_{swp}\right)^{\langle 1\rangle}\right]}$$

The **vectorize** command (arrow on top) above the ln command creates a new matrix whose elements are the $\log_e$ of the elements of the original vector.

Now we can use the **line** function to return the slope and intercept.

$$AB_{swp} := \text{line}\left[\left(Sub_{swp}\right)^{\langle 0\rangle}, logI_{swp}\right]$$

$$Logfit(x,y) := \left(AB_y\right)_0 + \left(AB_y\right)_1 \cdot x$$

intercept
slope

We check the quaility of the fit by plotting the data and the fitted function:

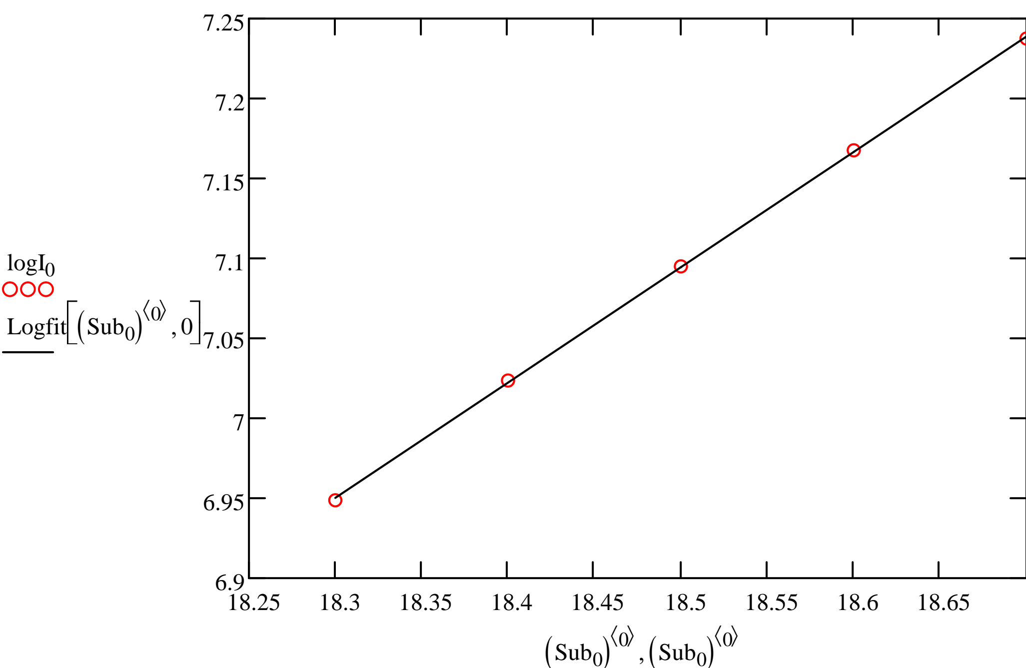

Now we can find Te from the inverse of th~ slope of the log graph:

$$Te_{swp} := \frac{1}{\left(AB_{swp}\right)_1} \qquad Te = (1.386)$$

Temperature in eV.

Option 1a: Find the temperature from the slope of the logarithm of the current with LaFramboise

Create a vector of subsets of 5 data points to the left of the plasma potential.

$$SubLF_{swp} := submatrix\left(DAT, i_{VpLF_{swp}} - 5, i_{VpLF_{swp}} - 1, 0, 1\right)$$

Create a vector logI with the logarithms of the currents:

$$logILF_{swp} := \overrightarrow{\ln\left[\left(SubLF_{swp}\right)^{\langle 1 \rangle}\right]}$$

The **vectorize** command (arrow on top) above the ln command creates a new matrix whose elements are the $\log_e$ of the elements of the original vector.

Now we can use the **line** function to return the slope and intercept.

$$ABLF_{swp} := line\left[\left(SubLF_{swp}\right)^{\langle 0 \rangle}, logILF_{swp}\right]$$

$$LogfitLF(x, y) := \left(ABLF_y\right)_0 + \left(ABLF_y\right)_1 \cdot x$$

intercept
slope

We check the quaility of the fit by plotting the data and the fitted function:

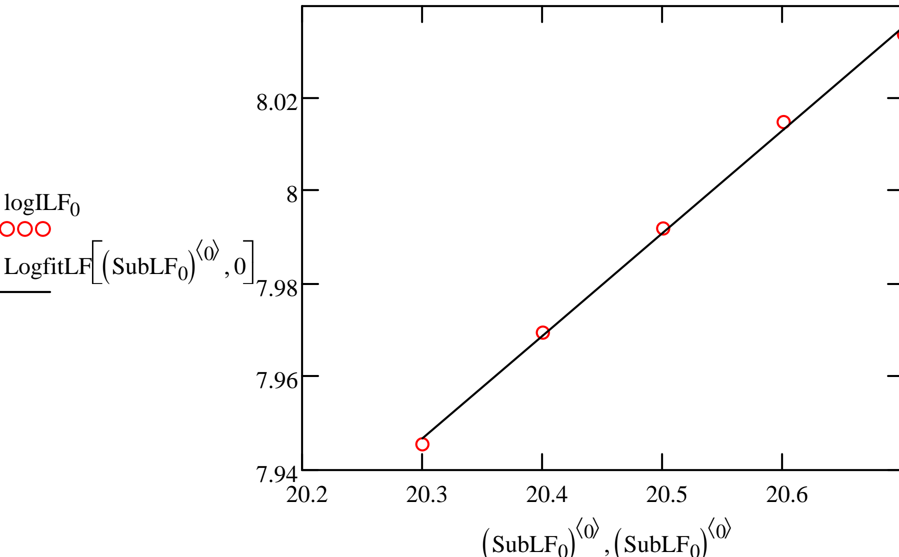

$$TeLF_{swp} := \frac{1}{\left(ABLF_{swp}\right)_1}$$

$TeLF = (4.505)$ Temperature in eV.

Find the density from Isat and the thermal velocity of electrons

Physical constants: $q := 1.6 \cdot 10^{-19}$ $\quad me := 9.11 \cdot 10^{-31}$

Now we can find Te from the inverse of the slope of the log graph:

Calculate the "flux" velocity of the electrons:

$$ve := \sqrt{\frac{q \cdot Te}{2\pi \cdot me}}$$

Note that qT_e is the electron energy because our temperature is in eV. We can use T_e and Isat and the equation at the beginning of the exercise to find the electron density n_e.

$$ne := \overrightarrow{\frac{Isat \cdot 10^{-6}}{ve \cdot Ap \cdot q}} \cdot m^{-3} \qquad ne = \left(1.209 \times 10^{10}\right) cm^{-3}$$

Electron density in cm^{-3}.

Now we have found the electron density and temperature from the probe data.
Note that Isat has been converted from microamps to amps.

Option 2: Smartprobe Method

$i_{Vf} = (342) \qquad i_{Vp} = (388)$

Integrate using the Trapezoidal Rule

$$Integral_{VfVp_{swp}} := \left[\sum_{m = i_{Vf_{swp}}}^{i_{Vp_{swp}}-1} \left[\frac{1}{2} \cdot \left[\left(DAT^{\langle 2 \cdot swp+1 \rangle}\right)_m + \left(DAT^{\langle 2 \cdot swp+1 \rangle}\right)_{m+1}\right]\left[\left(DAT^{\langle 2 \cdot swp \rangle}\right)_{m+1} + -\left(DAT^{\langle 2 \cdot swp \rangle}\right)_m\right]\right]\right]$$

$$Te_{SP} := \overrightarrow{\frac{Integral_{VfVp}}{Isat}} \qquad Te_{SP} = (1.2252) \quad \text{in eV}$$

Calculate the "flux" velocity of the electrons:

$$ve_{SP} := \sqrt{\frac{q \cdot Te_{SP}}{2\pi \cdot me}}$$

Note that qT_e is the electron energy because our temperature is in eV. We can use T_e and Isat and the equation at the beginning of the exercise to find the electron density n_e.

$$ne_{SP} := \overrightarrow{\frac{Isat \cdot 10^{-6}}{ve_{SP} \cdot Ap \cdot q}} \cdot m^{-3} \qquad ne_{SP} = \left(1.285 \times 10^{10}\right) cm^{-3}$$

Electron density in cm^{-3}.

Option 2a: Smartprobe Method w/ LaFramboise

$i_{Vf} = (342) \qquad i_{VpLF} = (408)$

Integrate using the Trapezoidal Rule

$$\text{Integral}_{VfVpLF_{swp}} := \left[\sum_{m = i_{Vf_{swp}}}^{i_{VpLF_{swp}}-1} \left[\frac{1}{2} \cdot \left[\left(DAT^{\langle 2\cdot swp+1 \rangle}\right)_m \cdots + \left(DAT^{\langle 2\cdot swp+1 \rangle}\right)_{m+1} \right] \left[\left(DAT^{\langle 2\cdot swp \rangle}\right)_{m+1} \cdots + -\left(DAT^{\langle 2\cdot swp \rangle}\right)_m \right] \right] \right]$$

$$Te_{SPLF} := \overrightarrow{\frac{\text{Integral}_{VfVpLF}}{\text{Isat}_{LF}}} \qquad Te_{SPLF} = (2.1017) \text{ in eV}$$

Calculate the "flux" velocity of the electrons: $ve_{SPLF} := \sqrt{\frac{q \cdot Te_{SPLF}}{2\pi \cdot me}}$

Note that qT_e is the electron energy because our temperature is in eV. We can use T_e and Isat and the equation at the beginning of the exercise to find the electron density n_e.

$$ne_{SPLF} := \overrightarrow{\frac{\text{Isat}_{LF} \cdot 10^{-6}}{ve_{SPLF} \cdot Ap \cdot q}} \cdot m^{-3} \qquad ne_{SPLF} = \left(2.069 \times 10^{10}\right) cm^{-3} \text{Electron density in cm}^{-3}.$$

Now we have found the electron density and temperature from the probe data.
Note that Isat has been converted from microamps to amps.

For the time being, let us create a nice little array that will fit directly into Excel: We currently want it in the format of:
kTe 1st swp SP, Ne 1st swp SP, kTe 2nd swp SP, Ne 2nd swp SP, kTe Avg swp SP, Ne Avg swp SP, kTe 1st swp LN, Ne 1st swp LN, kTe 2nd swp LN, Ne 2nd swp LN, kTe Avg swp LN, Ne Avg swp LN,

Clean up/Remove the units

$ne_{SP} := ne_{SP} \cdot cm^3$ $\quad ne_{SP} = \left(1.285 \times 10^{10}\right)$ $\quad ne := ne \cdot cm^3$ $\quad ne = \left(1.209 \times 10^{10}\right)$

$ne_{SPLF} := ne_{SPLF} \cdot cm^3$ $\quad ne_{SPLF} = \left(2.069 \times 10^{10}\right)$

$$Excel_line := augment\left(Te_{SP_0}, ne_{SP_0}, Te_{SPLF_0}, ne_{SPLF_0}, Te_0, ne_0\right)$$

$$Excel_line = \left(1.22521 \quad 1.28541 \times 10^{10} \quad 2.10166 \quad 2.06926 \times 10^{10} \quad 1.38574 \quad 1.20866 \times 10^{10}\right)$$

Appendix C. Langmuir Probe and Sweep Identification

C.1. Sweep Identification

A large number of data files were created when researching this topic. While initially each one was cataloged manually, the need for a systematic naming of the sweeps soon became apparent. Thus a folder structure and file naming convention was imposed. Figure C.36 shows the hierarchy of folders. The hierarchy levels with tokens in italics enclosed in brackets (<*token*>) and descriptions following a colon are listed below in descending order and will reference the example names in Figure C.36.

- <*Description of experiments*>: He Calibration Runs
- <*Year of runs*>: 2007
- Two options:
  - <*Two digit number run month*>–<*Name of run month*>: 11–November
  - <*Side experiment done under the same plasma conditions*>: Ceramic Test Length Runs
- (Optional) <*Two digit number run day*>: *Not present in this example.*
- <*Probe identification code*> L=<*probe tip length in cm*>, D=<*probe tip diameter in mm*>: 18-Pt-1-R0 L=0.5, D=0.25
  - The probe identification code will be discussed in the next section (

Langmuir Probe Identification).

- Run <*Run number*> Data: Run 120 Data
  - Optionally, a “Run <Run Number> Analysis” folder is included to store the MathCAD and Excel worksheets that analyze a particular run’s data.

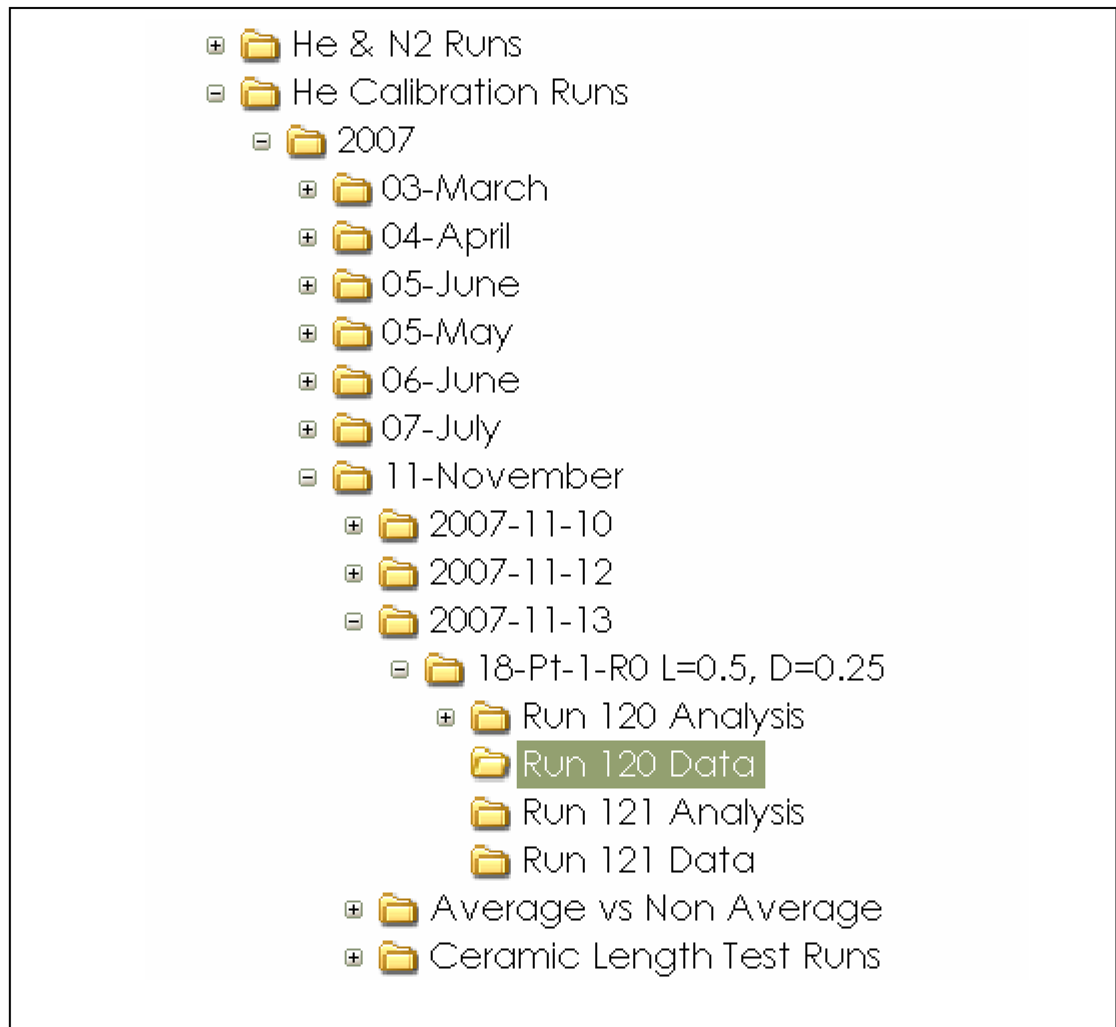

Figure C.36: Folder tree showing the hierarchy of folder names exemplifying the folder naming conventions.

Similarly, Figure C.37 shows an example of the run naming conventions. While the names of the files can be somewhat altered based on what the user selects in the data file organization form in the data acquisition application and sweep control form, the names follow a file format as described below, using Run 120F1 from Figure C.37 as an example. Tokens are in italics enclosed in brackets followed by either a definition or the data from the example.

- <*Run Identifier*> – <*Plasma Chemistry*> – <*Plasma Conditions*> <*Plasma DC Bias*> <*Sweep Voltage Description*>.csv:
  Run 120F1 – 100% He – 125 mTorr 50 W -168 V from -20.00 to 60.00 by 0.10 V.csv
  - <*Run Identifier*>: Run <*Run Serial Number*> <*Cleaning Serial Letter*><*Intra-cleaning Serial Number*>
    - <*Run Serial Number*>: 120
    - <*Cleaning Serial Letter*>: F
    - <*Intra-cleaning Serial Number*>: 1
  - <*Plasma Chemistry*>: 100% He
  - <*Plasma Conditions*>: 125 mTorr 50 W
  - <*Plasma DC Bias*>: -168 V
  - <*Sweep Voltage Description*>: from -20.00 to 60.00 by 0.10 V

Figure C.37: Several run files exemplifying the run naming conventions.

C.2. Langmuir Probe Identification

Because a large number of Langmuir probes were produced with differing characteristics, a way to index them became paramount to ensuring consistency and repeatability. This section will present the method behind the serial coding of the probes, but more importantly will help one to understand what probe produced what data when sifting through the supplemental data. The probe identifiers follow the format described below with tokens in italics enclosed in brackets, the example probe name will be the one referenced in Figure C.36

- <*Probe series number*>–<*Probe tip material*>–<*Probe serial number within the probe series*>–<*Rework number*>: 18–Pt–1–R0
    - <*Probe series number*>: 18
    - <*Probe tip material*>: Pt (Platinum)
    - <*Probe serial number within the probe series*>: 1
    - <*Rework number*>: R0
        - The rework number represents the number of times the probe housing has been opened and re-sealed to modify the probe tip or any other component of the probe. Typically probes last through three to four reworks.